

Analysis Of Gearbox Loads In Large Air Cooled Condensers

by

Charles Henry Ochse Lombard



*Thesis in partial fulfilment of the requirements for the degree
of Master of Engineering (Mechanical) in the Faculty of
Engineering at Stellenbosch University*

Supervisor: Dr. Daniel Nicolaas Johannes Els

Co-supervisor: Dr. Jacques Muiyser

March 2017

Declaration

By submitting this thesis electronically, I declare that the entirety of the work contained therein is my own, original work, that I am the sole author thereof (save to the extent explicitly otherwise stated), that reproduction and publication thereof by Stellenbosch University will not infringe any third party rights and that I have not previously in its entirety or in part submitted it for obtaining any qualification.

Date: March 2017

Copyright © 2017 Stellenbosch University
All rights reserved.

Abstract

Analysis Of Gearbox Loads In Large Air Cooled Condensers

C.H.O. Lombard

*Department of Mechanical and Mechatronic Engineering,
University of Stellenbosch,
Private Bag X1, Matieland 7602, South Africa.*

Thesis: Mechanical Engineering

March 2017

Operational gearbox loading, in an air-cooled condenser (ACC), is measured and analysed in this investigation. Measurements are recorded during the start, stop and normal operational periods of the gearbox. Interaction between gearbox input and output torsion and bending experienced by the output shaft, are the primary focus of the study. Secondary areas of investigation include gearbox vibration, temperature, shaft speeds and power consumption of the motor. Correlations are also drawn between gearbox loading and wind conditions.

Industry has noted that the gearboxes used in the ACC of large coal fired power stations, are responsible for most of the unit down-time, which motivated the above mentioned investigation. This investigation is part of a collaboration between Stellenbosch University and various industry partners. The knowledge gained from this study may be used to optimize selection criteria, design of ACC gearbox components, and to improve operation and maintenance information. Previous research has not yet published data that was obtained from the input shaft of such a gearbox, as working conditions complicate this task.

A previously developed measurement system is customized to meet the requirements of this investigation. Strain gauges are used to measure torsion on both gearbox shafts as well as bending on the output shaft. The data is transmitted from the rotating shafts by means of radio frequency and it is recorded by using a very specialized data acquisition system. Gearbox shaft speed, vibration and temperature are measured with proximity sensors, accelerometers and a thermal camera. The power supply of the motor is measured with an

oscilloscope and current transformers. The data from the various sensors are time synchronized before recording.

The accelerometers and the thermal camera were calibrated beforehand, while the same was not possible for the strain gauges. Fundamental strain theory was used to determine the measured torsion and bending on the output shaft. The accuracy of the input shaft measurements are quantified by means of finite element analysis, statistical analysis and laboratory testing. Vibration analysis is then also performed on the input shaft to investigate the relationship between temperature and elastic modulus.

Firstly, start-up measurements showed that the induction motor draws up to 7.89 times the rated power. During this period, gearbox torque was measured to be roughly four times higher than the operational torque. Secondly, analysis of the normal operational data showed that strain measurement is affected by shaft temperature, while frequency spectrum analysis proved that torsional vibrations are transferred through the gearbox. Correlations were also drawn between output shaft bending and varying wind conditions. Lastly, stop period measurements were able to show reverse loading of the gearbox, as the fan drives the motor during that period.

This study succeeded in acquiring and analysing data from the input shaft of an operational ACC gearbox, which has never been done before. It was also established that absolute strain gauge measurements are not possible without knowing the exact material properties of the test sample.

Uittreksel

Analise Van Ratkas Laste In Groot Lug Verkoelde Kondenseerders

(“Analysis Of Gearbox Loads In Large Air Cooled Condensers”)

C.H.O. Lombard

*Departement Meganiese en Megatroniese Ingenieurswese,
Universiteit van Stellenbosch,
Privaatsak X1, Matieland 7602, Suid Afrika.*

Tesis: Mechanical Engineering

Maart 2017

In hierdie ondersoek word die operasionele lading van 'n ratkas van 'n lugverkoelde kondenseerder (LVK) gemeet en ontleed. Metings word geneem tydens die begin, stop en normale operasionele werkstoestande van die ratkas. Die primêre fokus van hierdie studie is die interaksie tussen die in- en uitree torsie van die ratkas, en die buigmoment van die uitree-as. Sekondêre areas van die ondersoek sluit in ratkas vibrasie, temperatuur, as-spoed en kragverbruik van die motor. Ooreenkomste word ook gemaak tussen die las van die ratkas en windtoestande.

Die industrie het opgemerk dat die LVK ratkaste by groot steenkool aangedrewe kragstasies die hooforsaak van LVK stilstandtyd is. Dit het hierdie ondersoek gemotiveer en vorm deel van die samewerking tussen die Universiteit van Stellenbosch en vennote in die industrie. Die kennis wat in hierdie studie opgedoen word, kan gebruik word vir die optimering van seleksie standaarde, die ontwerp van LVK ratkas komponente en die verbetering van operasionele en onderhouds inligting. As gevolg van komplekse werksomstandighede, is vorige navorsings data wat verkry is van die intree-as van hierdie ratkaste, nog nie gepubliseer nie.

'n Reeds bestaande meetstelsel is aangepas om aan die vereistes van hierdie ondersoek te voldoen. Rekestrokies word gebruik om die torsie in beide ratkas asse te meet. Die buiging van die uitree-as word ook deur rekestrokies gemeet. Data word van die roterende asse versend deur middel van radio frekwensie en dit word opgeneem deur 'n gespesialiseerde data opnemingsstelsel. Die ratkas se as-spoed, vibrasie en temperatuur word gemeet met nabyheids

sensors, versnellingsmeters en 'n termiese kamera. Die krag toevoer na die motor word gemeet met 'n ossiloskoop en stroom transformators. Die data van die onderskeie sensors word gesinkroniseer voor dit opgeneem word.

Die versnellingsmeters en termiese kamera is vooraf gekalibreer, maar dit was nie moontlik vir die rekstrokie nie. Fundamentele vervormingsteorie is gebruik om die torsie en uitree-as buiging vas te stel. Die akkuraatheid van die intree-as se metings word gekwantifiseer deur middel van eindige element analise, statistiese analise en laboratorium toetsing. Vibrasie analise word ook uitgevoer op die intree-as om die verwantskap tussen temperatuur en elastisiteits modulus te ondersoek.

Hierdie ondersoek se metings toon eerstens dat die induksie motor tydens die begin tydperk 7.89 keer die gespesifiseerde drywing trek. Gedurende hierdie tydperk was die ratkas torsie ongeveer vier keer hoër as die operasionele torsie. Tweedens toon die analise van die normale operasionele data dat die vervormingsmeting beïnvloed word deur die as se temperatuur, terwyl frekwensie spektrum analise bewys dat torsie vibrasies deur die ratkas oorgedra word. Ooreenkomste word ook gemaak tussen die buiging van die uitree-as en veranderlike windtoestande. Laastens het die metings van die stopperiode getoon dat omgekeerde belading van die ratkas plaasvind, aangesien die motor in hierdie periode deur die waaier aandryf is.

Die ondersoek het daarin geslaag om data van die intree-as van 'n operasionele LVK ratkas te bekom en te ontleed, iets wat nog nie voorheen gedoen is nie. Daar is ook vasgestel dat absolute rekstrokie metings nie moontlik is sonder dat die akkurate materiaal-eienskappe van die toetsmonster bekend is nie.

This thesis is dedicated to my parents and my wife, for their unconditional love and support.

Acknowledgements

I would like to thank the following parties for their continual support throughout the project:

- Dr. Danie Els and Mr. Jacques Muiyser, my supervisors, for their faith in my abilities as well as their guidance and assistance throughout the course of the investigation.
- Hansen Industrial Transmissions and GEA Aircooled Systems for their financial and technical support. In particular I would like to thank Mr. Stephan Britz for his technical support and his role as my industry mentor.
- Eskom for the opportunity to record measurements at one of their power station facilities. I would like to thank Mr. Francois Nel for his assistance prior and during the site excursion.
- University of Stellenbosch and the Mechanical en Mechatronic Engineering workshop for the use of their hardware and facilities. I specifically want to thank Mr. Ferdi Zietsman for his assistance in the preparation of my strain gauges, and accompanying me on site excursions.

Contents

Declaration	i
Abstract	ii
Uittreksel	iv
Acknowledgements	vii
Contents	viii
List of Figures	xi
List of Tables	xvi
Nomenclature	xvii
1 Introduction	1
1.1 Objectives	1
1.2 Scope	1
1.3 Deliverables	2
2 Literature Study	3
2.1 Power Station Background	3
2.1.1 Coal Fired Power Generation	3
2.1.2 Air Cooled Condenser	4
2.1.3 Electric Motor	5
2.1.4 M4ACC Gearbox	6
2.1.5 Fan and Air Circulation	7
2.2 Gearbox Failures	8
2.2.1 Torsional and Lateral Vibration	10
2.2.2 Bearings	10
2.2.3 Lubrication	11
2.2.4 Unexpected Loads	11
2.2.5 Thermal Instability	12
2.3 Measurement System	12

2.3.1	Strain Gauge	12
2.3.2	Vibration and Accelerometers	14
2.3.3	Signal Transmission and Recording Hardware	15
2.3.4	Integration of Measurement System	16
2.3.5	Reliability of Strain Measurements	17
2.4	Application of Literature Review	17
3	Quantification of Measurement Accuracy	18
3.1	Background	18
3.2	Strain Gauge Measurements	21
3.2.1	Experimental Procedure	23
3.2.2	Torsional Strain Theory	24
3.2.3	Experimental Results	26
3.3	Digital Image Correlation	28
3.3.1	Experimental Procedure	29
3.3.2	Experimental Results	30
3.4	Finite Element Modelling	31
3.4.1	Mesh Independence Study	32
3.4.2	Torque Transfer by Coupling	32
3.4.3	Torque Transfer by Key	35
3.4.4	Modelled Stress Distribution	36
3.4.5	Modelled Strain Measurement	36
3.5	Statistical Analysis	40
3.5.1	Define Problem and Random Variables	40
3.5.2	Effect of Strain Gauge Misalignment	41
3.5.3	Effect of Material Properties	43
3.6	Relationship Between Shaft Elasticity and Temperature	45
3.6.1	Background	45
3.6.2	Theoretical Calculations	46
3.6.3	Experimental Procedure	47
3.6.4	Experimental Results	48
3.6.5	FE Modal Analysis	51
3.7	Strain Measurement Accuracy	53
4	Measurements	54
4.1	Induction Motor Measurements	54
4.2	Strain Gauge Measurements	55
4.3	Speed, Temperature and Vibration Measurements	57
4.4	Experimental Information	58
4.4.1	Hardware	58
4.4.2	Operational States Measured	58
4.5	Results: Torque Transmission	59
4.5.1	Start-up Measurements	59
4.5.2	Normal Operation Measurements	63

<i>CONTENTS</i>	x
4.5.3 Run-down Measurements	68
4.6 Results: Output Shaft Bending	70
4.7 Results: Gearbox Vibration	76
5 Conclusion	79
5.1 Areas of Investigation	79
5.2 Investigation Findings	80
5.3 Recommendations for Future Measurements	81
Appendices	82
A Gear Design	83
B Relation Between Strain and Electric Resistance	87
C Instrument Calibration	89
C.1 Accelerometer	89
C.2 Load Cell	90
D Finite Element Analysis	92
D.1 Stress and Varying Material Properties	92
D.2 Linearity of Stress and Torque	93
E Oscilloscope Measurements	94
F Weather Station Data	96
G Project Photographs	99
G.1 Gearbox Input Shaft	99
G.2 Strain Gauge Rosettes	100
G.3 Proximity Sensor Connection	101
G.4 Shaft Protection	102
G.5 Gearbox Installation	104
H Measurement Data	106
H.1 Start-up Power Transfer	106
H.2 Raw Output Shaft Bending	107
H.3 Filtered Output Shaft Bending	110
Bibliography	113

List of Figures

2.1	Matimba coal-fired power station (Pretorius, 2012).	3
2.2	Illustration of ACC unit arrangement (Phala <i>et al.</i> , 2007).	4
2.3	ACC with inclined A-type frame design (Muiyser, 2012).	5
2.4	Induction motor assembly, Lin (2014).	6
2.5	Two-stage Hansen M4ACC gearbox and gears (Hansen Industrial Transmissions, 2004)(Goldschagg, 2013).	7
2.6	Ideal circulation and hot air recirculation in an ACC (Liu <i>et al.</i> , 2009).	7
2.7	Illustration of a single fan (Goldschagg, 2013).	8
2.8	Two-stage industrial gearbox.	8
2.9	Gear failures at Matimba power station from 1994 to 2012 (Goldschagg, 2013).	9
2.10	Perpendicular shaft multi-stage industrial gearbox after axial failure	9
2.11	Particle indentation onto roller.	11
2.12	Advanced roller bearing failure.	11
2.13	Illustration of the Wheatstone bridge and a strain gauge (McGinty, 2012).	13
2.14	Simplified depiction of a piezoelectric transducer used in an accelerometer.	14
2.15	SG-Link-LXRS used to transmit the signal from the gearbox input shaft.	15
2.16	V-Link-LXRS used to transmit multiple signals from the gearbox output shaft.	15
2.17	Illustration of the WSDA-Base-104 station used to receive the signals from the SG-Link-LXRS and V-Link-LXRS.	16
2.18	QuantumX MX1601B data acquisition (DAQ) apparatus, used to synchronise analogue signals from multiple sensors.	16
2.19	Integrated measurement system.	16
3.1	Input and output shaft of the M4ACC gearbox, and an illustration of the input shaft with regard to wind and lubricant.	19
3.2	Strain measurement system.	19

3.3	Input shaft of the M4ACC gearbox with strain gauge rosettes positioned in the ideal position, and illustration of left-hand-side (LHS) and right-hand-side (RHS) convention.	20
3.4	Illustration of sleeve used to prevent coupling from sliding on the input shaft.	20
3.5	Wheatstone bridge circuit with four active strain gauges.	21
3.6	Torsional strain gauge rosette mounted on the RHS of the keyway.	22
3.7	Full bridge strain gauge configuration used for torsional strain measurement.	22
3.8	Input shaft mounted onto the work bench for laboratory calibration.	23
3.9	Moment arm under full load connected to the input shaft and the work bench.	23
3.10	Plane stress element (A) and equivalent principal stress element (B) on the outer surface of a shaft subjected to torsion.	25
3.11	Mohr's circle for plane strain.	25
3.12	Comparison between strain measured on both the LHS and RHS of the keyway for the same shaft torsion.	27
3.13	Comparison between applied torque and measured torque.	28
3.14	Speckled pattern used to track deformation on the RHS of the keyway. The position that is chosen as the zero-reference point is also shown (Zero Point)	29
3.15	Two-camera stereo vision DIC camera setup.	29
3.16	Tangential displacement of nodes on the LHS (-20 mm to 0 mm) and RHS (0 mm to 20 mm) of the keyway.	30
3.17	Strain measured 25 mm to the left of the keyway.	31
3.18	Strain measured 25 mm to the right of the keyway.	31
3.19	Mesh independence.	32
3.20	Geometric constraint applied to the input shaft, modelling the interference fit of the coupling.	33
3.21	Diagram of symbols used for interference fit assembly.	33
3.22	Force exerted by key onto keyway wall.	35
3.23	Torsion applied between the keyway and the gear teeth, modelling zero interference from the coupling and torque transfer by means of the key.	35
3.24	Fringe plot of maximum shear stress experienced by the modelled shaft.	36
3.25	Nodes on FEM models that represent the possible strain gauge position.	37
3.26	Illustration of stress transformation on to the plane of strain measurement.	37
3.27	Strain gauge rosette (SGR) misalignment in the axial direction ($\pm z_{err}$) and in the tangential ($\pm \theta_{err}$) direction on the circumferential line (CL).	41

3.28	Angular strain gauge misalignment measured from the circumferential line (CL).	42
3.29	Statistical distribution of the modelled strain for each strain gauge of the full bridge configuration.	43
3.30	Distribution of the modelled full bridge strain measurement over 100 000 iterations.	45
3.31	Setup used for AE measurements.	47
3.32	Spectrogram of shaft frequencies.	48
3.33	Frequency spectrum plot of shaft vibration.	49
3.34	First natural frequency of input shaft.	49
3.35	Frequency change of the first (f_{1_j}), second (f_{2_j}) and third (f_{3_j}) natural frequencies of the shaft at temperature j	50
3.36	Percentage change in E vs. temperature of shaft.	51
3.37	Mode shapes of the input shaft.	52
3.38	Statistical relationship between shaft torque and torsional strain.	53
3.39	Correction factor for increased operational shaft temperature.	53
4.1	Position of test gearbox with regard to the power station.	54
4.2	Current transformer connection.	55
4.3	Full bridge strain gauge configuration used for bending strain measurement.	56
4.4	Perpendicular bending planes on the output shaft of the M4ACC gearbox.	57
4.5	Sensors used on the M4ACC gearbox.	58
4.6	Start-up torque measured on 19 April 2016, at 13:30.	59
4.7	Start-up torque measured on 20 April 2016, at 15:30.	60
4.8	Start-up torque measured on 21 April 2016, at 11:40.	60
4.9	Input shaft speed during start-up.	61
4.10	Output shaft speed during start-up.	61
4.11	Comparison of power transfer from the motor to the gearbox output, measured on 21 April 016.	61
4.12	Start-up power transmission of the gearbox.	62
4.13	Temperature change of gearbox casing.	63
4.14	Electric power measured at the switch board, roughly 100 m from the motor.	63
4.15	Frequency spectrum plot of instantaneous power.	64
4.16	Gearbox input shaft power with measurement tolerance band and motor output power, measured on 26 April 2016.	65
4.17	Torque transmission from the input shaft to the output shaft directly after start-up.	66
4.18	Torque transmission from the input to output shaft one hour after start-up.	66
4.19	Torque transmission from the input to output shaft two hours after start-up.	67

4.20	Frequency spectrum plot of the input shaft torque.	67
4.21	Frequency spectrum plot of the output shaft torque.	68
4.22	Speed of the output shaft during the run-down period.	68
4.23	Torque measured on both gearbox shafts during the run-down period.	69
4.24	Spectrogram of output shaft torque during the run-down period.	70
4.25	Rotational frequency of the input and output shafts of the gearbox, and the natural frequency of the fan blades versus output shaft speed.	70
4.26	Orientation of polar plot with regard to the fan-bridge.	71
4.27	Bending experienced by the output shaft during three wind direc- tions and constant wind speed.	71
4.28	Frequency spectrum plot of output shaft bending.	72
4.29	Bending forces present on the output shaft at rotational frequency.	73
4.30	Polar plot of bending components present in the bending data for a wind speed and direction of 25.6 m/s and 92°E.	74
4.31	Polar plot of bending experienced by the shaft on 25 April 2016, at 13:00.	75
4.32	Polar plot of bending experienced by the shaft on 25 April 2016, at 11:00.	75
4.33	Polar plot of bending experienced by the shaft on 25 April 2016, at 16:00.	76
4.34	Frequency spectrum of gearbox vibration in the z -direction, from 0 Hz to 200 Hz.	77
4.35	Frequency spectrum of gearbox vibration in the x -direction, from 0 Hz to 200 Hz.	77
4.36	Frequency spectrum of gearbox vibration in the z -direction, from 0 Hz to 40 Hz.	78
4.37	Frequency spectrum of gearbox vibration in the x -direction, from 0 Hz to 40 Hz.	78
B.1	Resistive wire placed on a plastic grid.	87
C.1	SV111 Vibration Calibrator.	89
C.2	HEAD acoustics SQuadriga II.	89
C.3	PCB-Accel-333B32 positioned on the vibration plate.	90
C.4	Settings panel of the SV111 Vibration Calibrator.	90
C.5	HBM RSCC-Load-Cell.	91
C.6	Calibration setup.	91
C.7	Load cell calibration curve.	91
D.1	Load control with varying elastic modulus.	92
D.2	Load control with varying Poisson's ratio.	93
D.3	Relationship between shaft torque and shear stress.	93
E.1	Line to neutral voltage and current.	94
E.2	Time lag between line voltage and current.	95

G.1	Input shaft.	99
G.2	Input shaft front view.	99
G.3	Sleeve with machined opening.	100
G.4	Sleeve with grub screw to keep sleeve in place.	100
G.5	Bending strain gauge rosette on the output shaft.	100
G.6	Torsional strain gauge rosette on the output shaft.	100
G.7	Torsional strain gauge rosette on the input shaft.	100
G.8	Proximity sensor rod for input shaft speed measurement.	101
G.9	Magnet and proximity sensor used for input shaft.	101
G.10	Proximity sensor positioned for output shaft speed measurement.	101
G.11	Proximity sensor and magnet used to measure the output shaft speed.	102
G.12	SG-Link-LXRS installed onto high speed coupling with free hanging connecting wires.	102
G.13	SG-Link-LXRS installed onto high speed coupling with connecting wires fixed to the coupling with quick set cement.	103
G.14	Strain gauges positioned on the output shaft.	103
G.15	Output shaft protection before transport.	103
G.16	Connecting the lift to the gearbox on the ground.	104
G.17	Gearbox being lowered into position in the ACC.	104
G.18	Connecting the gearbox output shaft to the fan hub.	105
G.19	Installation complete.	105
H.1	Start-up power transmission of the gearbox on 19 April 2016.	106
H.2	Start-up power transmission of the gearbox on 20 April 2016.	107
H.3	Start-up power transmission of the gearbox on 21 April 2016.	107
H.4	Bending moment measured on the output shaft by both bending full bridge configurations.	108
H.5	Absolute bending moment experienced by the output shaft.	109
H.6	Angle of absolute bending moment, with regard to the global coordinate system.	109
H.7	Absolute bending moment experienced by the output shaft shown for a two second period.	110
H.8	Angle of absolute bending moment, with regard to the global coordinate system, shown for a two second period.	110
H.9	Polar plot of bending components present in the bending data for a wind speed and direction of 25.4 m/s and 116°ESE.	111
H.10	Polar plot of bending components present in the bending data for a wind speed and direction of 24.6 m/s and 66°ENE.	112

List of Tables

3.1	LHS half bridge, RHS half bridge, difference between LHS and RHS measurements, and full bridge strain.	39
3.2	Mean variation of the modelled stress compared to the ideal stress.	42
3.3	Statistical characteristics of the modelled strain distribution.	44
3.4	Comparison between strain experienced by a full bridge configuration positioned on an ideal shaft and the modelled shaft, as well as the standard deviation of the modelled shaft strain.	44
3.5	Average change in elastic modulus of the shaft for each temperature interval.	51
3.6	Comparison between FE simulation and AE measurements on the input shaft.	52
4.1	Peak start-up torque.	60
4.2	Wind speed and direction.	72
F.1	Weather station measurements.	98

Nomenclature

Constants

$$g = 9.81 \text{ m/s}^2$$

Acronyms

ACC	Air-cooled condenser
AC	Alternating current
AE	Acoustic emission
CT	Current transformer
CL	Circumferential line
DC	Direct current
DIC	Digital image correlation
E	East
ESE	East-South-East
FE	Finite element
FEM	Finite element method
FFT	Fast Fourier transform
LHS	Left-hand-side
N	North
NE	North-East
NNE	North-North-East
NNW	North-North-West
NNW	North-North-West
PDF	Probability density function
PF	Power factor
PMF	Probability mass function
RHS	Right-hand-side
S	South
SG	Strain gauge
SGR	Strain gauge rosette

W West

Variables

A	Area	[m ²]
D	Diameter	[m]
E	Elastic modulus	[GPa]
E'	Elastic modulus at elevated temperature	[GPa]
ΔE	Change in elastic modulus at varying temperatures	[GPa]
F	Bending force	[N]
f	Frequency	[Hz]
f'	Natural frequency at elevated temperature	[Hz]
G	Shear modulus	[GPa]
I	Moment of inertia	[A]
J	Polar moment of inertia	[m ⁴]
k	Gauge factor	[]
L	Length	[m]
l_1	Radial displacement of the center of mass	[m]
l_2	Length of output shaft	[m]
M	Bending moment	[N · m]
m	Mass	[kg]
N	Number of	[]
P	Power	[W]
R	Resistance	[Ω]
r	Shaft radius	[m]
S	Strain measured on the input shaft	[$\mu\text{m}/\text{m}$]
T	Torque	[N · m]
V	Voltage	[V]
β	Beam boundary condition constant	[]
ϵ	Strain	[$\mu\text{m}/\text{m}$]
η	Motor efficiency	[]
θ	Angle	[$^\circ$]
ν	Poisson's ratio	[]
ρ	Density	[kg/m ³]
σ	Stress	[Pa]
ω	Rotational speed	[rad/s]

Subscripts

1 – 2	Principal stress/strains
1 – 4	Positions of the Wheatstone bridge resistors
<i>ap</i>	Assembly phase
<i>B1</i>	First bending plane
<i>B2</i>	Second bending plane
<i>bl</i>	Blade lift
<i>bp</i>	Blade pass
<i>cen</i>	Centrifugal
<i>fb</i>	Fan bridge
<i>g</i>	Gear
<i>gm</i>	Gear mesh
<i>gr</i>	Gravitational
<i>gt</i>	Gear teeth
<i>gtm</i>	Gear teeth mesh
<i>i_j</i>	<i>i</i> -th instance at <i>j</i> -interval
<i>i₀</i>	<i>i</i> -th instance at a fixed interval
<i>img</i>	Intermediate gear
<i>is</i>	Inner shaft
<i>ms</i>	Mating surface
<i>oc</i>	Outer coupling
<i>p</i>	Pinion
<i>pt</i>	Pinion teeth
<i>rg</i>	Rotation of gear
<i>ris</i>	Radial stress at the outer radius of the shaft
<i>roc</i>	Radial stress at the outer radius of the coupling
<i>rp</i>	Rotation of pinion
<i>sg</i>	Strain gauge
<i>tr</i>	Tooth repeat
<i>x</i>	<i>x</i> -direction
<i>x1</i>	Rotated <i>x</i> -axis-direction
<i>xy</i>	Perpendicular to the <i>x</i> -plane and directed in the <i>y</i> -direction
<i>x1y1</i>	Perpendicular to the <i>x1</i> -plane and directed in the <i>y1</i> -direction
<i>y</i>	<i>y</i> -direction
<i>y1</i>	Rotated <i>y</i> -axis-direction
<i>yx</i>	Perpendicular to the <i>y</i> -plane and directed in the <i>x</i> -direction

*NOMENCLATURE***xx**

- y_1x_1 Perpendicular to the y_1 -plane and directed in the x_1 -direction
 θ_i Circumference of inner shaft
 θ_o Circumference of outer coupling

Chapter 1

Introduction

Stellenbosch University set out an investigation to analyse operational gearbox loading in an air-cooled condenser (ACC) of a coal fired power station. Knowledge gained from this investigation can be used to optimize selection criteria, design of components and improve operational and maintenance information.

1.1 Objectives

The primary objectives of this investigation can be listed as:

- The development of a measurement system that meets the requirements of this project.
- Recording reliable data of gearbox loading in an operational ACC of a coal fired power station.
- Accurate analysis of the acquired data.

1.2 Scope

The research will focus mainly on the analysis of the gearbox system currently installed in the ACC of Matimba power station. Primarily, gearbox loads are measured on the input and the output shafts during three modes of operation i.e. start-up, run-down and normal operational periods. Secondary measurements include gearbox vibration, temperature and shaft speeds.

Power transferred from the motor to the gearbox will be investigated. The input and output torsion on the gearbox shafts during the start-up period will be recorded. This investigation will also quantify the magnitude and duration of the load exerted by the fan onto the gearbox during the run-down period. Load fluctuation during normal operation of the gearbox is investigated to observe whether wind conditions could cause unexpected loading. The analysis

performed during normal operation includes torque transmission through the gearbox, bending loads on the output shaft and gearbox vibration.

The scope of this research does not include a detailed evaluation of the entire ACC system with accompanying design recommendations. The focus is specifically aimed at the interaction between the electric motor, the gearbox and the fan, while monitoring the gearbox shafts.

1.3 Deliverables

The following deliverables can be expected at the completion of the proposed investigation: (1) a relevant literature review; (2) the development of the necessary measurement equipment; (3) reliable on-site measurements of gearbox loads and behaviour; (4) accurate data analysis of the measured data; (5) concluding remarks on gearbox load conditions and environmental effects.

A brief background is given on coal-fired power stations, ACCs, electric motors, industrial gearboxes and the ACC's air circulation. Gearbox failure is further investigated to better understand the motivation behind the proposed research. Focus is then put on each component of the measurement system, the integration thereof, and the synchronization and acquisitions of the data.

Previous research has failed to document torque measurements from the input shaft of an operational ACC gearbox. A measurement system has been developed that allows the transmission of torsional data from the rotating input shaft of the gearbox, overcoming the sensor installation challenges regarding rotational speed, shaft geometry and space limitations. The system also allows time synchronization of all the sensors therein.

Using the above mentioned measurement system, gearbox loads are measured in the operational ACC of Matimba power station. Torque is measured on both gearbox shafts during the start-up, run-down and normal operational period. Bending is measured on the output shaft of the gearbox, while gearbox vibration, temperature and shaft speeds are also measured. Weather data is obtained from a nearby weather station for the relevant measurement days.

Factors such as unknown material properties and shaft geometry, compromise the accuracy of the measurements obtained from the input shaft. Laboratory experimentation, finite element and statistical analysis is performed to quantify the accuracy of the input shaft measurements. Measurements obtained from the output shaft, proximity sensors and accelerometers do not have the same problem and are accurately analysed with greater ease.

Gearbox loading during start-up, run-down and normal operation periods are quantified. System vibrations are identified, and relationships are drawn between gearbox loading and varying wind conditions.

Chapter 2

Literature Study

The primary research goal is to accurately measure and analyse the loads that the M4ACC gearbox is subjected to. This chapter aims to provide background on the field of study, while placing focus on the measurement system.

2.1 Power Station Background

The workings of a coal-fired power station and the components of the power station's ACC are discussed in this section.

2.1.1 Coal Fired Power Generation

A coal fired power station, illustrated in Figure 2.1, makes use of the Rankine cycle where cold fluid is heated by an external source of energy (coal fire in this case) to form hot vapour that generates electricity through a steam turbine (Kröger, 2004). To obtain optimum power generation efficiency from the power station it is essential to maximize the temperature difference between the fluid entering, and the vapour leaving the boiler (Nguyen *et al.*, 2001).



Figure 2.1: Matimba coal-fired power station (Pretorius, 2012).

2.1.2 Air Cooled Condenser

A forced draft ACC is used as a dry-cooling mechanism in locations where water sources are scarce. The primary function of the ACC at coal fired power stations is to condense steam turbine vapour, and to return it to the feed water cycle at a temperature as cold as possible (Fay, 1997). Improving the efficiency of the ACC increases the efficiency of the power station (Beër, 2007). Figure 2.2 illustrates how four ACC fans are positioned in a row.

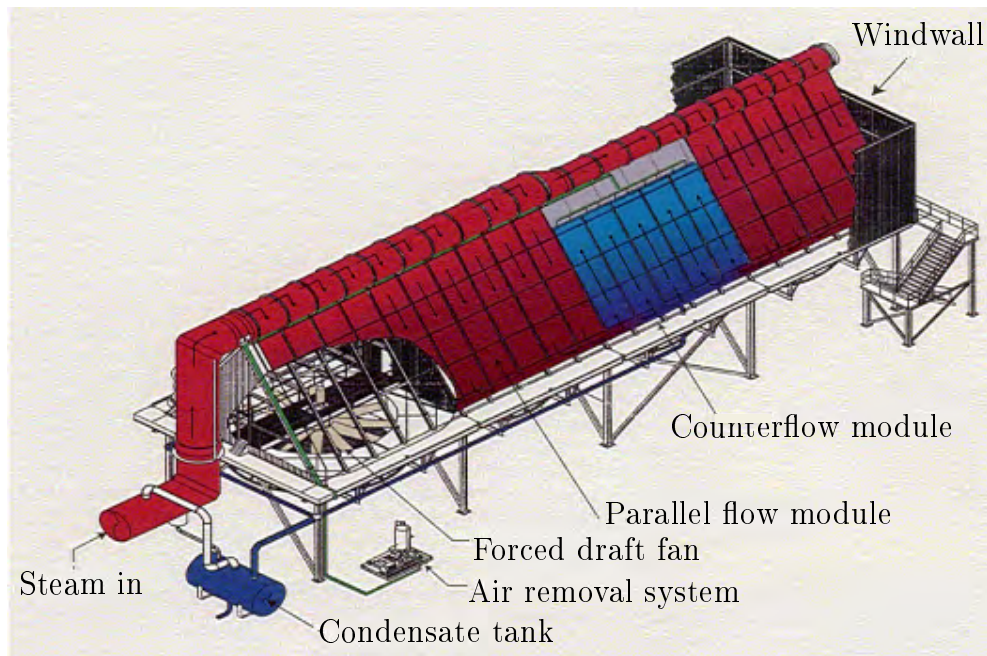


Figure 2.2: Illustration of ACC unit arrangement (Phala *et al.*, 2007).

The ACCs in South African power stations make use of inclined A-type arrangements, using a forced draft to initiate heat exchange. The inclined arrangement assists with drainage and it reduces the required surface area (Kröger, 2004). The forced draft is produced by a system consisting of a motor, gearbox, fan-bridge and a fan, as illustrated in Figure 2.3. Heat from the condensing steam is rejected to the environment via finned tubes. The axial flow fans mounted below the A-frame force a stream of air over the finned pipes, assisting in the heat exchange process (Bredell *et al.*, 2006). The forced convection induced by the axial flow fans is essential to the overall heat exchanger efficiency as the ambient air temperature does not suffice in warm climate areas.

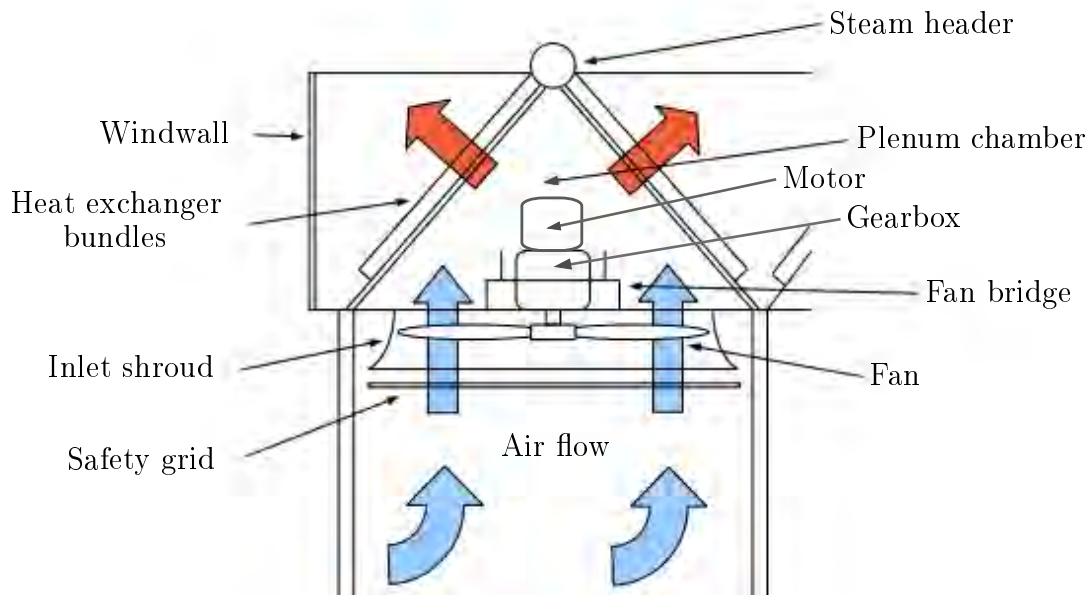


Figure 2.3: ACC with inclined A-type frame design (Muiyser, 2012).

2.1.3 Electric Motor

Electric motors used in ACCs are chosen based on system requirements, i.e. gearbox power rating, shaft thickness and the torque range of the gearbox-fan system. For the purpose of this study the focus is on alternating current (AC) motors i.e. synchronous motors and induction motors.

The main difference between synchronous and induction motors is the rotor. The synchronous motor rotor is powered by a direct current (DC) power supply, or it is made up of permanent magnets. Applying a DC current to the rotor is the most common practice. The motor is then doubly excited, meaning it requires power from two sources (DC power for the rotor and AC power for the stator). This complicates the motor build but the result is that the rotation of the rotor and the rotating magnetic field of the stator are synchronized (El-Hawary, 2002). Synchronous motors have a higher efficiency than induction motors because there are no rotor losses (Boglietti *et al.*, 2005). The speed of the synchronous motor is not dependent on the load of the rotor, given that it remains within the motor ratings. The motor requires a variable frequency drive to achieve variable speed and it is not self starting. Due to their complicated build, synchronous motors require regular maintenance.

Induction motors are more commonly used than synchronous motors because of simplicity, reliability and low cost. The induction motor works by supplying an AC current to the stator, which in turn transfers it to the rotor by transformer action (induction) (El-Hawary, 2002). A 3-phase induction motor is self starting and does not require a starting device. Induction motors are very attractive for industrial use as they require minimal maintenance,

are easily manufactured, very rugged and can operate in most environments. Induction motors are available in a wide range of sizes and are less expensive than synchronous motors. However, they come with disadvantages of their own, i.e. the power factor is always lagging and generally between 0.85 to 0.9 at full load. They also draw a high starting current to overcome the rotor inertia. A typical horizontal induction motor assembly is shown in Figure 2.4.

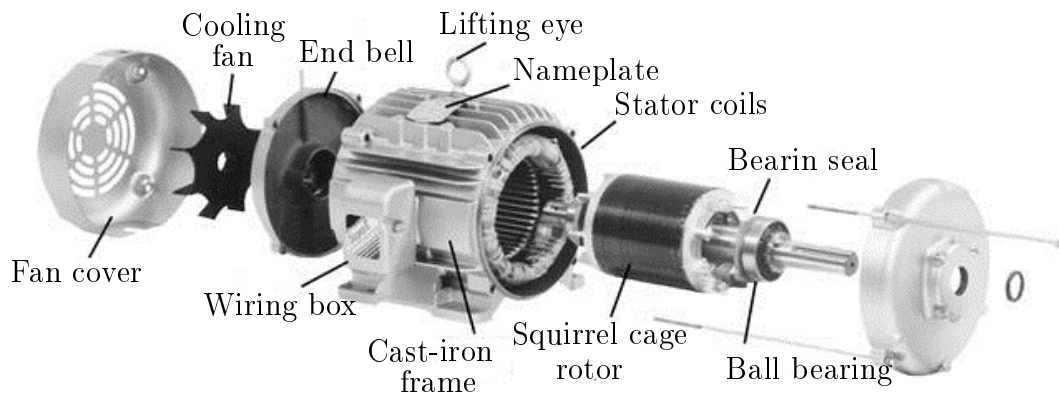


Figure 2.4: Induction motor assembly, Lin (2014).

The motors used in the ACC of Matimba power station are rated for 280 kW, 1489 rpm and are 96.1 % efficient (CMG Performance Report). Polak (1999), from Neale Consulting Engineers Ltd., found that oversized motors are often chosen to ensure shaft rotation during unexpected loads. This could lead to excessive loads from the input side at start-up. Excessive starting torque may alter the system resonant characteristics (Polak, 1999). Soft-start technology is generally implemented in large induction motor systems where a direct on-line starter may cause a voltage dip during start-up (Pillay *et al.*, 2009). The motors used in the ACC of Matimba Power Station are directly connected on-line, based on the start-up time measured by Muiyser (2012). Using a direct on-line starter for the 288 motors used in the ACC of Matimba power station saves costs and simplifies the system for maintenance purposes. A study on soft starting large induction motors at constant current and minimized starting torque was conducted by Zenginobuz (2001). This study states that motor starters employing power semiconductors (soft-starters) are being used increasingly to replace electromagnetic line starters (direct on-line).

2.1.4 M4ACC Gearbox

The ACC of Matimba Power Station makes use of a Hansen M4ACC gearbox with a torque range of 20 kN · m to 70 kN · m (Hansen Industrial Transmissions, 2004). This gearbox is a two-stage, vertical axis gearbox and can be viewed in Figure 2.5. Heavy duty tapered, cylindrical or spherical roller bearings are used to position the shafts. The gearbox housing is made from grey pearlitic

cast iron. Mineral oils are used as lubricant for the M4ACC gearbox with a pump lubrication system for the upper bearings. The gearbox relies on natural cooling or additional fan cooling to dissipate excess heat that is generated.

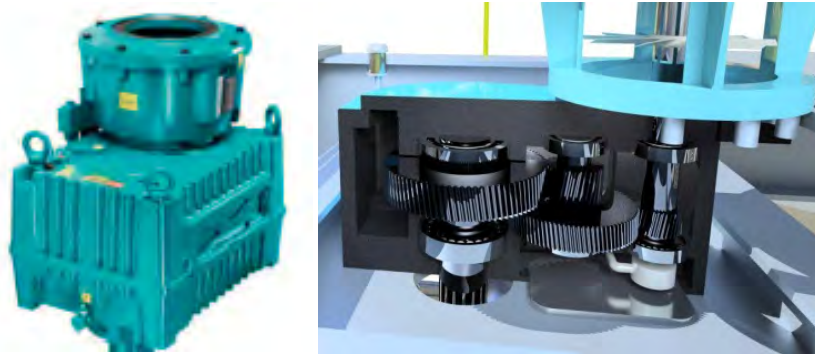


Figure 2.5: Two-stage Hansen M4ACC gearbox and gears (Hansen Industrial Transmissions, 2004)(Goldschagg, 2013).

2.1.5 Fan and Air Circulation

The heat exchanger is assisted by axial flow fans that blast ambient cooling air over the finned steam pipes. This system is open to the environment and ambient wind conditions have to be considered. Liu *et al.* (2009) found that fans used at power station ACCs are sensitive to ambient wind conditions. A problematic phenomenon, known as hot air recirculation, occurs when cool ambient air is heated after flowing over the finned steam pipes and recirculated into the fan inlet by adverse wind conditions. Ideally, cool air must be sucked into the inlet of the fans, forced over the finned steam pipes and ejected as hot air away from the ACC. Figure 2.6 illustrates ideal wind conditions as well as hot air recirculation. The amount of hot air that is recirculated by the ACC can be lowered by increasing the height of the wind-wall surrounding the ACC, and by increasing the speed of the edge fans.

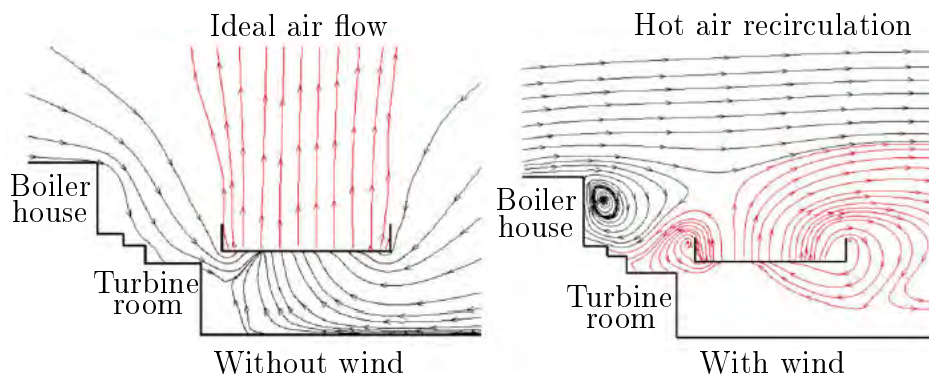


Figure 2.6: Ideal circulation and hot air recirculation in an ACC (Liu *et al.*, 2009).

It is suspected that adverse wind conditions cause the fans to load the gearboxes in an unexpected manner. Bredell *et al.* (2006) found that inlet flow losses increase as flow separation takes place at the fan inlet and that other problems include maldistribution of air into the fan and off-axis inflow conditions. Muiyser *et al.* (2014) confirmed that adverse wind conditions in the region of the power station have an impact on fan blade loading. A Matimba ACC fan, shown in Figure 2.7, has a diameter of 9.125 m and blade loading would cause bending stresses to develop in the output shaft of the gearbox.

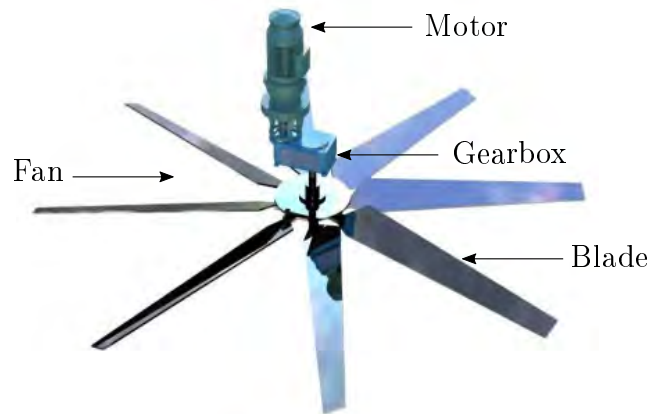


Figure 2.7: Illustration of a single fan (Goldschagg, 2013).

2.2 Gearbox Failures

The basic two-stage step-down gearbox consists of an input and output shaft connected by an intermediate gear, illustrated in Figure 2.8. Various types of gears are used in the connecting gear mechanism viz. spur gears, helical gears, bevel gears and worm gears. A guide for gear design is given in Appendix A.

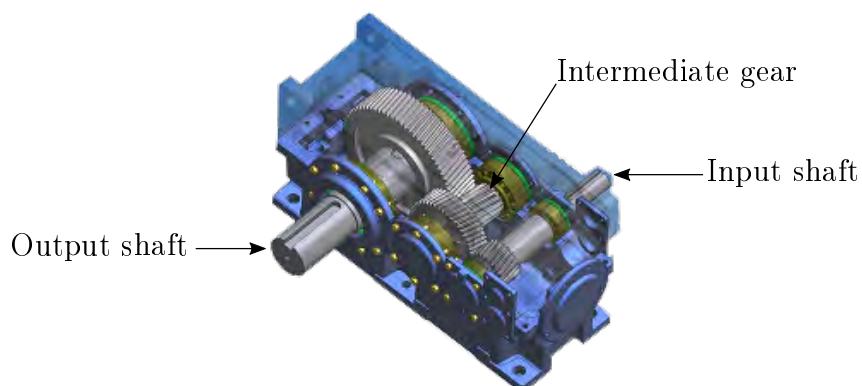


Figure 2.8: Two-stage industrial gearbox.

Gearbox failure is a harsh reality that the industry is faced with on a daily basis. The annual ACC gearbox failures at Matimba power station—out of 288 gearboxes—was documented by Goldschagg (2013) in Figure 2.9. It can be difficult to identify the root cause of a specific gearbox failure, as the end result is often a few broken pieces of metal within a gearbox, as shown in Figure 2.10.

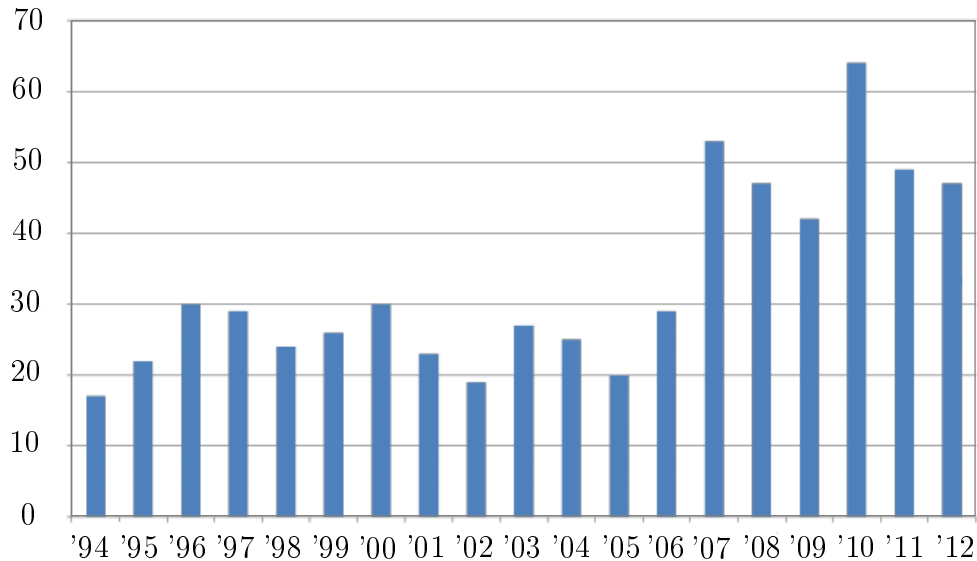


Figure 2.9: Gear failures at Matimba power station from 1994 to 2012 (Goldschagg, 2013).



Figure 2.10: Perpendicular shaft multi-stage industrial gearbox after axial failure

The most common cause of gearbox failures is the bearings, however they may not always be the root cause. A failure analysis performed by SKF on

bearing failure occurrence found that bearing failure is mostly caused by adverse external factors (Hameed *et al.*, 2009). The actual root cause may be misalignment, thermal instability, torsional or lateral vibrations, unexpected loads, and lubrication or contamination (Polak, 1999).

2.2.1 Torsional and Lateral Vibration

If gears were rigid, correctly spaced and had perfect involutes, no vibration would be generated during meshing (Smith, 1999). Vibration can contribute to gear failure. Transmission error is defined as the variation of the output gear position relative to the input gear position, and it is responsible for generating mesh vibration. In practice gearbox vibrations can be measured with ease and the cause of most vibrations can be identified (Luchetta, 2014). External factors also contribute to gearbox vibrations and should be considered when analysing gearbox vibrations (Bartelmus and Zimroz, 2008).

2.2.2 Bearings

Rolling bearings have been found to be sensitive to lubrication deficiencies, debris and vibrations (Polak, 1999). These bearings operate under high contact stress and are susceptible to debris and unexpected external loading. Bearing damage can be detected by unusual functional behaviour of the component. Flaked running surfaces from material fatigue or an alteration in radial clearance from wear cause distinct running noise (Brandlein *et al.*, 1995). Ai (2001) conducted a study where quantitative relationships are drawn between debris induced bearing fatigue and bearing life reduction. It has been estimated that 75% of premature bearing failure is debris related (Ai, 2001).

Classical fatigue damage begins with minute cracks that form under the surface. Over time these cracks propagate to the surface and cause flakes of steel to break loose. Continual service of the bearing after flaking leads to disturbed rolling conditions. This in turn could lead to the bearing ring fracturing completely (cage fracture) from the pressures experienced when running over a large flake. Once the subsurface cracks have been initiated, the lifespan of the bearing decreases (Harris and Kotzalas, 2007). Figure 2.11 shows how microscopic debris from flaking or lubricant become embedded in the rollers.

Wear is a common cause of bearing failure and is mainly caused by contamination of the bearing lubricant. Severe wear causes the clearance to increase and gives the surfaces a dull appearance. Rust could lead to wear and has the potential to form within the bearing if the bearing temperature is below the ambient temperature, specifically in downtime. Figure 2.12 illustrates a severe case of bearing failure from large scale gearbox use.

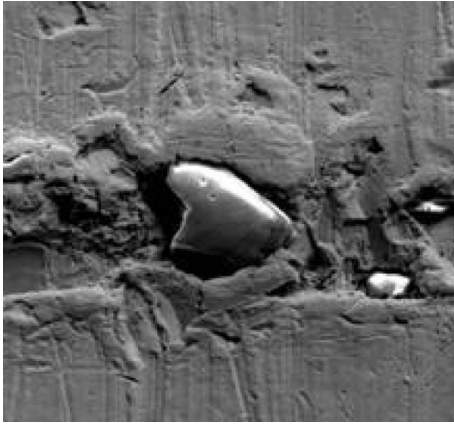


Figure 2.11: Particle indentation onto roller.



Figure 2.12: Advanced roller bearing failure.

2.2.3 Lubrication

There are various types of lubricant viz. liquid lubricants, greases, polymeric lubricants and solid lubricants (Harris and Kotzalas, 2007). Liquid lubricants are generally used for gears and bearings while greases are used more for sealing. Lubrication is essential as insufficient lubrication or interrupted lubrication will almost certainly result in failure. Proper practices include using the appropriate lubricant for the specific application, ensuring that the lubricant is clean and maintaining a sufficient supply thereof (Luchetta, 2014).

The lubricant film separates the surfaces in contact and having a poor lubricant film would cause cracks to develop closer to the surface (Brandlein *et al.*, 1995). Scoring is a failure that is associated with film breakdown, resulting in metal-to-metal contact, as well as high temperatures that further result in gear tooth surface damage (Budynas and Nisbet, 2015). Abrasive wear on the other hand occurs when a lubricant is contaminated with foreign material. An example of microscopic surface deformation caused by particles found in contaminated lubricant is shown in Figure 2.11. Lubricant analysis can deliver valuable insight on the purity thereof and of the operation of the gearbox.

2.2.4 Unexpected Loads

There are a multitude of reasons that can cause unexpected gearbox loading. Flexible couplings, especially gear couplings, can cause gear teeth damage or bearing failure due to considerable radial and axial loads. Oversized electric motors are frequently specified and can produce immoderate starting torques. Using soft-start technology like variable speed drives, can improve the start-up characteristics, but in general large motors are harmful to gears (Polak,

1999). In the case of ACC gearboxes, dynamic wind conditions could also cause unexpected loading from the fan.

2.2.5 Thermal Instability

Thermal instability is a failure mode that is very difficult to diagnose, as the failed components are usually completely destroyed by the time of failure. This mode of failure occurs when a large temperature difference builds up between the shaft inside a bearing and housing outside a bearing. This temperature difference causes the bearing to lose internal clearance and it becomes excessively pre-loaded (Polak, 1999). Thermal instability is most commonly associated with high speed shafts and it occurs shortly after start-up—usually in colder weather. This is because the temperature difference builds up to a maximum shortly after start-up before stabilizing over time (Polak, 1999). This failure may also be found later in the lifespan, as bearing or lubrication degradation may cause increased rates of heat generation.

2.3 Measurement System

The system used for the measurements taken in this study is discussed in this section. Background is given on each component of the system viz. strain gauges, accelerometers, proximity sensors and the data acquisition hardware.

2.3.1 Strain Gauge

The strain gauge is a resistive elastic unit whose deformation can be related to material strain. There are different types of strain gauges viz. electric resistance, capacitive, inductive, mechanical, optical, piezoelectric, and semi-conductive. The different types of strain gauges are discussed in detail by Hoffmann (1989). The electric resistance strain gauge is most commonly used as it has a low cost and a high accuracy (eFunda, 2016). The relationship between applied strain and change in electric resistance is expressed as

$$\epsilon = \frac{\Delta R}{k \cdot R}, \quad (2.1)$$

with k being the gauge factor. The derivation of Equation 2.1 is illustrated in Appendix B.

For typical strain gauges the $\Delta R/R$ values range from 10^{-3} to 10^{-6} which relate to a ΔR range of 0.0007Ω to 0.7Ω for a 350Ω strain gauge (Cimbala, 2013). Ohmmeters can not accurately measure resistances in this range. Manojlovic and Jankovic (2013) discuss the use of bridge circuits to aid in the accurate measurement of small resistances. The bridge circuits that are used to measure low strain gauge resistances are the Four-wire Ohm circuit, the

Chevron bridge and the Wheatstone bridge. According to Application Note 290-1 the Wheatstone bridge is most frequently used for strain gauge application because of its outstanding sensitivity, and it is depicted in Figure 2.13. The Four-wire Ohm circuit is an expansion of the Wheatstone bridge, and the Chevron bridge is used on rotating machinery when slip rings are used to transmit data.

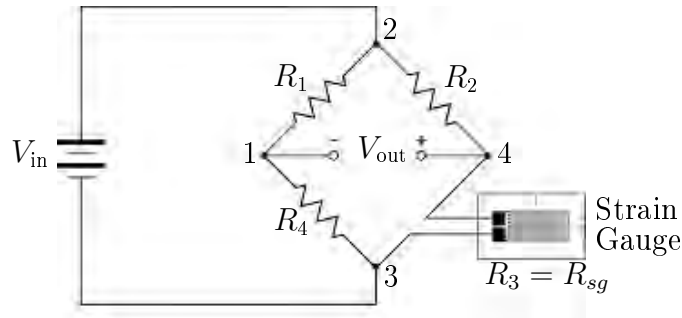


Figure 2.13: Illustration of the Wheatstone bridge and a strain gauge (McGinty, 2012).

Hoffmann (1986) describes the Wheatstone bridge as comparing unknown resistances to well defined resistances. From Figure 2.13, an input voltage is applied across nodes 2 and 3, while the output voltage is measured across nodes 1 and 4. If the bridge is perfectly balanced i.e. $R_1 = R_2 = R_3 = R_4$, the output voltage will be equal to zero. Therefore, when the resistor values change due to strain, an output voltage will be measured. The relationship between voltage and resistance can be expressed as

$$\frac{V_{out}}{V_{in}} = \frac{1}{4} \cdot \left(\frac{\Delta R_1}{R_1} - \frac{\Delta R_2}{R_2} + \frac{\Delta R_3}{R_3} - \frac{\Delta R_4}{R_4} \right) \quad (2.2)$$

neglecting second order factors as it is assumed that ΔR_i is much smaller than R_i . Substituting Equation 2.1 into Equation 2.2 gives

$$\frac{V_{out}}{V_{in}} = \frac{k}{4} \cdot (\epsilon_1 - \epsilon_2 + \epsilon_3 - \epsilon_4) = \frac{k}{4} \cdot \epsilon_{total} \quad (2.3)$$

which is used to relate the measured voltage to strain. The strain gauges are positioned to measure equal absolute strains i.e. $|\epsilon_1| = |\epsilon_2| = |\epsilon_3| = |\epsilon_4|$. Equation 2.3 gives a combined strain that acts as the total strain measured by the Wheatstone bridge. Hoffmann (1996) discusses the installation of strain gauges regarding the specific application, connecting the wires, testing the strain gauges and protecting them from the environment. Muiyser (2012) made use of strain gauges to measure shaft strains on an ACC gearbox.

2.3.2 Vibration and Accelerometers

In recent times machinery has become more intricate and operate faster, leading to an increase in associated vibration problems. The need for a better understanding of the causes of vibration and the dynamic response of structures has thus risen. Serridge and Licht (1987) discuss the four broad areas of vibration measurement i.e. vibration testing, machine health monitoring and fault diagnosis, structural analysis and human vibration measurement.

An accurate and reliable vibration transducer is required to measure such vibration signals, and the piezoelectric accelerometer has proven to be the optimum choice thereof (Serridge and Licht, 1987). Advantages of this transducer include: usage over a wide range of frequencies; accurate vibration measurements that are possible in various environmental conditions; no external power supply is required; and it is extremely compact.

The transducer is made up of crystalline material such as quartz, or a polarized ceramic material such as barium titanate. For an accelerometer, an electric signal is produced by the transducer when some mechanical transient force is applied to it (Redwood, 1961). Typically, a mass is placed on top of the piezoelectric crystal, which then places a load on the crystal as the accelerometer moves (Illustrated in Figure 2.14). The electric signal is then related to the physical acceleration of the sensor.

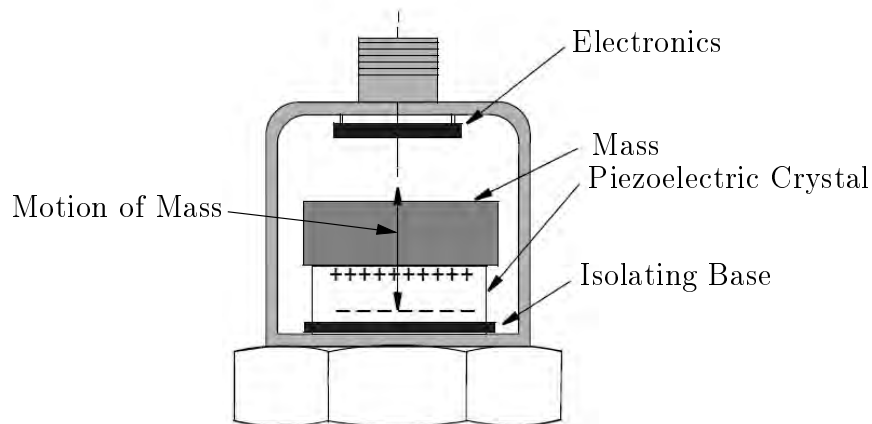


Figure 2.14: Simplified depiction of a piezoelectric transducer used in an accelerometer.

Health monitoring and fault diagnosis is performed in this project. The frequency components in the vibration signal are analysed by inspecting the frequency spectrum of the vibration data. Applying a Fast Fourier Transform to the vibration signal, allows the researcher to observe the frequencies of vibration (Harcarik *et al.*, 2012). This area of vibration measurement is widely used for fault detection in gears and bearings. McFadden and Smith (1984)

made use of this technique to identify a single point defect on the inner race way of a rolling element bearing, while Wang and McFadden (1993) later used a spectrogram as a tool for early failure detection in gears from vibration analysis. Frequency spectrum plots are used in this study to identify the operational vibration frequencies present in the M4ACC gearbox.

2.3.3 Signal Transmission and Recording Hardware

The two primary problems with measuring strain on rotating shafts are the positioning of the strain gauges, and the transmission of the measured signal from the rotating shaft to the recording hardware (Folta and Hrudickova, 2013). The positioning of the strain gauges is only problematic for the input shaft and it is discussed in detail in Chapter 3. The transmission and recording of the measured signal is discussed in this section.

The measured signal can be transmitted from the shaft to the recording apparatus by means of slip-rings (contact transmission) or telemetry (non-contact transmission). The sliding motion of the slip-rings may cause noise on the signal and require free space around the shaft (Folta and Hrudickova, 2013). Telemetry is used for the measurements in this study because of spacial limits around the shafts and because of lower signal noise.

A SG-Link-LXRS and a V-Link-LXRS are used as the telemetry devices that are responsible for transmitting the signal from the rotating shaft. The SG-Link-LXRS is smaller than the V-Link-LXRS, but can only transmit data from a single full bridge SG configuration, making it suitable for use on the input shaft where torsion is measured and space around the shaft is limited. The V-Link-LXRS is required for the output shaft as three full bridge SG configurations are used i.e. two for bending and one for torsion. Figure 2.15 and 2.16 shows both telemetry devices.



Figure 2.15: SG-Link-LXRS used to transmit the signal from the gearbox input shaft.



Figure 2.16: V-Link-LXRS used to transmit multiple signals from the gearbox output shaft.

The SG-Link-LXRS and V-Link-LXRS transmit the measured analogue signal, from the Wheatstone bridge by digitizing it and transmitting it to the

WSDA-Base-104 station via radio frequency. The WSDA-Base-104 station can then convert the digital signal back to an analogue voltage signal, ranging from 0 V to 3 V, which in turn is related to the relevant measured quantity. An important limitation of the WSDA-Base-104 station is that it can only stream data from one link at a time. This test setup thus requires two WSDA-Base-104 stations. Figure 2.17 shows the WSDA-Base-104 station.

The measured shaft strains are then synchronised with the shaft speed and gearbox vibration measurements, using a QuantumX MX1601B data synchronization apparatus. Analogue data signals are connected to the QuantumX MX1601B, where after the QuantumX MX1601B records the signals onto the same time stamp. The QuantumX MX1601B is shown in Figure 2.18.



Figure 2.17: Illustration of the WSDA-Base-104 station used to receive the signals from the SG-Link-LXRS and V-Link-LXRS.



Figure 2.18: QuantumX MX1601B data acquisition (DAQ) apparatus, used to synchronise analogue signals from multiple sensors.

2.3.4 Integration of Measurement System

An illustration of the design of the measurement system used in this project is shown in Figure 2.19.

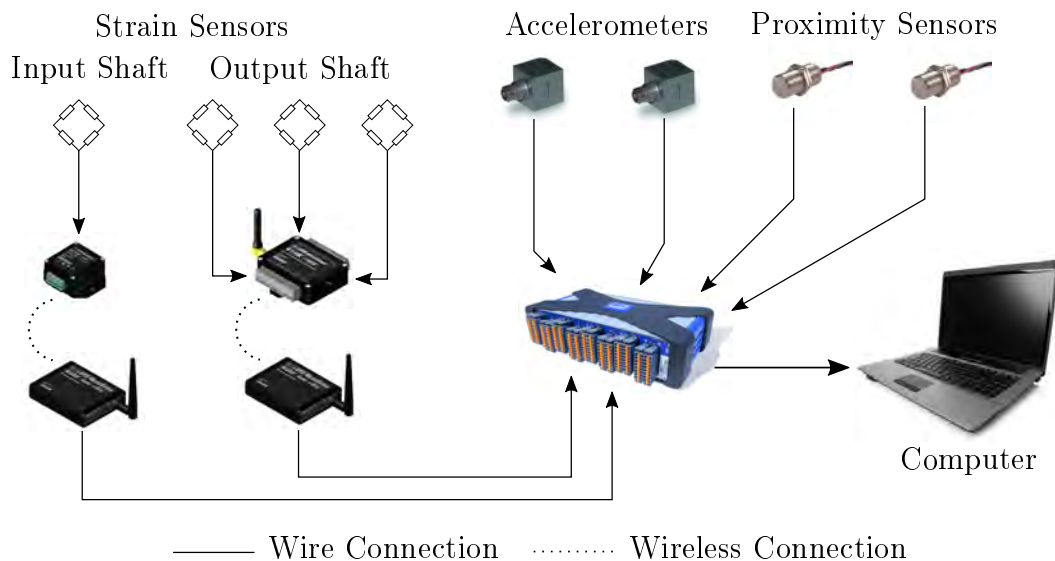


Figure 2.19: Integrated measurement system.

The measurement system used by Muiyser (2012) is modified for this study to incorporate gearbox vibration and input shaft measurements, and to exclude blade loading and air-flow measurements. The proximity sensors work by outputting an increased voltage each time a piece of magnetic material passes them, and they are used to measure the shaft speeds. Two PCB-Accel-333B32 are used as the gearbox vibration sensors. The accelerometers and the proximity sensors are fixed to the static gearbox and can be connected to the QuantumX MX1601B directly. The software required to operate this system is: Node Commander 2.10.0 for the WSDA-Base-104 stations and Catman Professional 5.0 for the QuantumX MX1601B.

2.3.5 Reliability of Strain Measurements

According to Folta and Hrudickova (2013), strain gauges should be positioned on areas without grooves and discontinuities to measure true representative data. This is not a problem when measuring strain on the output shaft, but strain measurements on the input shaft may be compromised by the close proximity of the keyway.

This problem can be solved with an accurate finite element method model (FEM), as the FEM model can be used to predict the strain that would be measured by strain gauges in the relevant position. Göksenli and Eryürek (2009) used a FEM model to analyse the stress developing around the keyway of an elevator shaft, which has a similar geometry to that of the M4ACC input shaft. In theory, a calibration curve could then be established relating torsion applied to the input shaft and strain measured near the keyway.

2.4 Application of Literature Review

This chapter delivered background on the functionality of an ACC which is installed in a large coal fired power station. The specific components of the ACC are discussed, with focus being placed on the causes of ACC gearbox failures. The project investigates two of these causes of gearbox failure, i.e. unexpected loading or torsional and lateral gearbox vibrations.

The measurement system that is discussed in Section 2.3 can be used to quantify the effect of the electric motor and of the fan on gearbox loading. Past research performed by Muiyser (2012) confirmed that a similar measurement system was used to measure operational loads in an ACC. Section 2.3 gives thorough background on the workings of the system and how it is designed for this specific investigation.

Chapter 3

Quantification of Measurement Accuracy

Calibration of test equipment improves the quality of the data measured and is a necessity when high accuracy data is expected. The equipment used on site for this research project include accelerometers, strain gauges, proximity sensors and a thermal camera. The accelerometers are calibrated with a SV111 Vibration Calibrator and the calibration is shown in Appendix C.1. The proximity sensors do not require calibration for the purpose of this study and the thermal camera used in this study makes use of its own on-board calibration. The integrated strain measurement system was not calibrated on site as it is was not practical to simulate known loads on the input and output shaft of the gearbox. The goal of this chapter is to predict the accuracy of the strain measurement system, with focus placed on input shaft measurements. This is done with finite element analysis, statistical analysis and laboratory testing.

3.1 Background

The data obtained from the M4ACC gearbox is measured on site in the ACC of Matimba Power Station. The M4ACC gearbox is a multi-stage step-down gearbox that is connected to a motor by means of a high speed coupling, and to a fan by means of a low speed coupling, as shown in Figure 3.1. The integrated strain measurement system consists of strain gauges, a link (V-Link-LXRS and SG-Link-LXRS), two WSDA-Base-104 stations and a laptop, shown in Figure 3.2. Torsional strain gauges are placed on both the input and output shafts, while bending strain gauges are placed on the output shaft only.

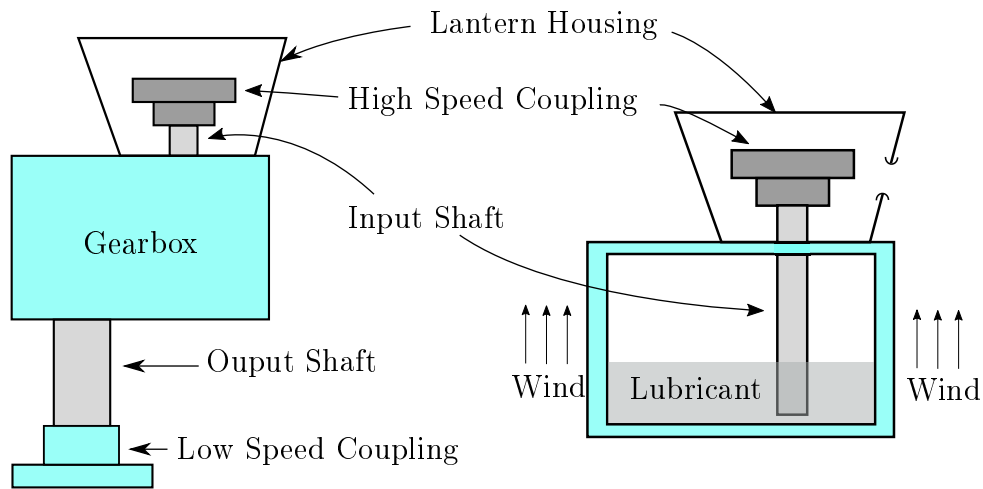


Figure 3.1: Input and output shaft of the M4ACC gearbox, and an illustration of the input shaft with regard to wind and lubricant.

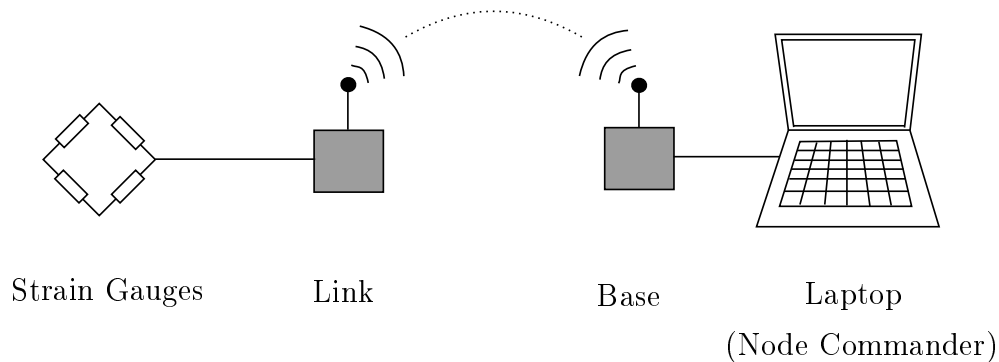


Figure 3.2: Strain measurement system.

The strain gauges can be positioned on the output shaft in such a way that they are subjected to homogeneous stress. This is due to the size of the available area that the strain gauges could be placed, and the distance between the strain gauges and any edge effects. For the purpose of relating measured strain to either torque or a bending moment on the output shaft of the gearbox, it is acceptable to approximate the output shaft as a simply supported cantilever beam with a circular cross section. This approximation allows the researcher to make use of fundamental strength of material equations from Hibbeler (2013) to relate strain to torque, or to a bending moment. The effect that the material properties of the output shaft will have on the torque and bending measurements is analysed statistically in Section 3.5.

Strain measurement on the input shaft is complicated by factors that have a negligible effect on the strain measured on the output shaft. The input shaft has limited space available for the strain gauges, resulting in the strain gauges to be positioned near the keyway, as shown in Figure 3.3. In practise a sleeve

is used as a safety measure to prevent the coupling from sliding down the shaft. Holes had to be machined into the sleeve to allow the strain gauges to be placed on to the input shaft, as shown in Figure 3.4. Refer to Appendix G.1 for photographs of the input shaft and the sleeve.

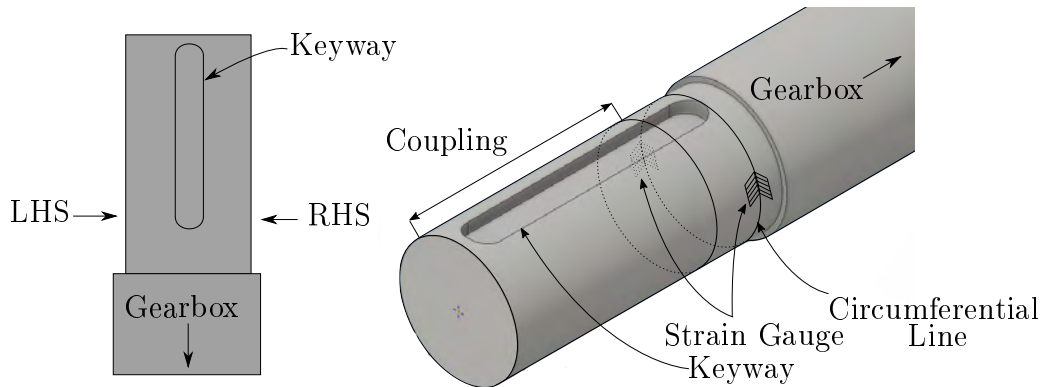


Figure 3.3: Input shaft of the M4ACC gearbox with strain gauge rosettes positioned in the ideal position, and illustration of left-hand-side (LHS) and right-hand-side (RHS) convention.

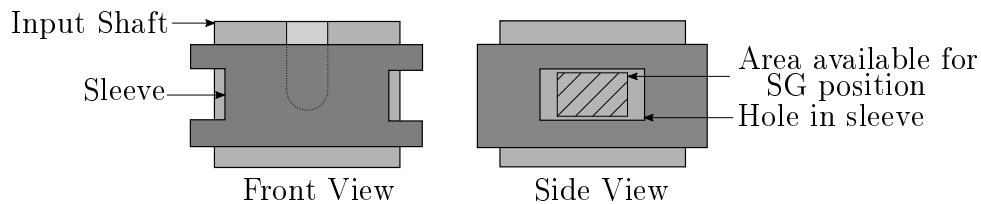


Figure 3.4: Illustration of sleeve used to prevent coupling from sliding on the input shaft.

The manner in which torque is applied to the input shaft is not exactly known. The high speed coupling is held in position by means of a key and a transition fit, which results in non-homogeneous stress distribution in the vicinity of the strain gauges. The effect that the material properties of the shaft will have on the torque measurements is statistically analysed in Section 3.5. The input shaft is not well ventilated and it is in direct contact with the gear lubricant, as shown in Figure 3.1. It is expected that the temperature of the input shaft will have a further effect on the material properties of the shaft. This will be investigated by means of a vibration analysis in Section 3.6.

To ensure that accurate and reliable strain data is obtained from the input shaft measurements, it is required to perform a calibration between torque applied to the input shaft and the strain measured by the strain gauges. Strain gauge measurements are taken on an actual input shaft in Section 3.2 to investigate the linearity of the torque-strain curve. Measurements taken with

digital image correlation (DIC) is used to compare the surface displacement of the regions around the keyway in Section 3.3. The shaft is then modelled using finite element method (FEM) in Section 3.4. For further referral it is important to take note of the LHS and RHS convention, as illustrated in Figure 3.3.

3.2 Strain Gauge Measurements

Manojlovic and Jankovic (2013) discuss the Kelvin double bridge, the Chevron bridge and the Wheatstone bridge. The Wheatstone bridge circuit, the most commonly used circuit for the purpose of experimental strain measurements, is used in this study (Manojlovic and Jankovic, 2013). Figure 3.5 shows the Wheatstone bridge with four active strain gauges. V_{in} is the constant supply voltage of the circuit, V_{out} is the measured output voltage and R_{1-4} is the resistance of each gauge, which is directly proportional to the strain (ϵ) it experiences. The experimental technique performed by Muiyser (2012) with strain gauges on an operational ACC unit using the fundamental theory described by Hoffmann (1986), is replicated in this study.

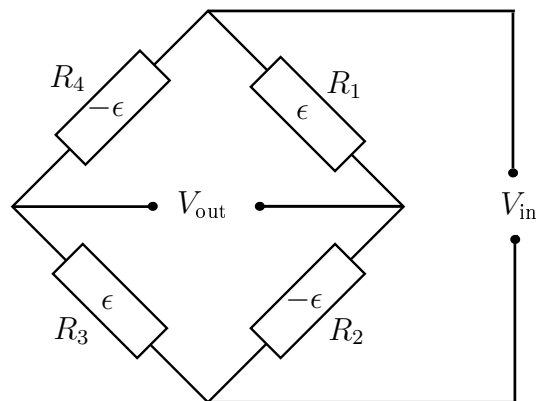


Figure 3.5: Wheatstone bridge circuit with four active strain gauges.

The strain gauges are mounted on rosettes to eliminate human error as much as possible. The half-bridge torsional strain gauge rosette used in this experiment, aligns two strain gauges at a 90° angle with each other. The practical setup required the use of two half-bridge strain gauge rosettes. The rosettes are placed on either side of the shaft being tested to form a full bridge, eliminating bending and temperature effects (Hoffmann, 1986). Figure 3.6 shows how a torsional strain gauge rosette is mounted on the RHS of the keyway. The rosette is positioned onto the shaft so that each strain gauge is aligned at a 45° angle with the shaft axis to measure torsional strain, as shown in Figure 3.7 (Hoffmann, 1986).

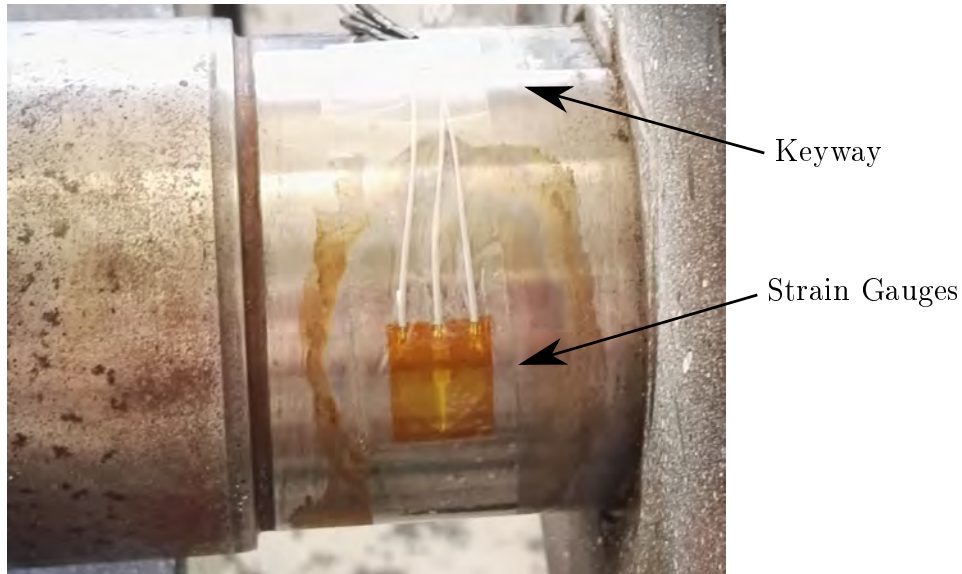


Figure 3.6: Torsional strain gauge rosette mounted on the RHS of the keyway.

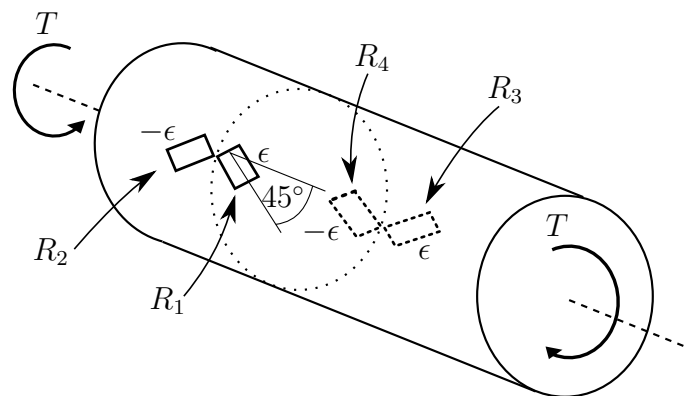


Figure 3.7: Full bridge strain gauge configuration used for torsional strain measurement.

The input shaft of the M4ACC gearbox experiences torque in excess of $1500 \text{ N} \cdot \text{m}$ when installed in an operational ACC. The shaft is placed in two plumber blocks for stability, while fixing one end of the shaft to the work bench by means of a weld. This allows for a torque to be applied at the opposite end of the shaft while measurements can be taken near the region of the keyway. The shaft mounting can be viewed in Figure 3.8.

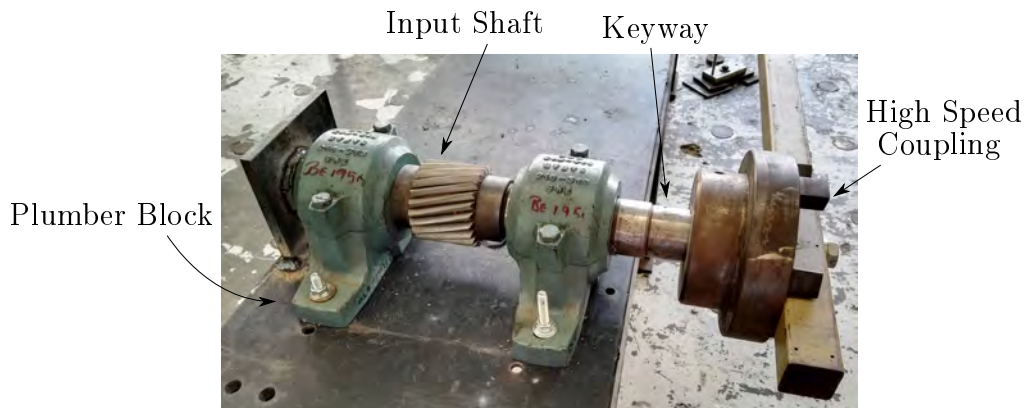


Figure 3.8: Input shaft mounted onto the work bench for laboratory calibration.

A moment arm is used to apply the torque to the shaft. The force at the tip of the moment arm is applied using a wire tensioner, which connects the tip of the moment arm to the ground via a load cell. The load cell is calibrated before the test and the calibration is shown in Appendix C.2. The experimental setup can be viewed in Figure 3.9.



Figure 3.9: Moment arm under full load connected to the input shaft and the work bench.

3.2.1 Experimental Procedure

Node Commander is the software that is used to communicate with the strain gauges from the computer (Node Commander 2.10.0), via the V-Link-LXRS. Once the strain gauges have been installed, they are connected to a computer and calibrated by performing an instrument scaling shunt calibration,

as described in TN-514. In what is described as instrument scaling shunt calibration, the strain gauge circuit output is simulated by subjecting a certain strain gauge to a predetermined strain. Measurements are taken in torque intervals of $200 \text{ N} \cdot \text{m}$, from $0 \text{ N} \cdot \text{m}$ to $1600 \text{ N} \cdot \text{m}$. This is repeated three times, ensuring an acceptable average is used for the torque-strain curves.

3.2.2 Torsional Strain Theory

The torque measured by the strain gauges is obtained by relating physically measured torsional strain to torque with equations from the fundamental theory of strength of materials (Hibbeler, 2013). Starting with Hooke's law for shearing,

$$\tau_{\max} = G\gamma_{\max}, \quad (3.1)$$

and equating it to the torsion equation,

$$\tau_{\max} = \frac{T_{\max}r}{J}, \quad (3.2)$$

it is possible to relate torque to shear strain as

$$G\gamma_{\max} = \frac{T_{\max}r}{J}. \quad (3.3)$$

$$G = \frac{E}{2(1 + \nu)} \quad (3.4)$$

$$J = \frac{\pi r^4}{2} \quad (3.5)$$

Then, by substituting Equation 3.4 and Equation 3.5 into Equation 3.3 it is possible to express torque in terms of shear strain as

$$T_{\max} = \frac{E\pi r^3}{4(1 + \nu)} \cdot \gamma_{\max}. \quad (3.6)$$

Strain gauges measure normal strain in the chosen direction, and not shear strain as is required for Equation 3.6. It would be convenient to relate torque to the measured quantity of the strain gauges. Due to the large size of the shaft, it can be assumed that the strain gauges measure the strain that is experienced by an infinitely small stress element on the surface of the shaft. Figure 3.10 shows an exaggerated depiction of a stress element (A) on the outer surface of a shaft in torsion. Element A is a pure shear element, and because the element is located on the outer radius of the shaft, it experiences the maximum shear stress (τ_{\max}) of the shaft. The resulting principal stresses of element A, are depicted in Element B of Figure 3.10, where it can be seen that the principal planes are aligned at 45° angles with the shaft axis.

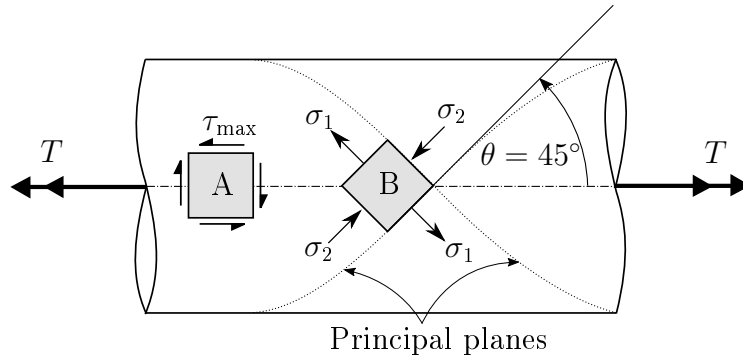


Figure 3.10: Plane stress element (A) and equivalent principal stress element (B) on the outer surface of a shaft subjected to torsion.

The principal stresses can be related to the principal strains by,

$$\epsilon_{1,2} = \frac{1}{E}(\sigma_{1,2} - \nu\sigma_{2,1}), \quad (3.7)$$

and occur along the same principal planes. The strain gauges are positioned along the principal planes to measure the principal strains. When placing a circular shaft in torsion, plane stress and plane strain can be assumed simultaneously. Mohr's circle for plane strain, as shown in Figure 3.11, can then be used to relate the principal strains that are measured by the strain gauges to the maximum shear strain (τ_{\max}) that is shown in Equation 3.6.

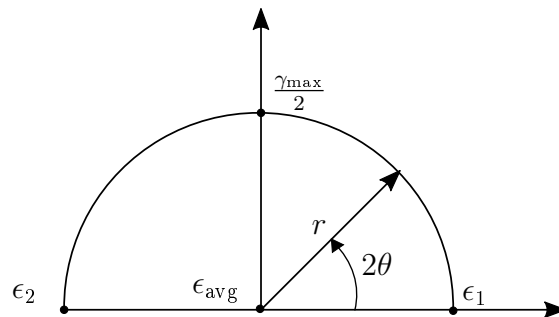


Figure 3.11: Mohr's circle for plane strain.

Figure 3.11 indicates that,

$$\frac{\tau_{\max}}{2} = \epsilon_1 = -\epsilon_2. \quad (3.8)$$

The equivalent torque experienced by the shaft can then be related to the measured strain as,

$$T = \frac{E\pi r^3}{2(1+\nu)} \cdot \epsilon, \quad (3.9)$$

where

T is the equivalent torque experienced by the shaft [$\text{N} \cdot \text{m}$],

E is elastic modulus for the specific shaft material [GPa],

r is the radius of the shaft [m],

ν is Poisson's ratio of the shaft material,

ϵ is principal strain measured by the strain gauges [$\mu\text{m}/\text{m}$].

It should be noted that the use of Equation 3.9 assumes a homogeneous circular shaft which is not the case when referring to the input shaft shown in Figure 3.3. Equation 3.9 can be used to calculate the torque on the shaft given the measured strain. This torque can then be compared to the known applied torque, to quantify the error between the applied torque and the measured torque. The combined effect that the keyway and manner of torque transfer will have on the measured shaft torque, will be observed in this experiment.

It is not possible to know the exact value of the elastic modulus and Poisson's ratio of the shaft, without performing tests on a sample of the shaft. The accepted approach is to use the average value of the elastic modulus and Poisson's ratio for case hardened steel. An elastic modulus value of 207 GPa and a Poisson's ratio of 0.29 is used for the calculation of the measured torque, as specified by Budynas and Nisbet (2015) for case hardened steel. The range of the material properties will be analysed statistically in Section 3.5.

3.2.3 Experimental Results

Two half bridge torsional strain gauge rosettes are positioned 90° to the left and to the right of the keyway as to replicate the setup used for the site measurements, as shown in Figure 3.3. These two half bridges can be used to compare the torsional strain measured on the LHS and the RHS of the keyway. It is suspected that the keyway and the method of torque transfer influences the stress distribution surrounding the keyway. Figure 3.12 shows a comparison between the strain measured on the LHS and the RHS of the keyway while the shaft experiences the same static torque.

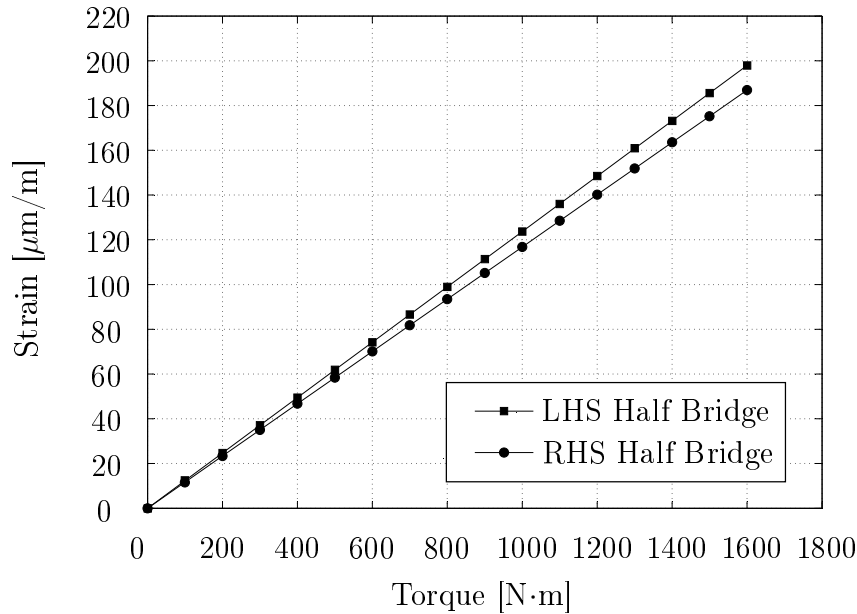


Figure 3.12: Comparison between strain measured on both the LHS and RHS of the keyway for the same shaft torsion.

It can be seen that the half bridge positioned on the LHS measures a higher strain value than the RHS half bridge while the shaft is in torsion. The linear curve that relates strain measured on the LHS of the keyway with the applied torque is expressed as,

$$S_{\text{LHS}} = 0.1237 \cdot T_{\text{applied}}, \quad (3.10)$$

while the curve representing the measured strain on the RHS is expressed as,

$$S_{\text{RHS}} = 0.1168 \cdot T_{\text{applied}}, \quad (3.11)$$

with S representing the measured strain. The strain measurements taken on both sides of the keyway while the shaft experiences torque, confirms that the LHS of the keyway deforms more than the RHS of the keyway. The strain measured on the LHS of the keyway was found to be on average 5.58 % higher than the strain measured on the RHS of the keyway. This strengthens the argument that the keyway has a significant effect on the stress distribution present on the circumference of the shaft.

A full bridge strain gauge configuration is used to measure the torsional strain on site because the V-Link-LXRS and SG-Link-LXRS used in this study are pre-set for full bridge configuration. For the full bridge configuration, the strain measured by the four strain gauges is summed and divided by four to determine the full bridge strain. The results shown in Figure 3.13 is a comparison between the applied torque and the measured torque. It is important to note that the measured torque refers to the torque that is calculated using Equation 3.9 and the measured strain.

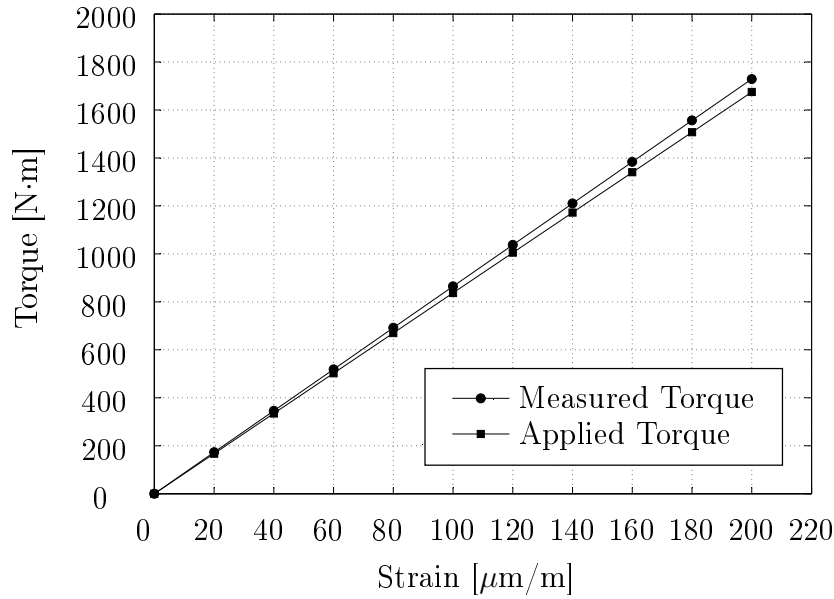


Figure 3.13: Comparison between applied torque and measured torque.

The comparison shown in Figure 3.13 indicates that the measured torque is higher than the applied torque. Also, the measured strain and the torque is related by a linear curve. This result shows that there is a need for further investigation. The curve representing the applied torque can be expressed as,

$$T_{\text{applied}} = 8.469 \cdot S_{\text{measured}}, \quad (3.12)$$

while the curve representing the measured torque can be expressed as,

$$T_{\text{measured}} = 8.645 \cdot S_{\text{measured}}, \quad (3.13)$$

with S representing measured strain which remains constant for both cases. The measured torque is 1.848% higher than the applied torque. It is suspected that the stress distribution on the circumference of the shaft, as well as the exact value of the shaft material properties, is the reason for the error in measured torque.

3.3 Digital Image Correlation

DIC is an innovative non-contact optical technique for measuring strain and displacement. Sutton *et al.* (1983) mapped the deformation of the center line of a cantilever by using this technique. Shortly after, Sutton *et al.* (1986) improved the correlation subroutine by implementing the Newton-Raphson method, improving the accuracy and computation time. The test done in this study required the DIC to be used on a 3D surface. Sutton *et al.* (2008) confirmed that the use of a two-camera stereo vision system, allows the measurement of out-of-plane motion.

DIC compares images at different stages of deformation by tracking blocks of pixels, mapped to a unique speckled pattern. For DIC to work effectively, it is required that the surface being photographed is covered with a unique speckled pattern (McCormick and Lord, 2010). This study required the use of two separate speckled pattern blocks to analyse both sides of the keyway. The speckled pattern used for the RHS of the keyway is shown in Figure 3.14. The camera setup used for the DIC measurements is shown in Figure 3.15.



Figure 3.14: Speckled pattern used to track deformation on the RHS of the keyway. The position that is chosen as the zero-reference point is also shown (Zero Point)

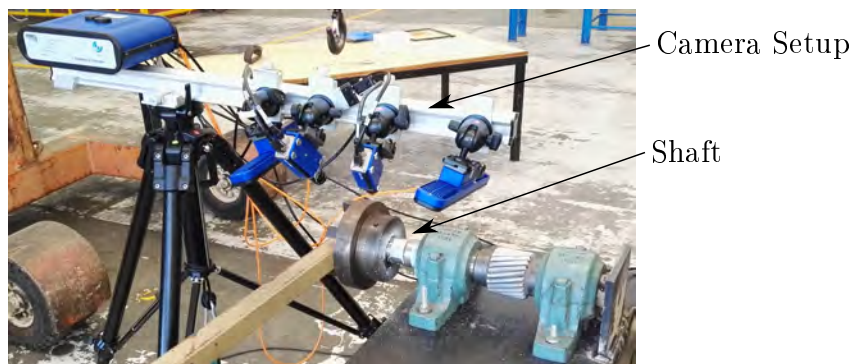


Figure 3.15: Two-camera stereo vision DIC camera setup.

3.3.1 Experimental Procedure

Once the cameras have been set up correctly and calibrated, StrainMaster is used to control the cameras and handle the image processing. Torque is applied to the shaft in the same manner as for the strain gauge measurements performed in Section 3.2. Measurements are taken from $0 \text{ N} \cdot \text{m}$ to $1500 \text{ N} \cdot \text{m}$ torque, at intervals of $500 \text{ N} \cdot \text{m}$. Each measurement is repeated five times to

obtain an acceptable average value. The displacement vector data is exported from StrainMaster and processed manually using Matlab.

3.3.2 Experimental Results

A common point found on both speckled patterns is used as the zero-reference point to eliminate any correlation error between the LHS and RHS measurements. The tangential displacement is measured relative to the zero-reference point which is located at the bottom point of the keyway, as shown in Figure 3.14. Figure 3.16 shows the relative tangential displacement of the pixels associated with each speckled pattern.

The tangential displacement is measured on the circumferential line that the strain gauges would be positioned on, as shown in Figure 3.3. Figure 3.16 indicates that the pixels on the LHS of the keyway displace 12% more than the pixels on the RHS of the keyway. This result makes sense as the key, which induces the torque on the shaft by means of the keyway wall, applies the force in the left-hand direction of the keyway and forces the region on the LHS to displace more than the region on the RHS.

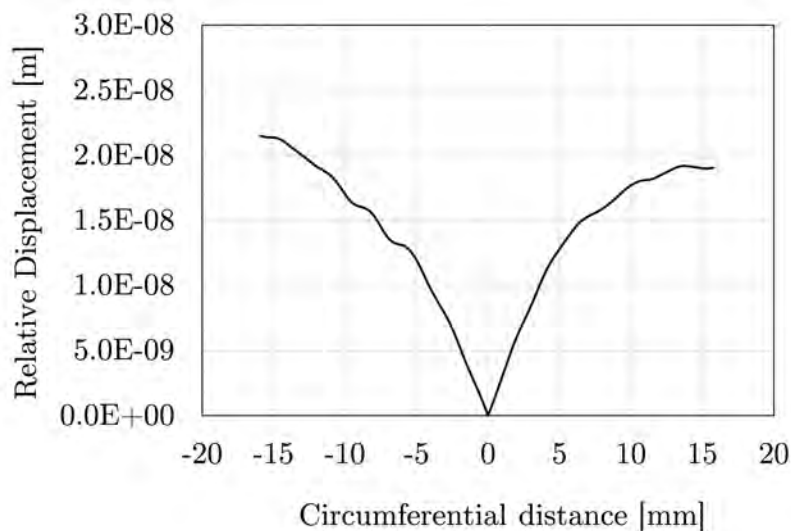


Figure 3.16: Tangential displacement of nodes on the LHS (-20 mm to 0 mm) and RHS (0 mm to 20 mm) of the keyway.

Figures 3.17 and 3.18 show the strain values measured by a fictional strain gauge in StrainMaster when the shaft experiences $1500 \text{ N} \cdot \text{m}$ torque. The fictional strain gauges are 25 mm to the left and to the right of the keyway. The strain is lower than the $173.36 \mu\text{m}/\text{m}$ strain calculated with Equation 3.9. Strain measurements from DIC show qualitatively that the LHS of the keyway experiences higher strain than the RHS of the keyway; $149.05 \mu\text{m}/\text{m}$ on the LHS and $-147.5 \mu\text{m}/\text{m}$ on the RHS. The sign difference is caused by the

strain gauge orientation. The DIC experiment correlates qualitatively with the measured strain results from Section 3.2, where it was found that the LHS of the keyway experiences more strain than the RHS.

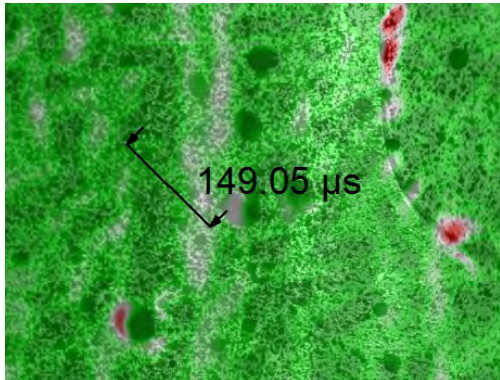


Figure 3.17: Strain measured 25 mm to the left of the keyway.

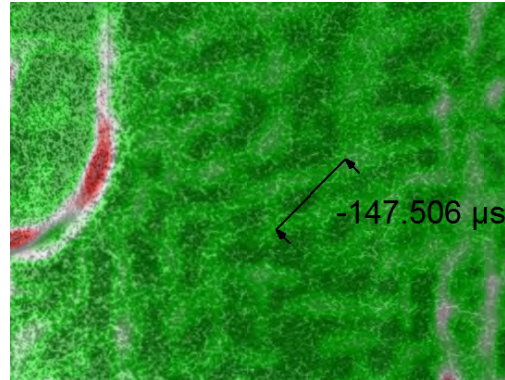


Figure 3.18: Strain measured 25 mm to the right of the keyway.

3.4 Finite Element Modelling

The primary objective of modelling the input shaft using Finite Element Method (FEM) is to identify what effect the stress distribution around the keyway will have on the strain gauge measurements. Three separate cases are modelled by FEM. The first case is the control case, where the input shaft is modelled without considering the effect of the coupling or the key. In the control case, the torque is applied at one end of the shaft while the other end is fully constrained. The effects that the coupling and the key have on stress distribution are investigated in the second and third cases. The coupling is mounted to the input shaft with a transition fit. As a safety measure, the transition fit is designed to be able to transfer all the torque if the key fails. The effect that the transition fit has on the stress distribution around the keyway will be investigated. In practise the key should act as the primary mode of torque transfer. The key exerts pressure on one of the keyway walls. Thus, uneven stress distribution around the keyway is expected and will also be investigated.

The boundary conditions of the second and third cases are discussed in Section 3.4.2 and Section 3.4.3. Quadratic tetrahedral (Tet10) elements are chosen above linear quadratic (Tet4) elements for the solid mesh of all three cases. The Tet4 element was established to be overly stiff for bending cases (Cook *et al.*, 2002). The material properties specified for compilation purposes is an elastic modulus of 207 GPa and a Poisson's ration of 0.29, given by Budynas and Nisbet (2015) for steel. The stress values obtained from the model are independent of the material properties, as load control is used for all three

cases. If displacement control was used, the stress would be dependent on the displacement of the shaft which is a function of the material properties. This was tested by varying the material properties for the same model and observing no change in the probed stress values and it is shown in Appendix D.1.

3.4.1 Mesh Independence Study

Mesh independence is performed on the shaft model that is used in all the cases that are investigated. The mesh independence was performed by observing the shear stress experienced by a node that is positioned on the LHS of the keyway. The node represents the ideal strain gauge positioning on the LHS side of the keyway. Figure 3.19 illustrates how the shear stress at the node of interest converges as the number of elements increases.

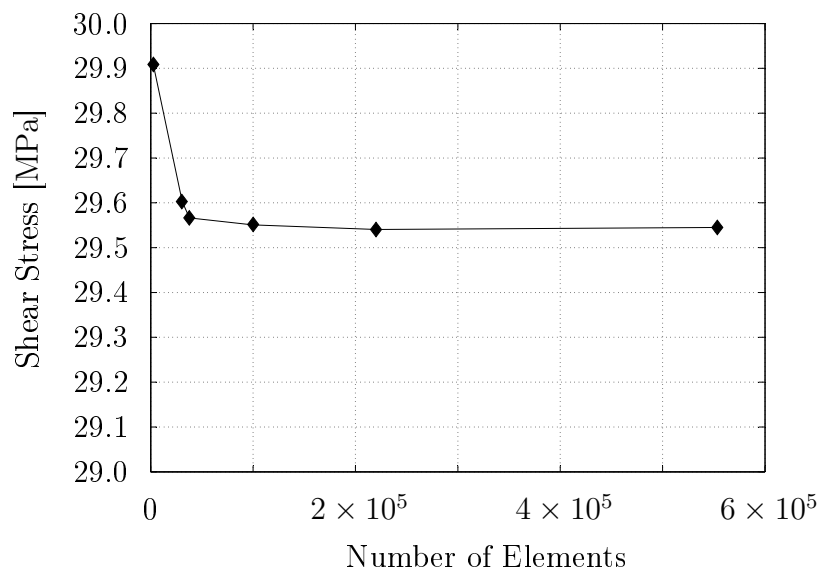


Figure 3.19: Mesh independence.

It is decided to use a mesh size of 3mm per element, which results in 220 171 elements. The mesh size is chosen to ensure that nodes are present on the shaft at 3mm increments.

3.4.2 Torque Transfer by Coupling

The coupling case is similar to the control case, with the exception that coupling shrink is included. The torque is applied by means of a torsional moment at the coupling end of the input shaft, while the other end of the shaft is constrained. The interference fit of the coupling can be modelled geometrically or by contact pressure (MSC.Software, 2016). Xiao *et al.* (2015) made use of both methods in a contact stress analysis. Modelling the coupling with contact pressure, induces bending onto the shaft, as the keyway causes an imbalance

in the pressure distribution. A geometrical constraint is used for this model to avoid bending effects. The coupling case assumes no torque transfer via the key, meaning that the shaft will experience zero bending. Figure 3.20 shows the constraint used for the coupling case.

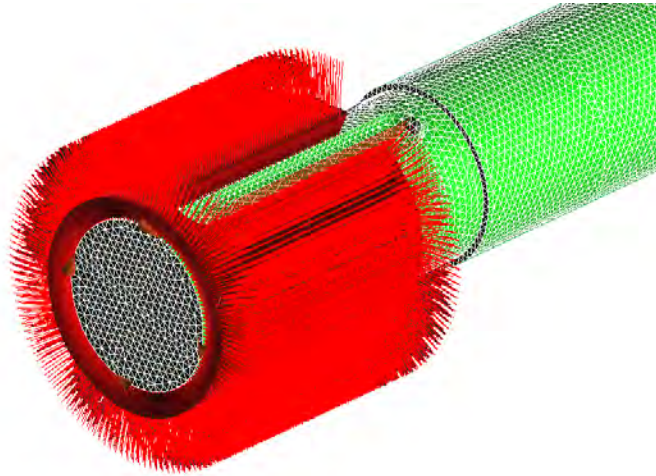


Figure 3.20: Geometric constraint applied to the input shaft, modelling the interference fit of the coupling.

The interference fit of the coupling is modelled by constraining the outer nodes on the shaft to a fixed radius. The nodes are constrained to a radius of $4.3 \mu\text{m}$ less than the original shaft radius. The shaft-coupling mating surface radius is calculated using Equations 3.14 to 3.19. Figure 3.21 shows an approximated two dimensional section of the shaft-coupling assembly.

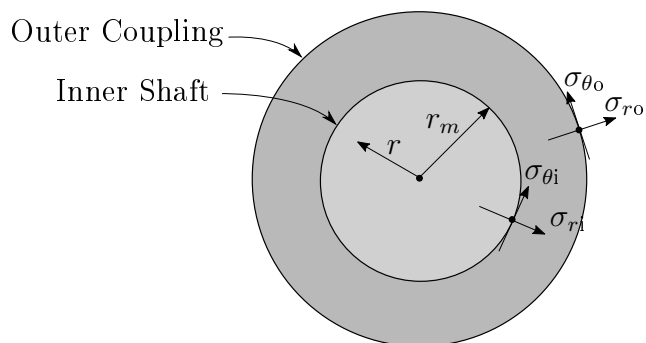


Figure 3.21: Diagram of symbols used for interference fit assembly.

$$\sigma_{\theta i} = A + \frac{B}{r^2}, \quad (3.14)$$

$$\sigma_{r i} = A - \frac{B}{r^2}, \quad (3.15)$$

$$\epsilon_{\theta i} = \frac{\sigma_{\theta i}}{E_{is}} - \frac{\nu_{is}}{E_{is}} \sigma_{r i} \quad (3.16)$$

for the inner shaft, and

$$\sigma_{\theta o} = C + \frac{D}{r^2}, \quad (3.17)$$

$$\sigma_{r o} = C - \frac{D}{r^2}, \quad (3.18)$$

$$\epsilon_{\theta o} = \frac{\sigma_{\theta o}}{E_{oc}} - \frac{\nu_{oc}}{E_{oc}} \sigma_{r o} \quad (3.19)$$

for the outer coupling. Where

σ_{θ} is the circumferential stress (hoop stress) [Pa],

σ_r is the radial stress [Pa],

A, B, C and D are constants that are obtained from the specific problem boundary conditions,

ϵ_{θ} is the circumferential strain, and

E and ν are elastic modulus and Poisson's ratio for either the shaft or the coupling.

Benham *et al.* (1996), describe Equations 3.14 to 3.19 in Chapter 14 of Mechanics of Engineering Material. The equations are applied to a shrink-fit assembly problem. Dimensions for the shaft and coupling are known, while interference pressure is unknown. The first step in using Equations 3.14 to 3.19 is to solve the constants A, B, C and D . When the inner component of the assembly is a solid shaft, constant B can be taken as zero. Equations 3.14 and 3.15 then show that $\sigma_{\theta i} = A = \sigma_{r i}$. Constants C and D can be solved by investigating the boundary condition $\sigma_{r o} = \sigma_{r i}$ at r_{ms} (mating surface radius), and $\sigma_{r o} = 0$ at the outer radius of the coupling. The problem then requires the use of an iterative approach in solving the radial shrink of the inner shaft. It should be noted that the keyway is ignored in using Equations 3.14 to 3.19.

3.4.3 Torque Transfer by Key

The case where the key transfers all the torque, proved to be difficult to model. The challenge in modelling this boundary condition is to accurately model the stress distribution on either side of the keyway without allowing the shaft to bend unrealistically from the non-tangential force exerted by the key, as shown in Figure 3.22. The shaft is forced to rotate with the coupling in practice and unrealistic modelled bending refers to bending that allows the shaft to move outside the bounds of the coupling.

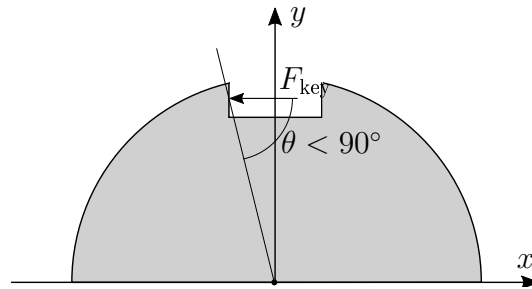


Figure 3.22: Force exerted by key onto keyway wall.

The torque is applied at the gear end of the shaft. The coupling end of the shaft that is fully constrained, prevented the nodes from leaving the bounds of the coupling and limited shaft bending. The key is modelled by applying a tangential constraint to the nodes on one wall of the keyway. The model is shown in Figure 3.23.

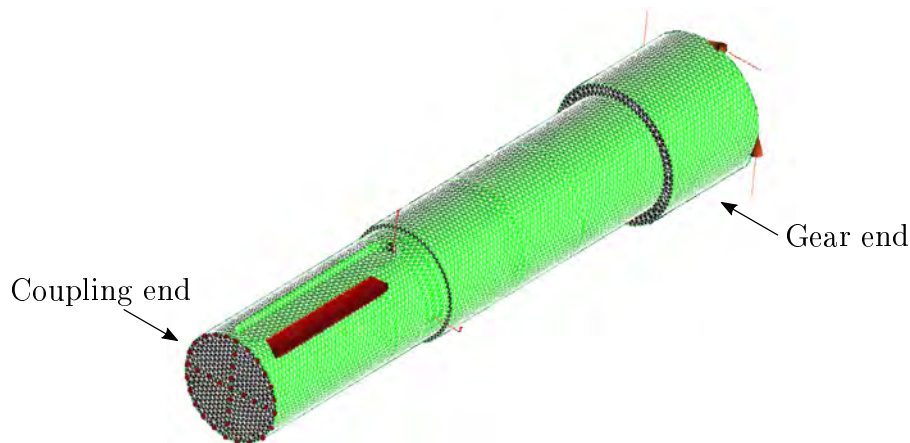


Figure 3.23: Torsion applied between the keyway and the gear teeth, modelling zero interference from the coupling and torque transfer by means of the key.

3.4.4 Modelled Stress Distribution

A section of the input shaft is shown in Figure 3.24, where the effect that the keyway has on the stress distribution can be observed. The case where all the torsion is applied by the coupling, and the case where all the torsion is applied by the key, are shown separately. The shear stress is lower in the region of the keyway for both cases. The stress distribution is more symmetrical around the keyway in the case of the coupling. The key causes higher shear stress on the side of the keyway that is under load.

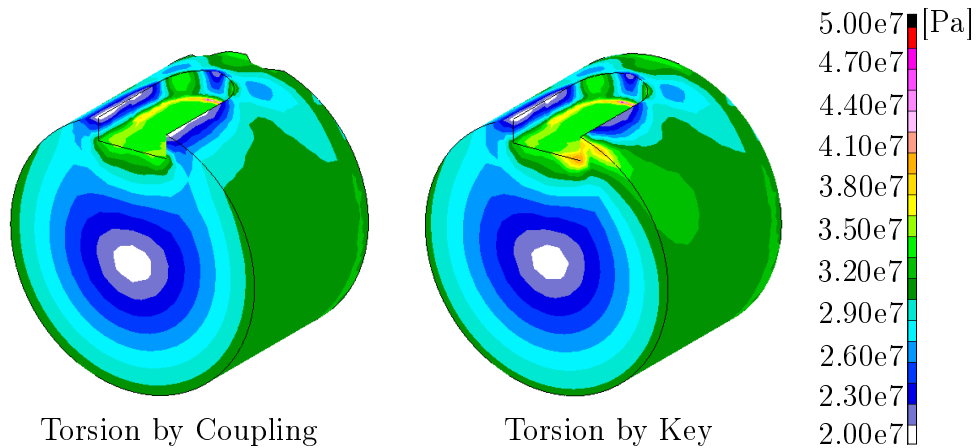


Figure 3.24: Fringe plot of maximum shear stress experienced by the modelled shaft.

3.4.5 Modelled Strain Measurement

The FEM models can be used to predict the strain measured by means of strain gauges on a physical input shaft. A stress tensor is used to identify the x and y stress components (σ_x and σ_y), as well as the shear stress (τ_{xy}) at the nodes of interest. The nodes of interest are positioned on the LHS and the RHS of the keyway, as shown in Figure 3.25, and represent the possible position of the strain gauges (SG). Each node represents one half bridge torsional strain gauge rosette. The probed stress has to be transformed to the planes on which the strain gauges are measuring strain.

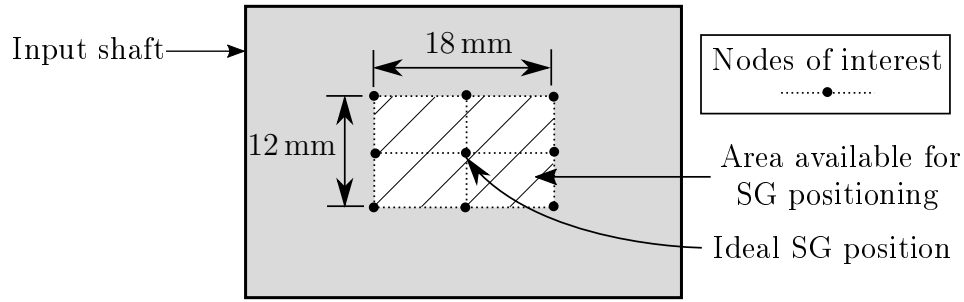


Figure 3.25: Nodes on FEM models that represent the possible strain gauge position.

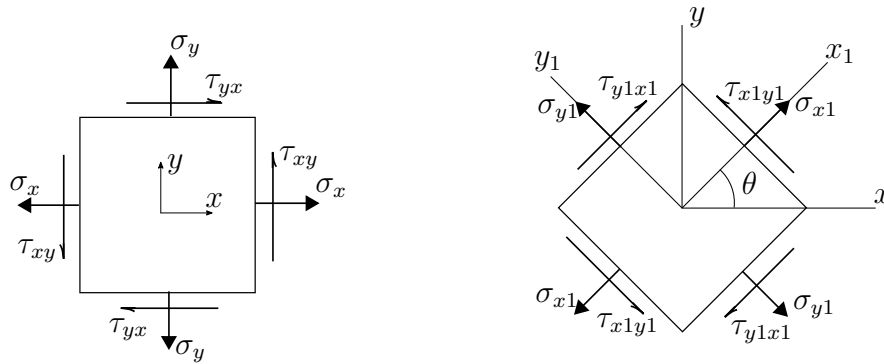


Figure 3.26: Illustration of stress transformation on to the plane of strain measurement.

The stress transformation equations from Benham *et al.* (1996), can be expressed as,

$$\sigma_{x1} = \frac{\sigma_x + \sigma_y}{2} + \frac{\sigma_x - \sigma_y}{2} \cos 2\theta + \tau_{xy} \sin 2\theta, \quad (3.20)$$

and

$$\sigma_{y1} = \frac{\sigma_x + \sigma_y}{2} - \frac{\sigma_x - \sigma_y}{2} \cos 2\theta - \tau_{xy} \sin 2\theta. \quad (3.21)$$

Using Equations 3.20 and 3.21 allows the transformation of σ_x , σ_y and τ_{xy} on to any required plane, as illustrated in Figure 3.26. Transforming the probed stress values on to a 45° plane, allows for the theoretical stress (σ_{x1} and σ_{y1}) to be identified on the principal stress planes that the strain gauges are positioned on. Using the stress-strain relationship equations for plane stress from Benham *et al.* (1996), it is possible to calculate the strain on those planes as,

$$\epsilon_{x1} = \frac{\sigma_{x1} - \nu\sigma_{y1}}{E}, \quad (3.22)$$

and

$$\epsilon_{y2} = \frac{\sigma_{y1} - \nu\sigma_{x1}}{E}. \quad (3.23)$$

The strain value that is derived from the FEM model is the value that would theoretically be measured by a torsional strain gauge rosette placed on the node. Two strains are calculated for each node, as the strain gauge rosette consists of two perpendicular strain gauges. Probing a node on the LHS and the RHS of the keyway, enables the calculation of the measured strain that would be measured by a full bridge torsional strain gauge configuration.

The strain gauge theory for a full bridge configuration assumes that the four strain gauges of the full bridge are measuring strain that is equal in magnitude, but differ in sign, depending on the relative alignment of the strain gauges. The four strain gauges of a full bridge configuration are positioned in such a way that $\epsilon_1 = -\epsilon_2 = \epsilon_3 = -\epsilon_4$. The relationship between the electrical measurement of the Wheatstone bridge and mechanical strain can be expressed as

$$\frac{V_{\text{out}}}{V_{\text{in}}} = \frac{k}{4}(\epsilon_1 - \epsilon_2 + \epsilon_3 - \epsilon_4), \quad (3.24)$$

where

V_{out} - Output voltage of the Wheatstone bridge [V]

V_{in} - Input voltage of the Wheatstone bridge [V]

k - Gauge factor

ϵ_{1-4} - Strain measured by each resistor of the full bridge [$\mu\text{m}/\text{m}$].

Assuming $\epsilon_1 = -\epsilon_2 = \epsilon_3 = -\epsilon_4 = \epsilon$, Equation 3.24 reduces to

$$\frac{V_{\text{out}}}{V_{\text{in}}} = k\epsilon, \quad (3.25)$$

with

$$\epsilon = \frac{\epsilon_1 - \epsilon_2 + \epsilon_3 - \epsilon_4}{4}. \quad (3.26)$$

The possible mode of torque transfer that the input shaft will be subjected to in practice is modelled by the two cases that investigate the coupling and key separately. The precise mode of torque transfer on to the input shaft is unknown and lies within these two cases. The strain that would be measured on the cases modelled, will be compared to strain measured on a physical

input shaft, as discussed in Chapter 3.2.3. The difference between the strain measured on both sides of the keyway is compared, as well as the total full bridge strain. Importantly, the strain that is considered is for ideal strain gauge positioning. The results of the strain comparison is shown in Table 3.1.

Table 3.1: LHS half bridge, RHS half bridge, difference between LHS and RHS measurements, and full bridge strain.

Case Investigated	Half Bridge LHS [$\mu\text{m}/\text{m}$]	Half Bridge RHS [$\mu\text{m}/\text{m}$]	Difference [%]	Full Bridge [$\mu\text{m}/\text{m}$]
Control	175.29	175.89	0.346	175.59
Coupling	172.84	180.04	4.170	176.44
Key	183.96	173.07	5.919	178.52
Measured	185.55	175.20	5.558	180.20

For the control case there is no coupling and no key present. The only factor that could influence the strain measured, is the keyway. The modelled strain measurements, measured on the LHS and RHS of the keyway, differ by 0.346%. The reason for the difference in strain is that the stress distribution is not exactly symmetric around the keyway.

The result of the coupling case show that the area on the RHS of the keyway experiences 4.17% more torsional strain than the area on the LHS of the keyway. A possible reason is that the RHS of the keyway is free to deform more than the LHS of the keyway. The torque is applied in the direction of the LHS, meaning that the gap of the keyway reduces the resistance to surface displacement experienced by the area on the RHS of the keyway.

The result for the case where the key transfers all the torque, shows that the LHS of the keyway experiences 5.919% more torsional strain than the RHS. This is the result of the force that is applied by the key to the left hand wall of the keyway. The key case also correlates well with the physically measured torsional strains. The strain measured on both sides of the keyway, as well as the full bridge strain, is within 1% of the modelled case. The difference between the LHS and RHS torsional strain is slightly higher for the modelled case. This is because the key case completely ignores the interference fit of the coupling, where as in practise the interference fit of the coupling has a slight influences on the stress distribution around the keyway.

The modelled cases proved that a linear relationship exists between torque applied to the shaft and measured torsional strain, as shown in Appendix D.2. In comparing the modelled cases to the physical strain gauge measurements, it was concluded that the key case acts as the best FE model of the M4ACC

gearbox input shaft. The effect of the coupling transition fit is overshadowed by the force applied by the key.

3.5 Statistical Analysis

The Monte Carlo simulation is a technique that is widely used in the probabilistic analysis of engineering problems. Mahadevan (1997) describes the Monte Carlo simulation as "a numerical experimentation technique to obtain the statistics of the output variables of a system computational model, given the statistics of the input variables".

In Probability, Reliability and Statistical Methods in Engineering Design, Haldar and Mahadevan (2000) divide the Monte Carlo simulation into six primary steps: (1) describe the problem in terms of the random variables in question; (2) quantifying the probabilistic characterization of the probability density functions (PDFs) and the probability mass functions (PMFs) of the random variables and their corresponding parameters; (3) generation of all the random variables; (4) numerical experimentation, i.e. evaluate the problem deterministically for each set of realizations of the random variables; (5) document the probabilistic information from a given number of such realizations; and (6) identifying the accuracy of the simulation.

The statistical analysis is performed on the FE model of the case where the key transfers the torsion on to the input shaft. Stress is extracted from the model, based on the strain gauge position and related to strain based on the material property range.

3.5.1 Define Problem and Random Variables

Steps 1 and 2 of the Monte Carlo process are discussed in this section. Measuring strain by means of strain gauges on the input shaft of the M4ACC gearbox makes use of fundamental equations of strength of materials. Assumptions are made regarding the shaft geometry, the positioning of the strain gauges and the material properties of the shaft. The shaft is approximated as a homogeneous circular cross section shaft (ideal shaft) in the derivation of Equation 3.9. It is also assumed that the strain gauges are positioned in the ideal position, and that the elastic modulus and Poisson's ratio of the shaft material is equal to 207 GPa and 0.29 respectively.

The geometry assumptions are incorporated by the FE model and they do not require statistical analysis. The average position of the strain gauges can be taken as the ideal position thereof, with the positioning range limited to the area available for the strain gauges, as shown in Figure 3.25. The area available is based on the physical circumstances that were presented to the researcher on site, and is shown in Figure 3.4. A normal distribution is chosen

for the random positions of the strain gauges, as it is more likely that the strain gauges will be positioned in the average position, than anywhere else.

The supplier of the input shaft performed a statistical analysis on 80 samples of the shaft and found that the mean value of the modulus of elasticity is equal to 207.97 GPa with a minimum value of 201.2 GPa and a maximum of 215.7 GPa. The Poisson's ratio varied from 0.27 to 0.30, (Verbeek, 2016). The range of the elastic modulus and Poisson's ratio is best represented by a normal distribution as stated by Ayyub (1998). Steps 3-6 are completed in Matlab R2013b, and the results are discussed in Section 3.5.2 and Section 3.5.3.

3.5.2 Effect of Strain Gauge Misalignment

This section aims to identify how the stress experienced by a strain gauge is affected by the positioning thereof. Three strain gauge misalignments, caused by human error, are investigated. The three misalignments are circumferential misalignment ($-\theta_{err}$ to $+\theta_{err}$), axial misalignment ($-z_{err}$ to $+z_{err}$) and rosette angle misalignment ($-\alpha_{err}$ to $+\alpha_{err}$). A normal distribution is assumed for the range of possible SG positions in each direction. The circumferential and axial misalignment is shown in Figure 3.27. Angular misalignment is shown in Figure 3.28, and refers to the angle at which the rosettes are positioned on the LHS and RHS.

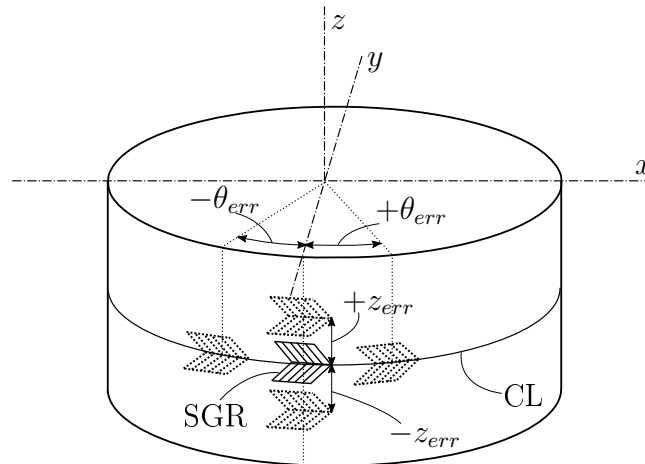


Figure 3.27: Strain gauge rosette (SGR) misalignment in the axial direction ($\pm z_{err}$) and in the tangential ($\pm \theta_{err}$) direction on the circumferential line (CL).

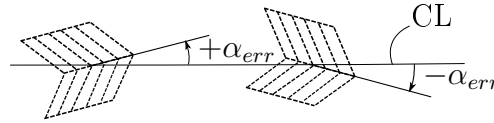


Figure 3.28: Angular strain gauge misalignment measured from the circumferential line (CL).

The area available for the strain gauges allows for a maximum axial strain gauge misalignment of $+z_{err} = 6$ mm in the positive z -direction, and $-z_{err} = 6$ mm in the negative z -direction. The tangential misalignment from the ideal position is $+\theta_{err} = 15.9^\circ$ in the right-hand direction and $-\theta_{err} = 15.9^\circ$ in the left-hand direction. The angular misalignment is selected to range from $+\alpha_{err} = 15^\circ$ to $-\alpha_{err} = 15^\circ$, measured from the circumferential line. The allowable range of angular misalignment is selected based on the assumption that the researcher was able to align the strain gauges reasonably well.

The random generator function of Matlab R2013b is used to generate 100 000 independent rosette positions on both sides of the keyway. The angular alignment of each rosette is then randomly determined. The stress experienced by each rosette can be calculated using Equation 3.20 and Equation 3.21. The stress experienced by each rosette is compared to the stress that a rosette would experience if it were positioned on an ideal shaft. The effect of the shaft geometry and the position of the rosette is shown in this result.

Table 3.2 shows that the geometry of the shaft and the rosette position have a significant effect on the stress experienced by the rosettes. The two rosettes consist of four strain gauges and the stress experienced by each strain gauge is shown as σ_{1-4} . Table 3.2 also shows the mean difference in stress from the ideal stress, and one standard deviation of the mean difference.

Table 3.2: Mean variation of the modelled stress compared to the ideal stress.

	Ideal Stress [MPa]	Mean Modelled Stress [MPa]	Mean Difference [%]	Standard Deviation [%]
σ_1	27.817	33.636	20.92	2.832
σ_2	-27.817	-21.733	-21.87	1.837
σ_3	27.817	24.503	-11.91	1.973
σ_4	-27.817	-34.447	23.83	1.569

3.5.3 Effect of Material Properties

The result shown in this section builds on the results from Section 3.5.2 by taking the varying material properties into account before calculating the measured strain. The theoretical stress experienced by the four strain gauges for each of the 100 000 iterations is converted into a measured strain value using Equation 3.22 and Equation 3.23. The elastic modulus and Poisson's ratio values used in Equation 3.22 and 3.23 are obtained from a random generation of normally distributed values of each of the variables, as discussed in Section 3.5.1. The modelled strain is compared to the strain that is expected to be measured on an ideal shaft. The modelled strain incorporates the effect of shaft geometry, rosette position and shaft material properties.

The distribution of the modelled strain is shown in Figure 3.29 for each strain gauge. Table 3.3 shows the statistics of the modelled strain distribution for each strain gauge, calculated with Matlab R2013b. For a normal distribution, the skewness is 0, the kurtosis is 3 and the median is equal to the mean (NIST/SEMATECH, 2013) and (Bentler, 2006). Kim (2013) states that normal distribution may not be assumed once a kurtosis greater than 7 is reached. The modelled strain for each strain gauge can thus be assumed to have a normal distribution.

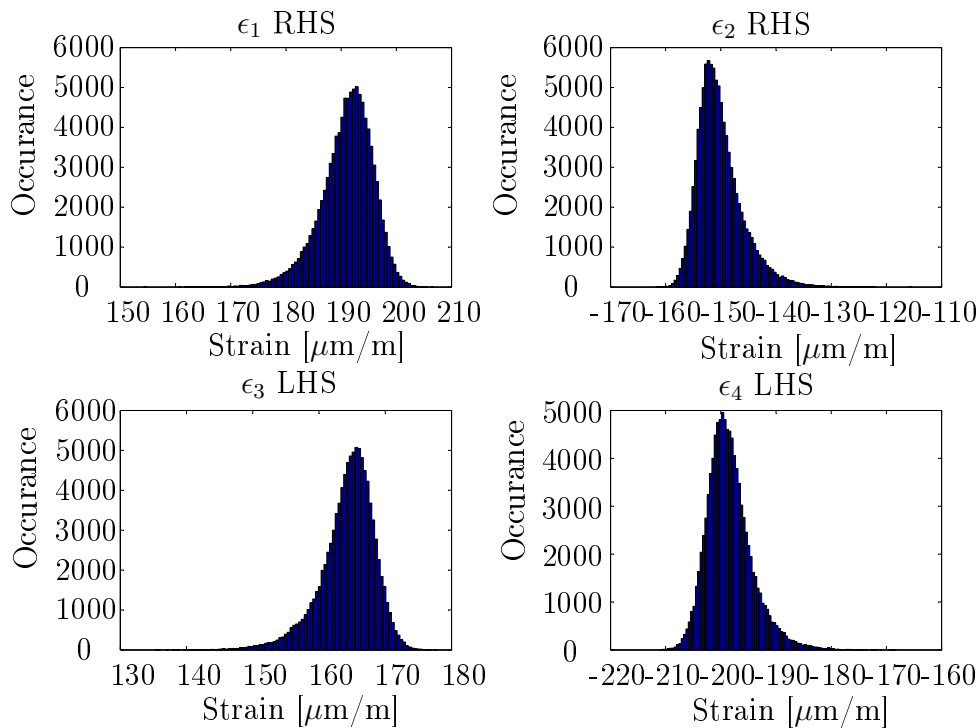


Figure 3.29: Statistical distribution of the modelled strain for each strain gauge of the full bridge configuration.

Table 3.3: Statistical characteristics of the modelled strain distribution.

	Skewness	Kurtosis	Median [$\mu\text{m}/\text{m}$]	Mean [$\mu\text{m}/\text{m}$]
ϵ_1	-0.1277	3.1204	191.686	191.568
ϵ_2	0.3455	3.4906	-150.836	-150.639
ϵ_3	-0.1602	3.4669	165.195	165.100
ϵ_4	0.1167	3.3342	-199.370	-199.294

The mean value measured by each strain gauge, and the full bridge measured strain is shown in Table 3.4. The four strain gauges measure significantly different strain values, but the combined strain value correlates reasonably well with the strain that would be measured on an ideal shaft.

Table 3.4: Comparison between strain experienced by a full bridge configuration positioned on an ideal shaft and the modelled shaft, as well as the standard deviation of the modelled shaft strain.

		Ideal Shaft Strain [$\mu\text{m}/\text{m}$]	Mean Statistical Strain [$\mu\text{m}/\text{m}$]	Standard Deviation [$\mu\text{m}/\text{m}$]
RHS	ϵ_1	173.35	191.562	5.154
	ϵ_2	-173.35	-150.625	3.944
LHS	ϵ_3	173.35	165.083	4.354
	ϵ_4	-173.35	-199.289	4.441
	ϵ_{total}	173.35	176.639	3.808

Figure 3.30 represents the distribution of 100 000 full bridge strain measurements on the input shaft while the shaft experiences a torsion of $1500 \text{ N} \cdot \text{m}$. The statistical analysis shows that the strain measured by a full bridge on the input shaft, can be expected to be on average 1.815 % higher than the strain that would be measured by the same full bridge on an ideal shaft. The standard deviation of the measured strain is $3.801 \mu\text{m}/\text{m}$.

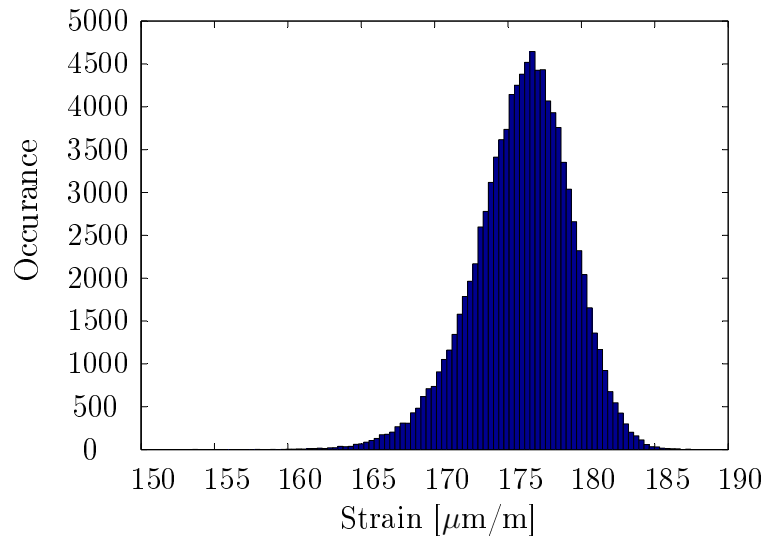


Figure 3.30: Distribution of the modelled full bridge strain measurement over 100 000 iterations.

3.6 Relationship Between Shaft Elasticity and Temperature

Accurate strain measurements require that the material properties of the structure being tested are exactly known. In Chapter 3.2 it is stated that the elastic modulus value and the Poisson's ratio of the shaft material can vary over a known range. According to Chen *et al.* (2006) the elastic modulus of mild steel can reduce by 5% when the operational temperature increases from 22 °C to 120 °C. The input shaft being analysed in this project is made of case hardened steel 1.6587(18CrNiMo7-6), according to BS EN 10084:2008. The objective of this section is to identify the change in elastic modulus of the input shaft during increased shaft temperature.

3.6.1 Background

According to Lord and Morrell (2007) it is possible to obtain reliable elastic modulus data from tensile tests, but this normally requires a separate experimental setup, using high accuracy averaging strain measurements and data analysis procedures. Lord and Morrell (2007) also state that dynamic methods of measuring elastic modulus are generally more versatile and can be readily applied to high temperature measurements. Dynamic methods include the flexural resonance method, the impact excitation technique, and other ultrasonic, resonance or acoustic wave propagation methods. Advantages of dynamic methods are that they are quick, simple and non-destructive. Acoustic emissions (AE) frequency analysis can be used to physically measure the natural frequencies of the input shaft. The technique uses a FFT to calculate the

frequency spectrum of the AE signal (de Groot *et al.*, 1995) and (Surgeon and Wevers, 1999).

A standard for testing the dynamic elastic modulus by impulse excitation of vibration is described in ASTM E1876-01. This standard states that the dynamic elastic properties of a material can be determined exactly if the geometry, mass and mechanical resonant frequencies of a suitable test specimen can be measured. In this experiment the goal is to identify the change in elastic modulus, and not the absolute elastic modulus and Poisson's ratio of the shaft material. As such it is not required to follow the entire test and analysis procedure described by ASTM E1876-01.

3.6.2 Theoretical Calculations

Meirovitch (2001) states that the transverse natural frequencies of a uniform Euler-Bernoulli beam can be calculated as

$$f_i = \frac{\beta_i}{2\pi} \sqrt{\frac{EI}{\rho A}}, \quad (3.27)$$

where

β is a constant associated with the beam boundary conditions,

I is the central moment of inertia of the beam,

ρ is density of the beam material,

A is the cross sectional area of the beam,

E is the elastic modulus of the beam material.

Shaft temperature is increased in this experiment causing ρ and E to change. After substituting

$$m = \rho AL \quad (3.28)$$

and

$$I = \frac{\pi D^4}{64} \quad (3.29)$$

into Equation 3.27, Equation 3.27 can be rewritten as

$$E = \frac{256m\pi}{\beta} \cdot \frac{f^2}{D^4L}. \quad (3.30)$$

For a temperature increase of ΔT the elastic modulus changes from E to E' . The relationship between E and E' can be calculated as

$$\frac{E'}{E} = \frac{D^4 L}{(D + \Delta D)^4 (L + \Delta L)} \cdot \left(\frac{f'}{f}\right)^2. \quad (3.31)$$

Unlike Equation 3.31, ASTM E1876-01 does not consider the diametrical expansion of the shaft. The longitudinal and diametric expansion of the shaft is calculated as $\Delta L = L \cdot \Delta T \cdot c_t$ and $\Delta D = D \cdot \Delta T \cdot c_t$, with c_t being the thermal expansion coefficient. The change in the elastic modulus of the shaft can then be expressed as

$$\Delta E = 1 - \frac{1}{(1 + \Delta T \cdot c_t)^5} \cdot \left(\frac{f_{i_j}}{f_{i_0}}\right)^2, \quad (3.32)$$

where

ΔE is the change in elastic modulus at varying shaft temperatures,

f_{i_j} is the i -th natural frequency of the shaft at a given temperature, j ,

f_{i_0} is the i -th natural frequency of the shaft at room temperature.

3.6.3 Experimental Procedure

Three microphones are used to obtain an average of the AE signal, (PCB-Microphone-378B02). The shaft is heated by placing it in a composites processing oven and regulating the temperature. The shaft is then excited by dropping it onto a hard surface that is heavily damped. This technique is chosen instead of a modal hammer, as is described by ASTM E1876-01, because it allows for more energy to be transferred to the shaft. This method excites the transverse natural frequencies of the shaft and torsional frequencies will not be measured. The measurement setup is shown in Figure 3.31.



Figure 3.31: Setup used for AE measurements.

The shaft is left in the oven for two hours before each measurement, ensuring the shaft is heated through. The minimum time needed to heat the shaft

through is calculated to be roughly 100 min. The calculation is performed by making use of the Heisler charts in Chapter 4 of Cengel and Ghajar (2015) and assuming a convection heat transfer coefficient of $70 \text{ W/m}^2 \cdot \text{K}$.

The shaft boundary condition is free-free and is tested at four temperatures. The room temperature of the laboratory is 16°C , where after the oven temperature is raised to 45°C , 65°C and 100°C . The experiment is repeated over three days, leaving the shaft to cool overnight. The AE are recorded and processed with a SQuadriga II Mobile Recording and Playback System, (HEAD Recorder) and (Artemis SUITE).

3.6.4 Experimental Results

The transverse natural frequencies of the shaft are measured at room temperature and shown as a spectrogram in Figure 3.32. The spectrogram shows that the measured frequencies remain constant with time.

The frequency spectrum plot of the shaft at two temperature intervals is shown in Figure 3.33. The amplitudes of the plots vary, due to the inconsistent amount of energy being transferred to the shaft. The frequency shift of the first natural frequency is shown in Figure 3.34.

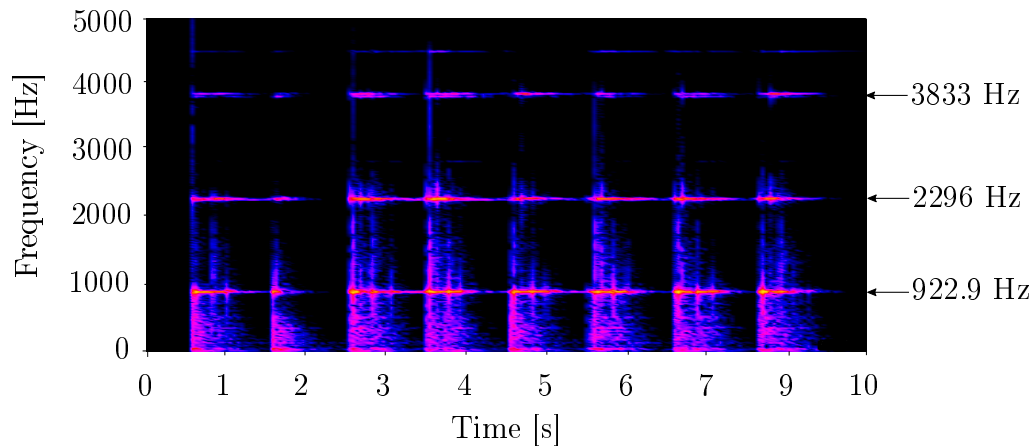


Figure 3.32: Spectrogram of shaft frequencies.

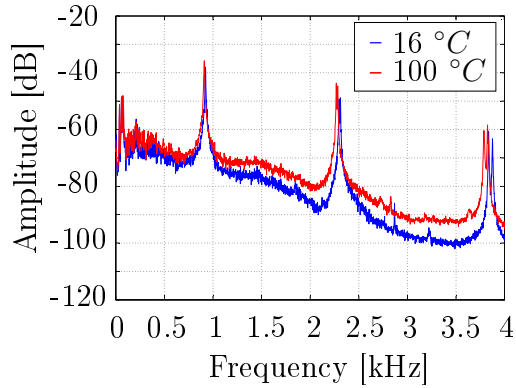


Figure 3.33: Frequency spectrum plot of shaft vibration.

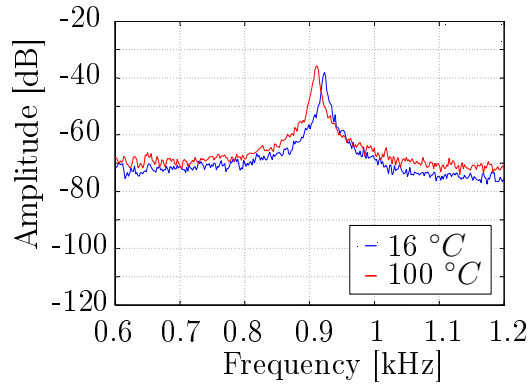


Figure 3.34: First natural frequency of input shaft.

The change in frequency of the first, second and third natural frequencies (f_{1_j}, f_{2_j} and f_{3_j}) of the shaft are shown in Figure 3.35. The frequencies f_{1_j} , f_{2_j} and f_{3_j} shift from 923 Hz to 911 Hz, 2297 Hz to 2268 Hz and 3836 Hz to 3788 Hz when the shaft temperature is increased from 16 °C to 100 °C.

The final result showing the change in the elastic modulus of the shaft is determined by first establishing a chosen room temperature value of 20 °C. A second order polynomial interpolation is performed to fit a curve to the measured data, shown in Figure 3.35. The first three transverse natural frequencies of the shaft, at room temperature, are given as $f_{1_0} = 922.9$ Hz, $f_{2_0} = 2296$ Hz and $f_{3_0} = 3833$ Hz. Equation 3.32 can be used to calculate the change in elastic modulus for each measured frequency value with regard to the natural frequencies of the shaft at room temperature.

The result of applying Equation 3.32 to the measured data is shown in Figure 3.36. The data for each temperature interval is represented by a box-and-whisker plot, with a second order polynomial curve fitted to the combined data. Each temperature interval has 108 data samples and the box-and-whisker plot represents the distribution thereof. For the data at 16 °C there were twelve outliers, but they are ignored as the rest of the samples are concentrated around the mean. Table 3.5 shows the mean change in the elastic modulus for each temperature interval, as well as the standard deviation thereof. Normality can be assumed for the data of each interval ($-1 < \text{skewness} < 1$), (Kim, 2013).

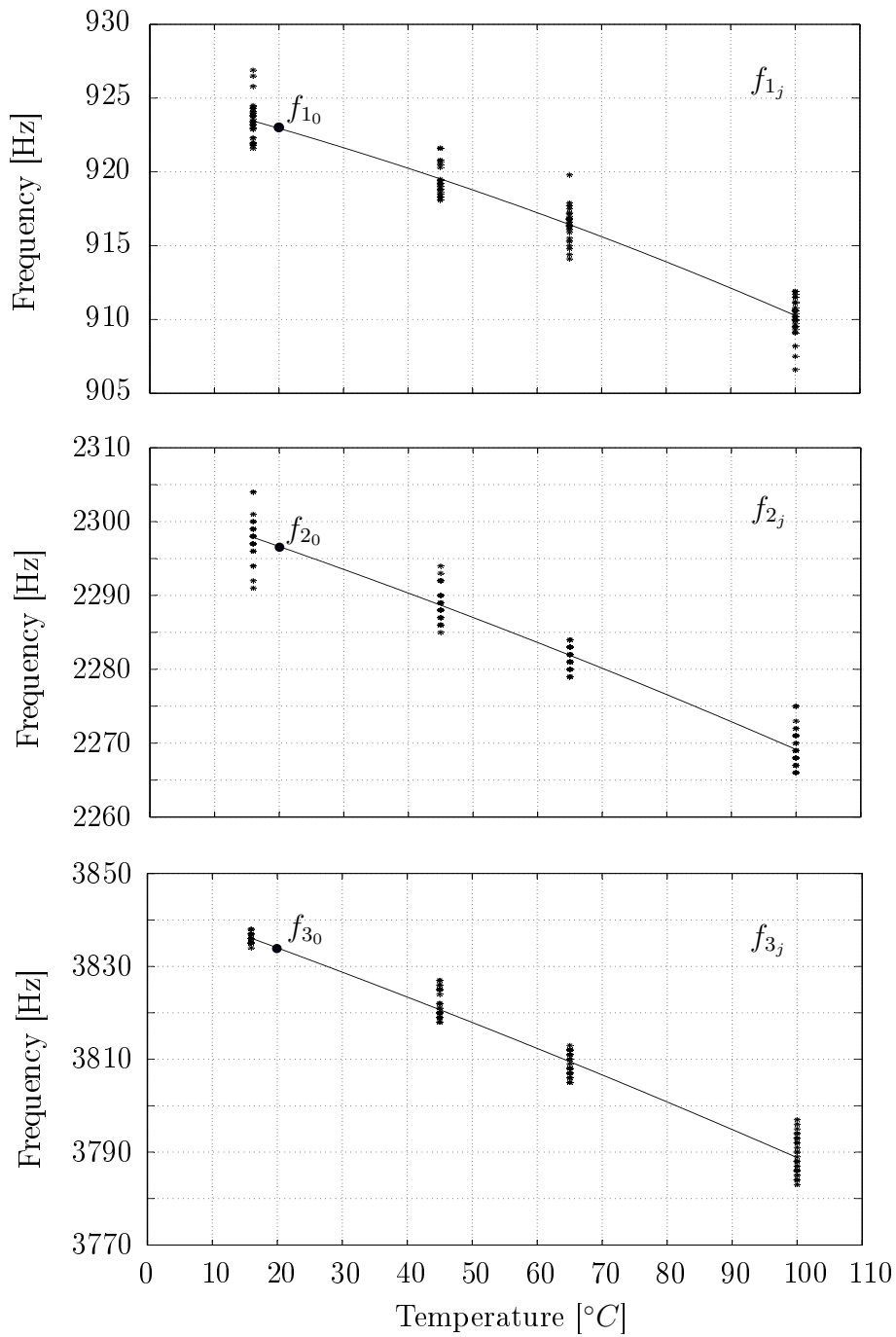


Figure 3.35: Frequency change of the first (f_{1_j}), second (f_{2_j}) and third (f_{3_j}) natural frequencies of the shaft at temperature j .

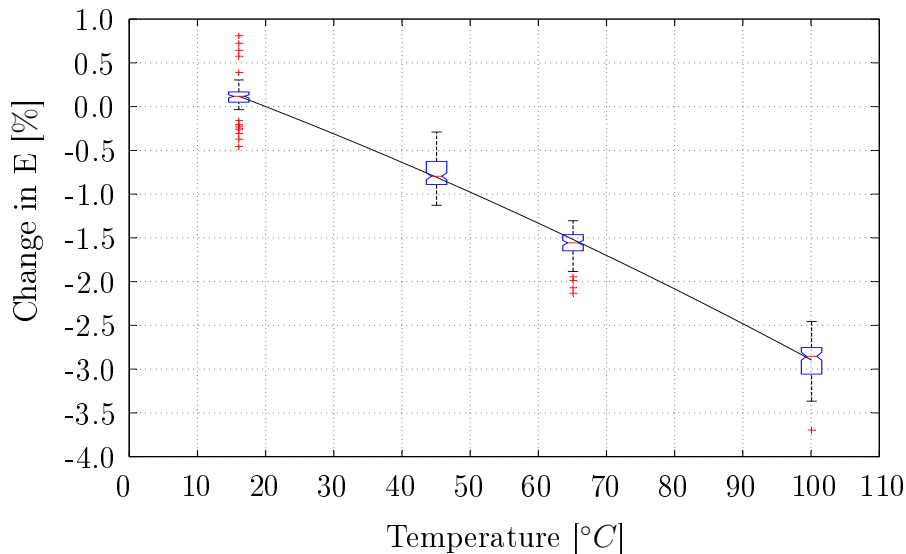


Figure 3.36: Percentage change in E vs. temperature of shaft.

Ledbetter and Austin (1984) measured the velocity of sound waves through three grades of hardened steel. They found that the elastic modulus of all three grades of steel reduced by 2.35% to 2.39% for a temperature increase from 20°C to 100°C. The results shown in Table 3.5 indicate that the elastic modulus of the input shaft reduced by 2.437% for the same temperature increase.

Table 3.5: Average change in elastic modulus of the shaft for each temperature interval.

Temperature Interval [°C]	Mean ΔE [%]	Standard Deviation [%]
16	0.157	0.201
45	-0.785	0.206
65	-1.540	0.163
100	-2.859	0.245

The measured results are compared to a FE modal analysis to validate the measured natural frequencies.

3.6.5 FE Modal Analysis

A modal analysis is performed with FE to identify the vibration induced dynamic response of the input shaft. The analysis shows the displacement that can be expected if the given natural frequencies are excited. The input shaft

is modelled as free-free. Figure 3.37 shows the shaft displacement for the first four natural frequencies of the shaft. Mode 1, 3 and 6 are the first three modes of transverse displacement and displace in the y -plane; Mode 2, 4 and 7 displace in the x -plane. Mode 5 is the first mode of torsional displacement.

The natural frequencies of the shaft are measured in Section 3.6. The natural frequencies obtained from FE simulation are compared to AE measurements taken on the input shaft in Table 3.6. The shaft is excited in the transverse direction, hence the AE measurements measure natural frequencies in the transverse direction. The AE measurements correlate well with the modal analysis performed by FE simulation.

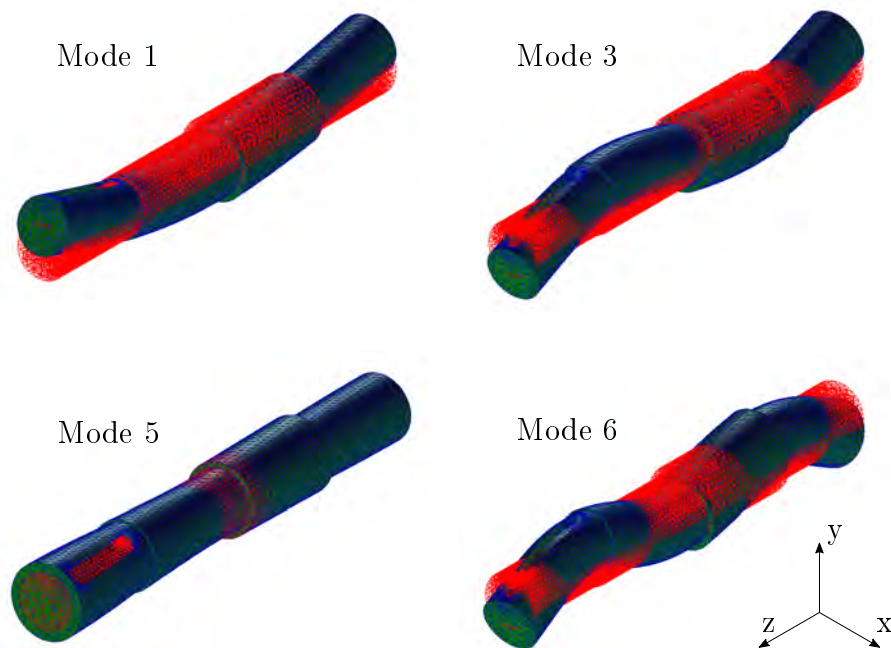


Figure 3.37: Mode shapes of the input shaft.

Table 3.6: Comparison between FE simulation and AE measurements on the input shaft.

Shaft Deformation	Natural Frequency	FE [Hz]	AE [Hz]	Difference [%]
Mode 1	f_1	883.2	922.9	4.30
Mode 3	f_2	2200.2	2296	4.18
Mode 5	f_3	2808.3		
Mode 6	f_4	3777.8	3833	1.44

3.7 Strain Measurement Accuracy

The calibration curve shown in Figure 3.38 relates measured strain to shaft torque. The calibration curve and two standard deviation error bands ($\pm 2\sigma$) are obtained from the statistically derived strain measurements from Figure 3.30. The error bands represent two standard deviations and equate to a measurement tolerance of $\pm 4.5\%$. The physical strain measurements from Section 3.2 fall within the error bounds of Figure 3.38.

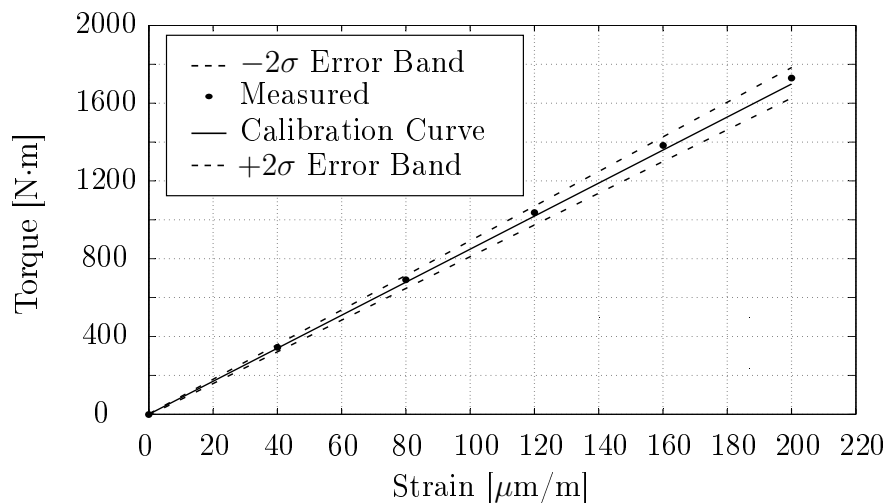


Figure 3.38: Statistical relationship between shaft torque and torsional strain.

The material properties used in the derivation of the calibration curve were specified for room temperature (20°C). The torque obtained from Figure 3.38 needs to be corrected for a given shaft temperature. The correction factor is given in Figure 3.39 and can be used for an operational temperature range of 20°C to 100°C . The correction factor is calculated using the mean ΔE values specified in Table 3.5.

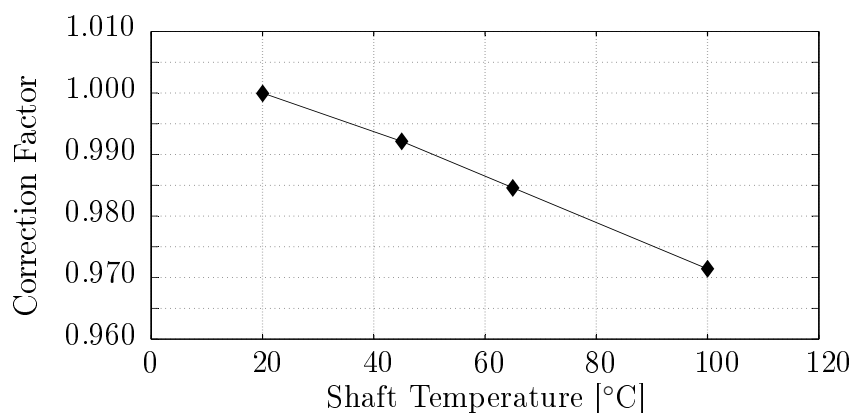


Figure 3.39: Correction factor for increased operational shaft temperature.

Chapter 4

Measurements

The objectives of this research project require the analysis of reliable data acquired from on-site measurements. The gearbox that is tested is located in Unit 3 (position 33MAG50) of Matimba Power Station and depicted in Figure 4.1. Measurements were taken on ten days between 15–26 April 2016.

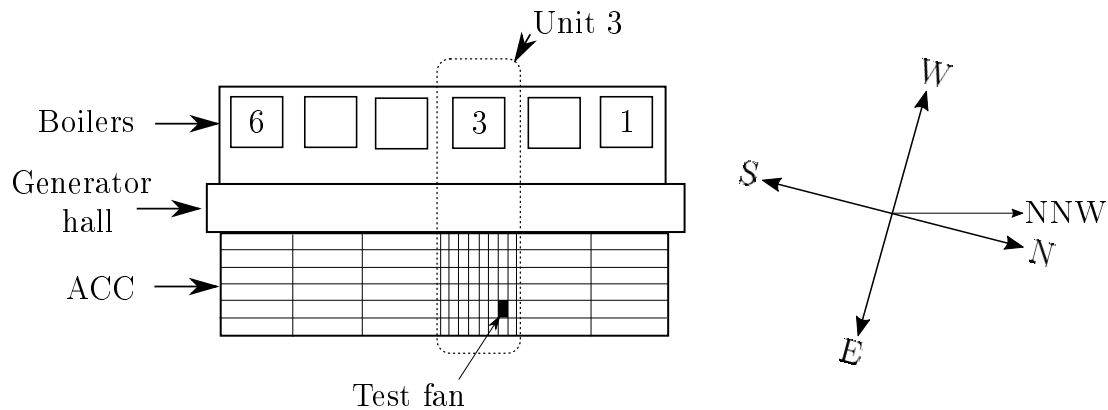


Figure 4.1: Position of test gearbox with regard to the power station.

The areas of investigation are: (1) Electrical power input of the induction motor; (2) Speed and torque on the gearbox input shaft; (3) Speed, torque and bending on the gearbox output shaft; (4) Gearbox vibration and temperature; (5) Wind speed, wind direction and air temperature.

4.1 Induction Motor Measurements

Measuring the instantaneous three phase power flowing into the induction motor allows the researcher to calculate the power output of the motor. The electrical power input of the induction motor is measured by means of current transformers (CTs) connected to each phase, and an oscilloscope. The measurements are taken at the breaker board, roughly 100 m from the motor. The

line to neutral voltage (V_{LN}) and the line current (I_L) of each phase is measured. Line losses were calculated to be negligible compared to rotor losses. Figure 4.2 shows how the CTs are connected to each phases.

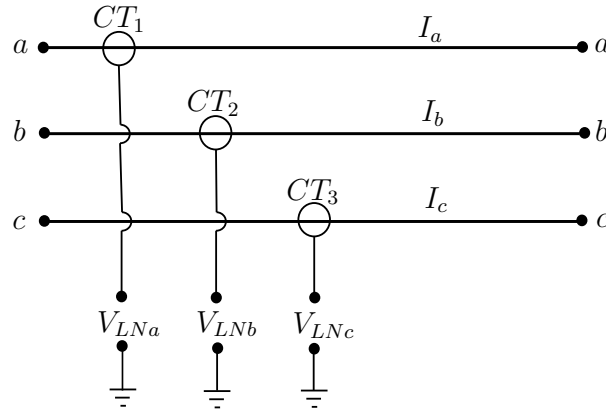


Figure 4.2: Current transformer connection.

Instantaneous power per phase can be calculated as,

$$P_a = V_{LNa}I_{La}, \quad (4.1)$$

$$P_b = V_{LNb}I_{Lb}, \quad (4.2)$$

$$P_c = V_{LNc}I_{Lc}. \quad (4.3)$$

The three phase instantaneous power flowing into the motor is then calculated as,

$$P_{in} = P_a + P_b + P_c. \quad (4.4)$$

Ideally it would be convenient to compare the mechanical power measured on the gearbox input shaft to the motor output power. Given the efficiency (η) of the motor, the output power can be calculated as,

$$P_{out} = \eta \cdot P_{in}. \quad (4.5)$$

From the speed, power and power factor measurements, it can be deduced that the motor operates between 70% and 85% of full load. The resulting motor efficiency is 95%, as stated by the manufacturer (WEG W22 Three-Phase Electric Motor). The power factor measurement is shown in Appendix E.

4.2 Strain Gauge Measurements

Torsional strain is measured on both gearbox shafts and is discussed in Section 3.2. This section discussed bending strain, measured on the output shaft. Appendix G.2 shows the various SG rosette mountings. Torsional strain on

the input shaft of the gearbox is related to torque with the calibration curve shown in Figure 3.38, while the torque on the output shaft is calculated with Equation 3.9.

As with the calculation of torque, the bending moment is also calculated by relating measured strain to a bending moment by using fundamental strength of material equations shown in Benham *et al.* (1996). Substituting

$$\sigma = E\epsilon \quad (4.6)$$

and

$$I = \frac{\pi r^4}{4} \quad (4.7)$$

into

$$\sigma_{\max} = \frac{Mr}{I}, \quad (4.8)$$

and rearranging, the bending moment can be calculated as

$$M = \frac{E\pi r^3}{4} \cdot \epsilon \quad (4.9)$$

where ϵ is the measured bending strain. The strain gauge positioning for measuring bending strain in a single plane is shown in Figure 4.3. The strain gauges are placed parallel to the shaft axis.

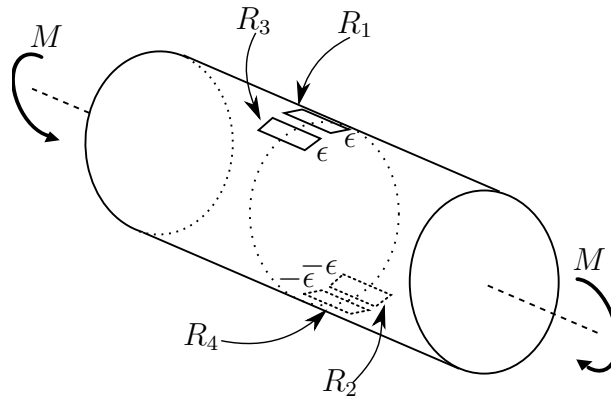


Figure 4.3: Full bridge strain gauge configuration used for bending strain measurement.

To capture the absolute shaft bending it is required to measure bending in two planes that are perpendicular to each other. The two vector components of the absolute shaft bending is measured with regard to the rotating coordinate system of the shaft. The rotational position of the shaft is required to transform the two bending vectors to the global coordinate system of the fan

bridge, and the proximity sensor can be used to track the shaft position. The position of the perpendicular bending planes and the position of the proximity sensor magnet is shown in Figure 4.4.

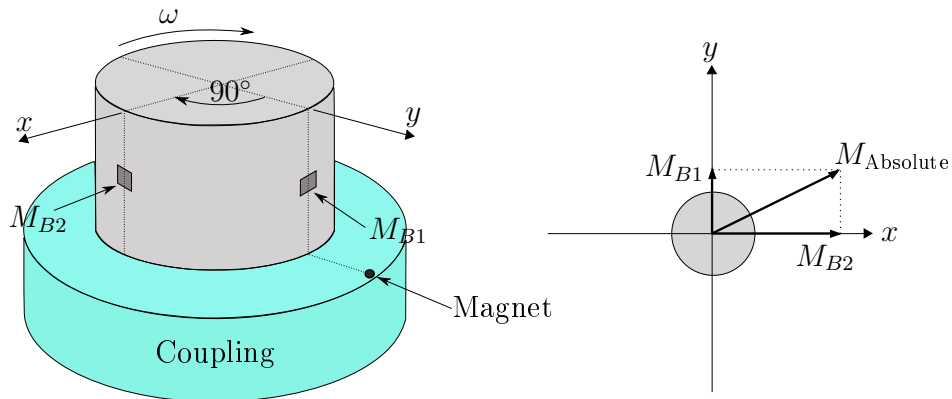


Figure 4.4: Perpendicular bending planes on the output shaft of the M4ACC gearbox.

4.3 Speed, Temperature and Vibration Measurements

Speed is measured on both shafts of the gearbox. This information is required to relate torque and power. The speed is measured by means of a hall-effect proximity sensor, using the slide-by technique discussed by Ramsden (2006). The position of the magnet placed on the output shaft is shown in Figure 4.4. The resolution chosen for the proximity sensor is one ping per revolution. Refer to Appendix G.3 for an illustration of the sensor installation.

A FLIR E8 thermal camera is used to measure the case temperature of the gearbox. The viscosity of gear lubricant is known to vary with temperature (Roelands, 1966). The gearbox power transfer capability then varies depending on the lubricant viscosity as the molecules in the lubricant become more resistive to shearing for low viscosities, or show little resistance to shearing for high viscosity (Andersson, 2014).

Accelerometers are used to measure the vibration of the gearbox during operation, allowing the measurement of high frequency vibrations (Hameed *et al.*, 2009). Wang and McFadden (1993) discuss condition monitoring with accelerometers, using a time-frequency distribution to analyse gear vibration. In this study a frequency spectrum is used to observe the gearbox frequencies.

Ambient air temperature, wind speed and wind direction is measured at a nearby power station. The weather station measurements are used throughout this chapter and are illustrated in Appendix F.

4.4 Experimental Information

The measurement equipment used and the operational states measured are discussed in this section. Appendix G.4 and G.5 shows what safety precautions were taken regarding the input and output shaft, and how the gearbox is installed in the ACC.

4.4.1 Hardware

The measurement setup consists of multiple sensors that are time synchronised using a QuantumX MX1601B DAQ. Eight sensors were placed on the gearbox, of which four were placed on the rotating shafts. The input shaft rotates at 1500 rpm and a counter weight for the SG-Link-LXRS is required to maintain shaft balance. The data measured on the rotating shafts has to be transmitted wirelessly. The positioning of the sensors are shown in Figure 4.5. The sensors and the hardware used to transfer the data wirelessly is labelled from 1 to 8, while other components are abbreviated. The integration of the measurement system and the recording of the data are performed as discussed in Section 2.3.3.

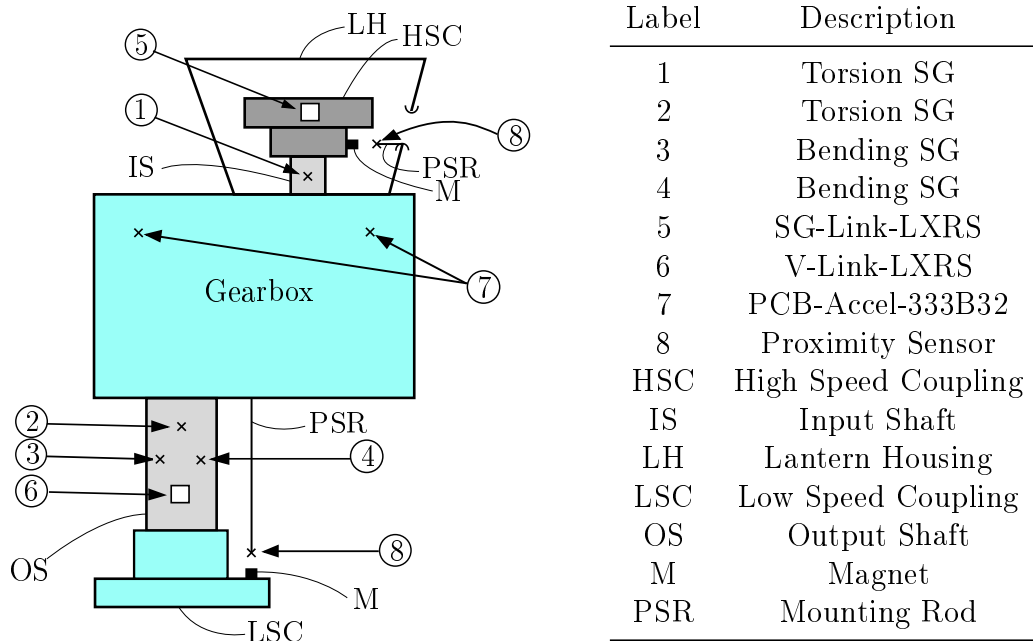


Figure 4.5: Sensors used on the M4ACC gearbox.

4.4.2 Operational States Measured

Measurements are taken during three states of gearbox operation viz. start-up, normal operation and run-down period. The gearbox experiences high

torsional loading during the start-up period because of the direct on-line connection of the motor (Pillay *et al.*, 2009). Measurements taken during normal operation hope to observe the effect of varying wind conditions on gearbox loading. Due to the battery life restrictions of the SG-Link-LXRS, measurements are limited to 5 min to 10 min intervals every 30 min to 60 min. This is done so that measurements can be taken for a longer period of the day. Torque transmission of the gearbox is measured during the run-down period of the fan to quantify the reverse loading effect of the fan momentum.

4.5 Results: Torque Transmission

Torque is measured on the input and output shaft of the gearbox, during all the operational states. The results obtained by Muiyser (2012) for the output shaft torsion correlate with the results found in this section. Previous research did not document torsional load for the input shaft.

4.5.1 Start-up Measurements

The start-up measurements aim to quantify the load experienced by the gearbox during the start-up period. Start-up torque measured on three separate days is compared in Figures 4.6 to 4.8 to observe the effect of wind on torque. Table 4.1 gives the peak start-up torque on both the gearbox shafts, as well as the wind conditions at that time.

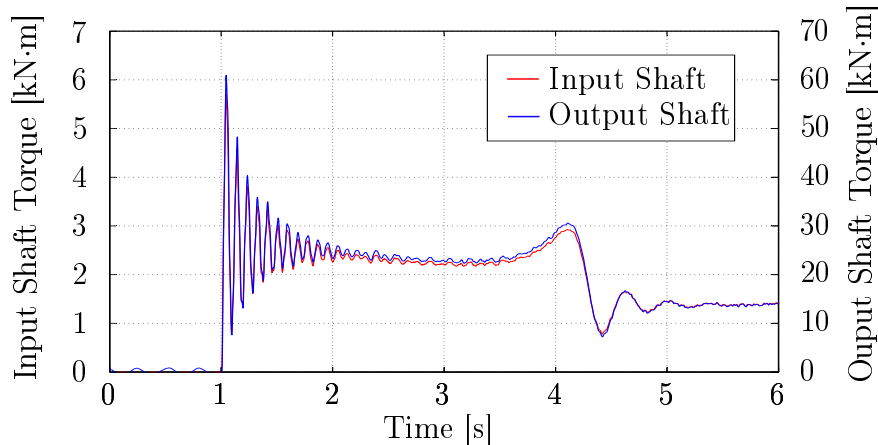


Figure 4.6: Start-up torque measured on 19 April 2016, at 13:30.

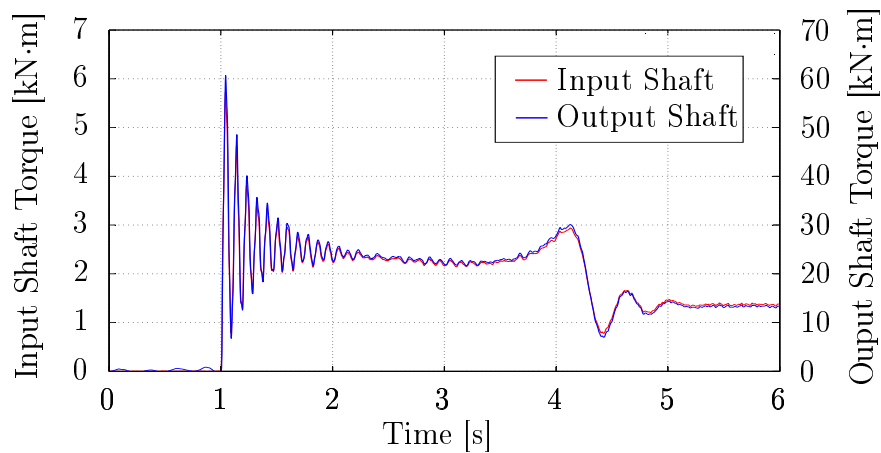


Figure 4.7: Start-up torque measured on 20 April 2016, at 15:30.

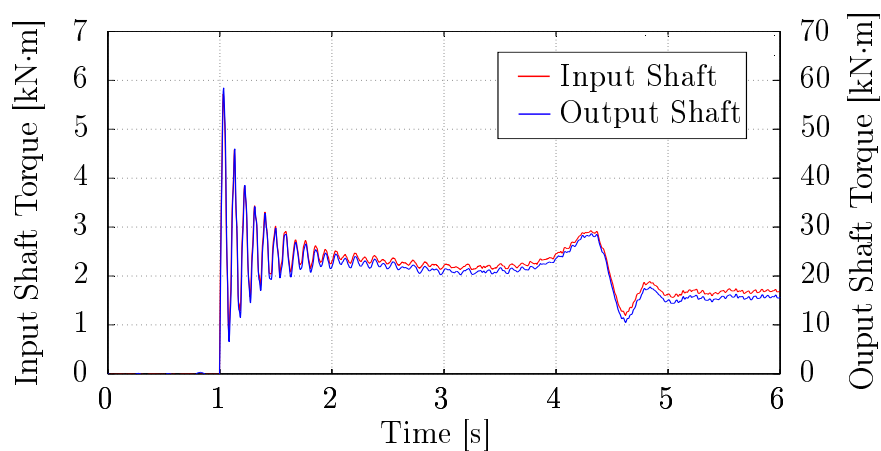


Figure 4.8: Start-up torque measured on 21 April 2016, at 11:40.

Table 4.1: Peak start-up torque.

Date	Input Shaft [N · m]	Ouput Shaft [N · m]	Wind Speed [m/s]	Wind Direction
19/04	5839	61 149	11.5	30°
20/04	5830	60 678	10	20°
21/04	5823	58 428	28	43°

The torque experienced by the input shaft is not significantly effected by the varying wind conditions during start-up. Torsion on the output shaft of the gearbox becomes affected when the wind speed increases and the wind direction becomes more easterly. The fan is positioned near the edge of the

ACC, thus wind that blows from the east reduces the load on the fan, as natural draft forces wind into the fan.

The start-up speed of both the gearbox shafts is measured and shown in Figures 4.9 and 4.10. The speed of both shafts increases linearly and becomes constant at normal operation. The fan reaches an operational speed of 127.6 rpm in 3.163s, while the speed of the input shaft reaches 1500 rpm.

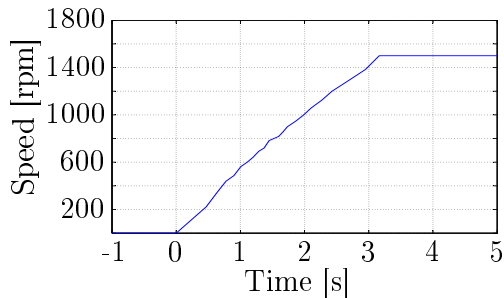


Figure 4.9: Input shaft speed during start-up.

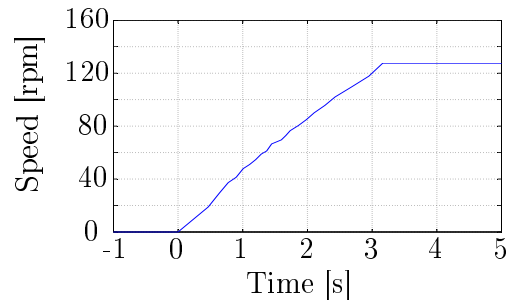


Figure 4.10: Output shaft speed during start-up.

Power transfer from the motor to the fan is measured to observe how much energy passes through the gearbox during the start-up period. The motor power output is calculated with Equation 4.5. Figure 4.11 shows the power transfer through the system during start-up.

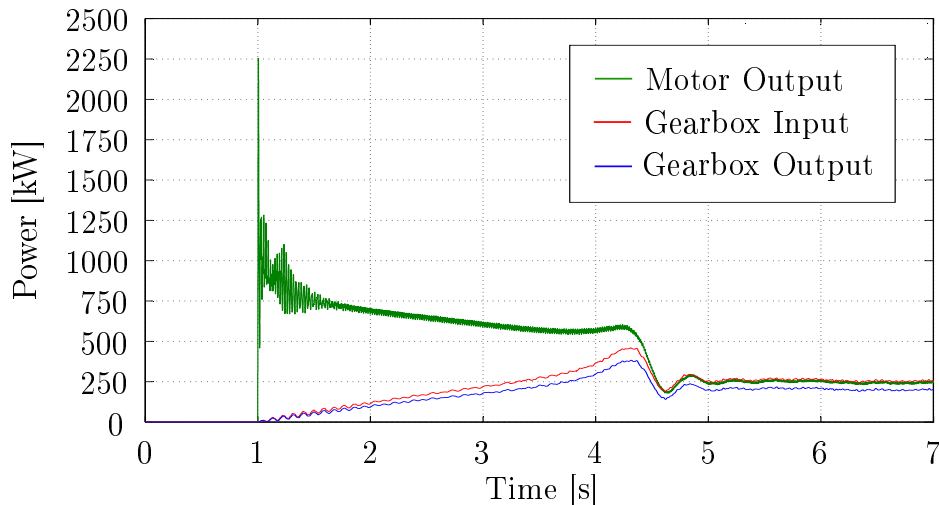


Figure 4.11: Comparison of power transfer from the motor to the gearbox output, measured on 21 April 016.

Slip is maximum during start-up of an induction motor, inducing high rotor current. Because of transformer action the stator currents are thus excessively high (Garg and Tomar, 2015). This causes start-up current to be typically 6 to 8 times higher than operational current for induction motors (Pillay *et al.*, 2009). The measured peak start-up power is 7.89 times higher than the rated

power of the motor ($P_{\text{start}} = 2250 \text{ kW}$ vs. $P_{\text{rated}} = 285 \text{ kW}$). The excessive start-up power is not transferred to the gearbox, as the slip is still high, i.e. no shaft rotation. Figure 4.12 gives a better illustration of the power transfer from the input to the output shaft of the gearbox. The gearbox power transfer capability is lower during the start-up period of the gearbox because the gearbox is still at ambient temperature. Power transfer from the input to the output shaft of the gearbox is shown in Appendix H.1 for the start-ups measured from 19–21 April.

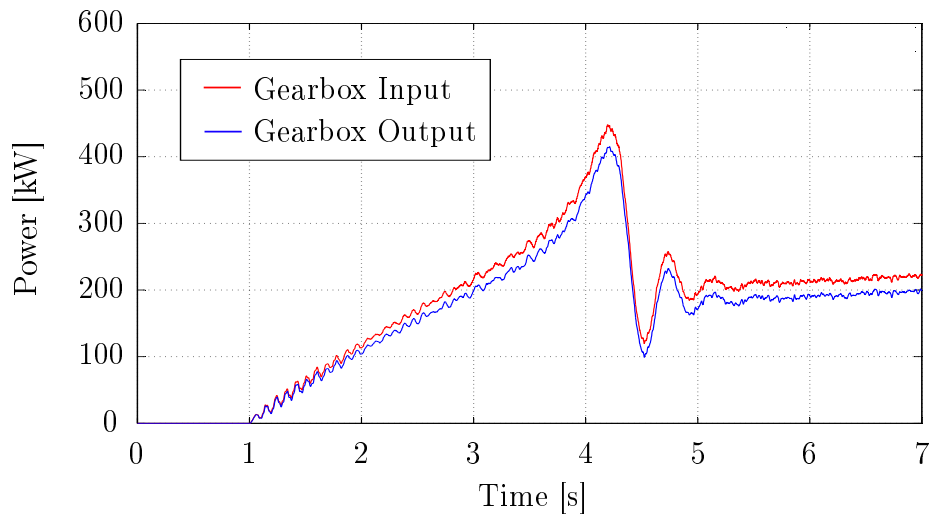


Figure 4.12: Start-up power transmission of the gearbox.

Figure 4.13 shows the temperature measured on the outside of the gearbox with a FLIR E8 thermal camera. The temperature measurements are taken to observe the time needed for the gearbox to reach operational temperature. The temperature is measured at the same position for consistency. The gearbox reaches its operational temperature of 50°C to 55°C after 2 hours of operation. The lubricant inside the gearbox needs to be at operational temperature for optimal power transfer capability.

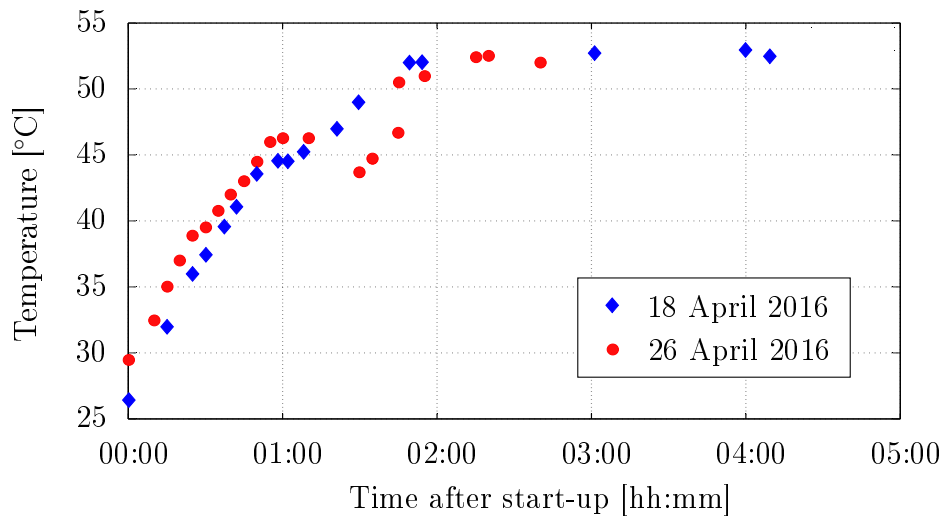


Figure 4.13: Temperature change of gearbox casing.

4.5.2 Normal Operation Measurements

Torque measurements during normal operation allows the researcher to observe how torque is transferred through the gearbox while the gearbox temperature increases. Figure 4.14 shows the instantaneous power that is measured at the input of the induction motor. The average power is 212.4 kW, with a maximum and minimum of 250.0 kW and 185.5 kW respectively.

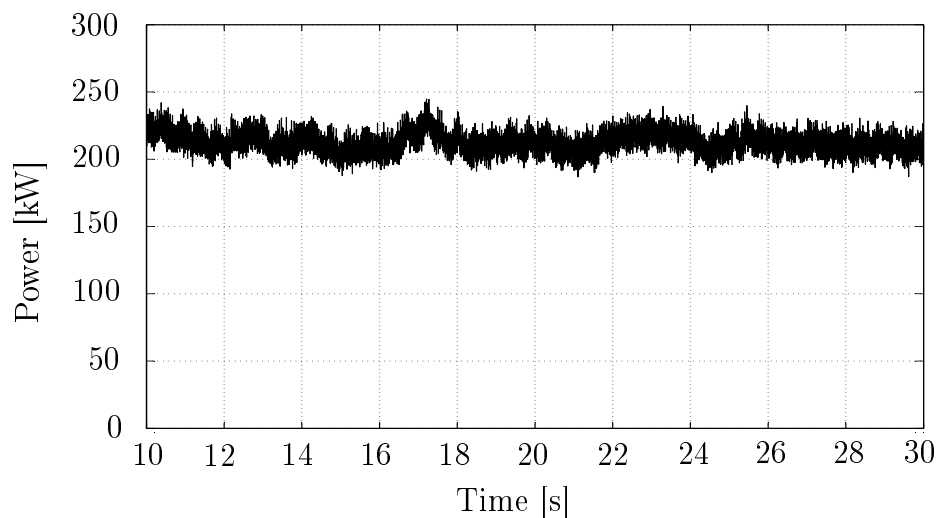


Figure 4.14: Electric power measured at the switch board, roughly 100 m from the motor.

The power signal has noise on it, and performing a FFT on the signal will expose the frequency components that are present. The measured signal was 10s long, the FFT resolution is 0.025 Hz and a Hamming window was used. Figure 4.15 confirms that the fundamental frequency of the power supply

($f_1 = 50$ Hz) and the second harmonic ($f_2 = 100$ Hz) contribute to the signal noise.

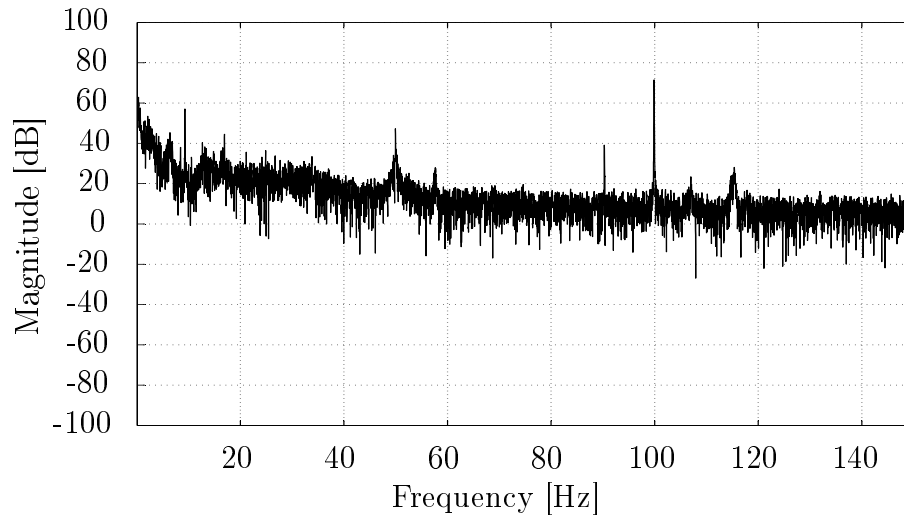


Figure 4.15: Frequency spectrum plot of instantaneous power.

A low pass filter eliminates the high frequency components of the power signal. The filtered instantaneous power signal is shown in Figure 4.16, where the motor output power is compared to the measured input power of the gearbox. The input shaft of the gearbox is connected to the motor output shaft by means of a flanged coupling.

In theory the gearbox input power should be within 1% of motor output power, as the power is transferred with a rigid coupling. Figure 4.16 shows a comparison between the motor output power (measured with CTs) and the gearbox input power (measured with SGs), with a tolerance on the gearbox input power measurement. The measured gearbox input power is 2.15% higher than the motor output power, which falls within the 4.5% tolerance band of the input shaft measurements. The results show that the SG measurements on the input shaft correlate well with the CT measurements at the switch board.

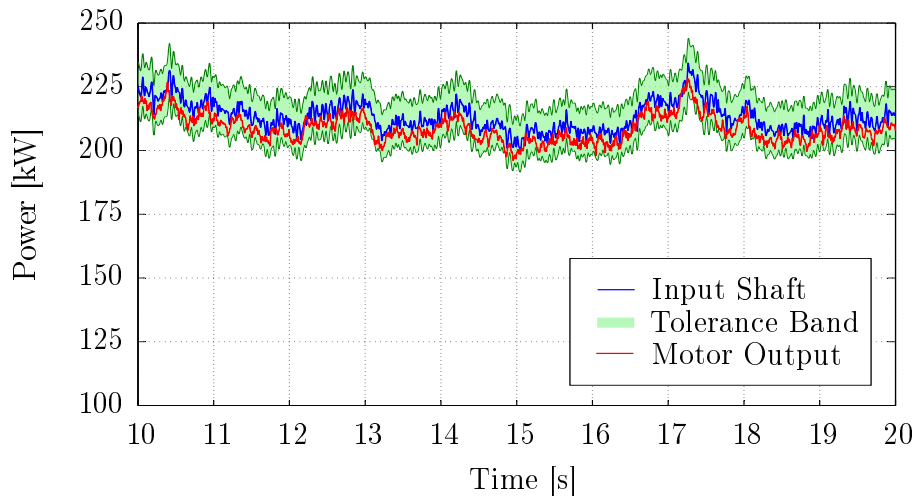


Figure 4.16: Gearbox input shaft power with measurement tolerance band and motor output power, measured on 26 April 2016.

Torque measurements from both shafts of the gearbox are compared at different running times in Figures 4.17 to 4.19. The input shaft torque is obtained with the calibration curve shown in Figure 3.38 and corrected for increased operational temperature with Figure 3.39; it is assumed that the input shaft reaches an operational temperature of 65°C after two hours of operation. Importantly there is a $\pm 4.5\%$ tolerance on the input shaft measurements. The output shaft torque is calculated with Equation 3.9, using a constant elastic modulus of 207 GPa and a Poisson's ratio of 0.29.

There is no phase shift between the input and output shaft torque measurements, implying that the gears remain in rigid contact with one another in one rotational direction. The torque that is transferred from the input to the output shaft varies with running time. Figure 4.17 shows that 90.4% of the input shaft torque is transferred to the output shaft directly after start-up. One hour after start-up 95.3% of the torque is transferred from the input to the output shaft, as shown in Figure 4.18. The amount of torque transferred then lowers to 91.6% after two hours of running time, as shown in Figure 4.19. It is suspected that the change in the amount of torque transferred can be accredited to a combination of the material properties and operational temperature of the shafts. The exact operational temperature of the input and output shafts are unknown, but the temperatures increase at different rates. The varying shaft temperature effects the elastic modulus of the respective shafts, while a constant elastic modulus is assumed for the output shaft.

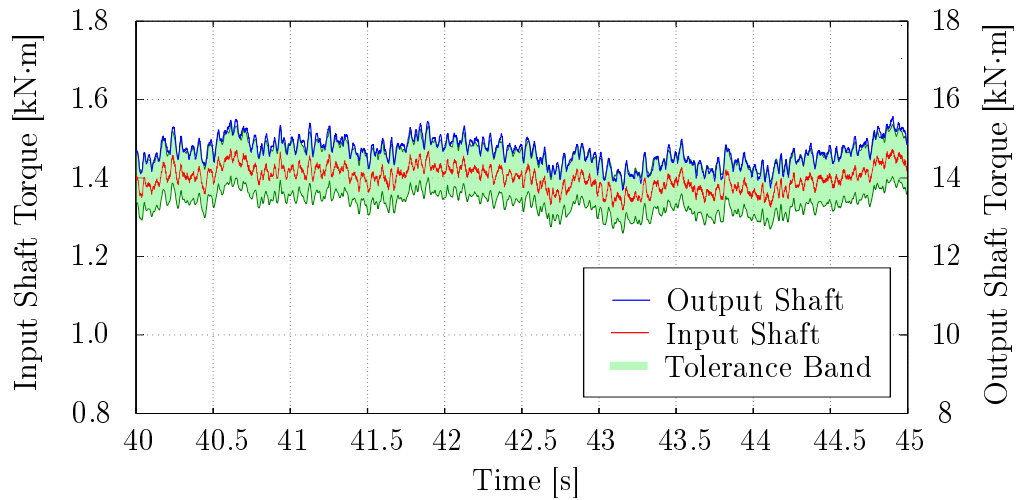


Figure 4.17: Torque transmission from the input shaft to the output shaft directly after start-up.

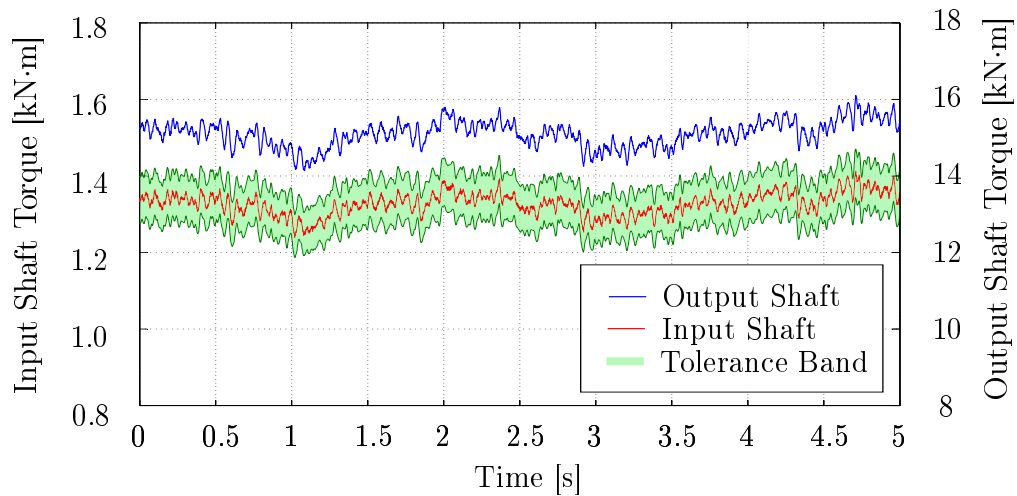


Figure 4.18: Torque transmission from the input to output shaft one hour after start-up.

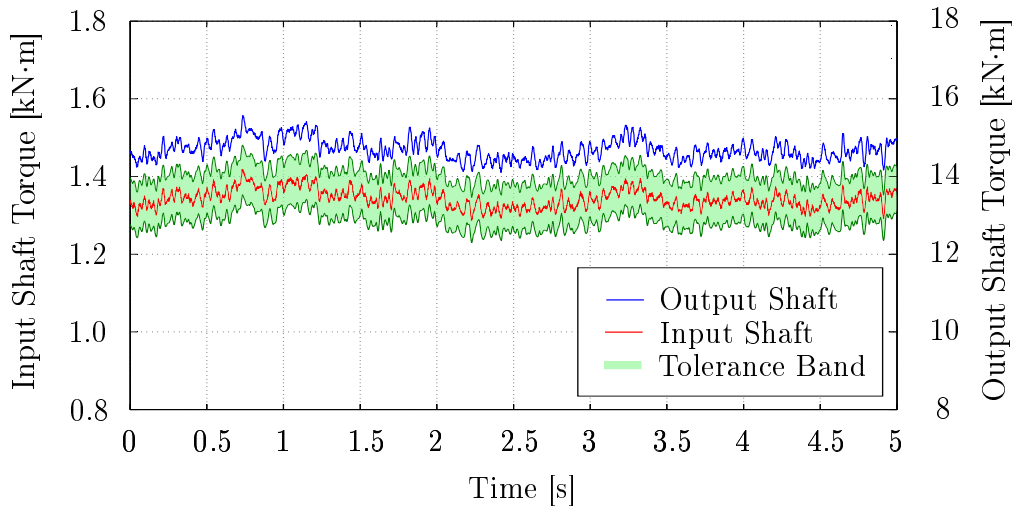


Figure 4.19: Torque transmission from the input to output shaft two hours after start-up.

FFTs are performed on the torque data measured on both the input and output shafts of the gearbox. The measured signal is 10 min long, the FFT resolution is 0.002 Hz and a Hamming window was used. Figures 4.20 and 4.21 show the frequency spectrum plots of the torque experienced by both gearbox shafts. It is noted that the frequency peaks occur at the same location for both gearbox shafts with the amplitudes scaled by the gear ratio.

The first and most dominant frequency is at 0.264 Hz, which is likely caused by varying wind speed and direction. The frequency of rotation of both input and output shafts are shown at 2.113 Hz and 24.87 Hz respectively. Another significant peak is located at 16.92 Hz, which can be attributed to the frequency at which blades pass underneath the bridge. The peak located at 9.282 Hz is caused by the intermediate gear rotational frequency, as discussed in Section 4.7.

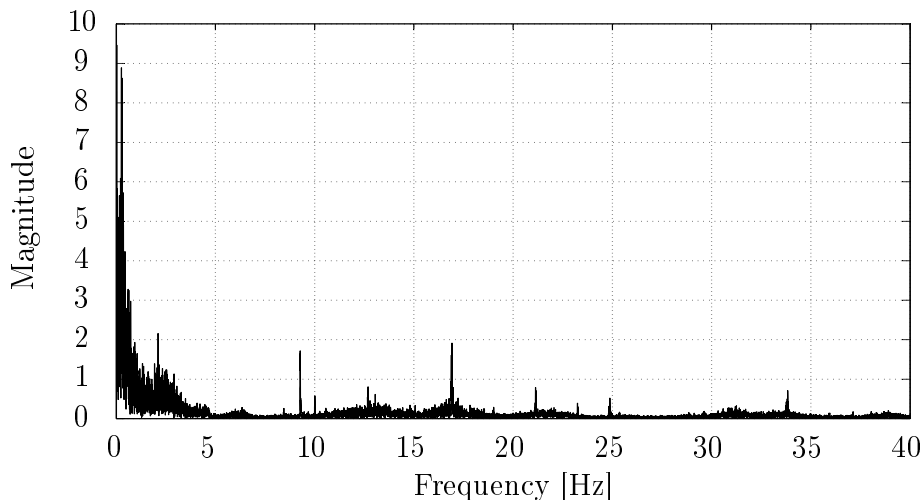


Figure 4.20: Frequency spectrum plot of the input shaft torque.

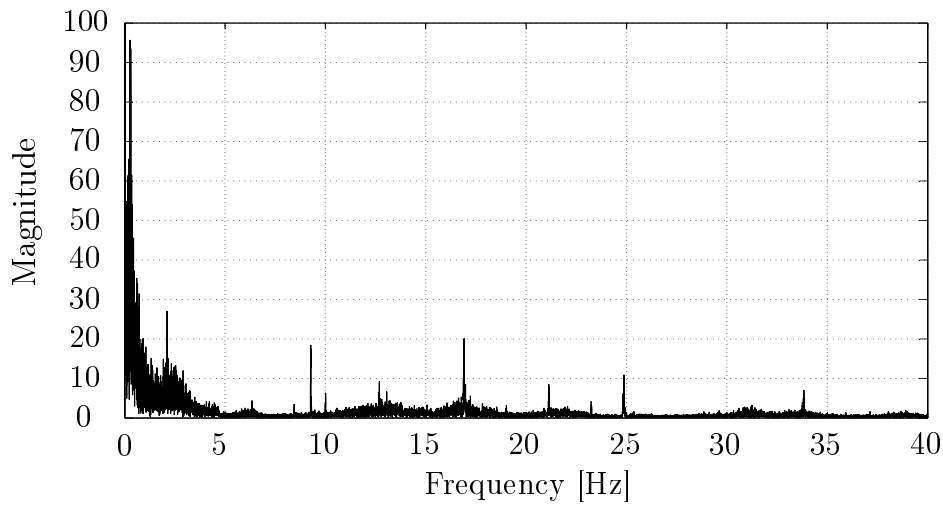


Figure 4.21: Frequency spectrum plot of the output shaft torque.

4.5.3 Run-down Measurements

The torque is measured on both shafts of the gearbox during the run-down period of the fan on 24/04/2016. The speed of the output shaft during the run-down period is shown in Figure 4.22. The shaft slows down exponentially and stops after 19.65 s. Reverse loading is visible in Figure 4.23 as the fan continues to drive the gearbox during the run-down period. The peak torque in the reverse direction is $430 \text{ N} \cdot \text{m}$ and $5380 \text{ N} \cdot \text{m}$ on the input and output shafts.

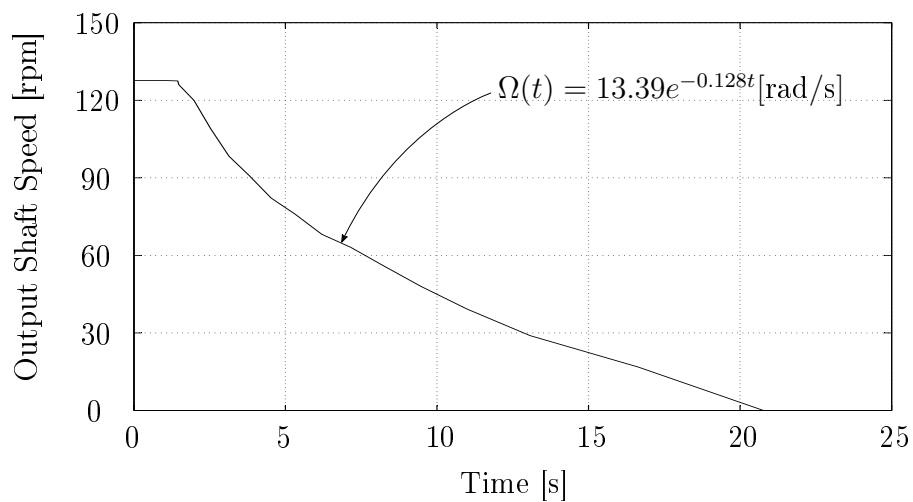


Figure 4.22: Speed of the output shaft during the run-down period.

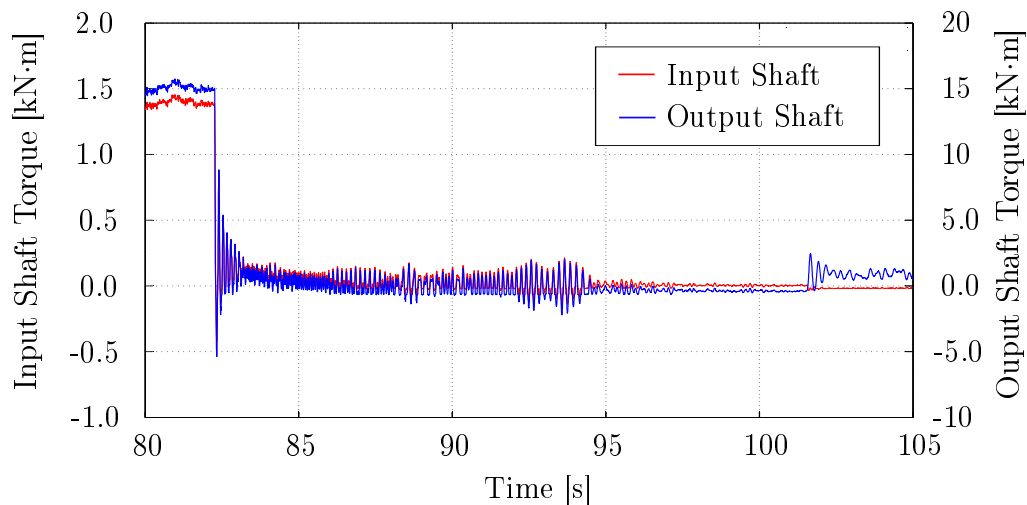


Figure 4.23: Torque measured on both gearbox shafts during the run-down period.

A spectrogram of the frequencies present in the torque measured on the output shaft is shown in Figure 4.24. A window overlap of 99% was used for maximum resolution. By making use of a well-known Rayleigh principal, Yntema (1955) expresses the natural frequency of a rotating beam as

$$f_{\text{Blade}}(t) = \frac{1}{2\pi} \cdot \sqrt{\omega_{\text{static}}^2 + k\Omega(t)^2}. \quad (4.10)$$

The fan blade is approximated as a rotating beam, allowing the calculation of its frequency (f_{Blade}) with Equation 4.10. k is known as a Southwell coefficient and can be solved by setting: (1) ω_{static} equal to 33.929 rad/s, (Muiser, 2012); (2) $\Omega(0)$ equal to 13.39 rad/s, from Figure 4.22; and (3) $f_{\text{Blade}}(0)$ equal to 39.785 rad/s, from Figure 4.36. Equation 4.10 is then written as

$$f_{\text{Blade}}(t) = \sqrt{29.16 + 10.96e^{-0.256t}}, \quad (4.11)$$

while the rotational frequency of the input shaft can be written as

$$f_{\text{Input}}(t) = 25e^{-0.128t}, \quad (4.12)$$

Equation 4.11 and 4.12 are plotted onto Figure 4.24. The input shaft rotational frequency is linearly related to the rotational speed of the output shaft. The natural frequency of the fan blades is dependant on the rotational speed of the output shaft, as the centrifugal force acting on the blade increases the blade stiffness during rotation. The rotational frequency of the input shaft and the natural frequency of the blades are related to the output shaft speed in Figure 4.25.

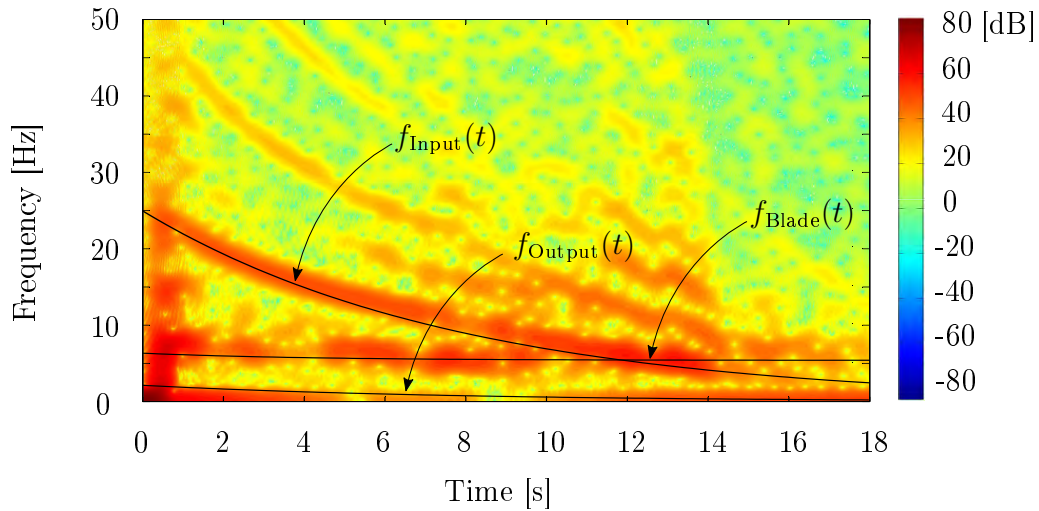


Figure 4.24: Spectrogram of output shaft torque during the run-down period.

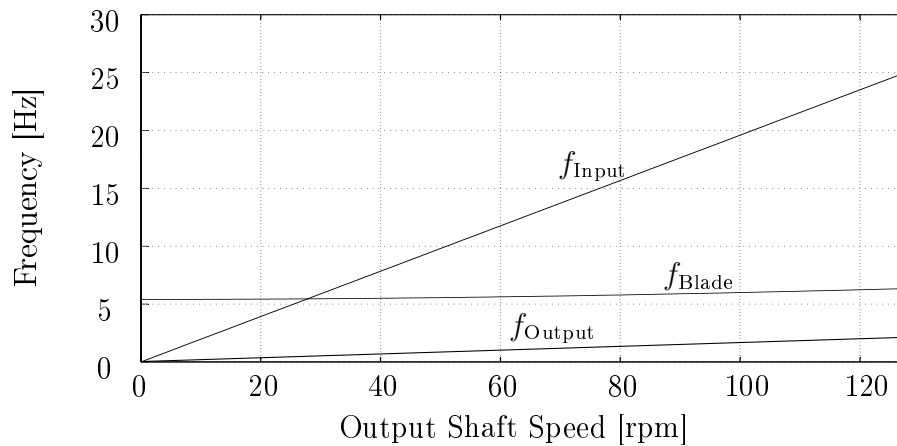


Figure 4.25: Rotational frequency of the input and output shafts of the gearbox, and the natural frequency of the fan blades versus output shaft speed.

4.6 Results: Output Shaft Bending

Bending measurements are taken during varying wind conditions to identify the bending forces the output shaft is subjected to. The bending measurement results are displayed on a polar plot that is orientated with regard to the global static coordinate system of the fan-bridge, as shown in Figure 4.26. Refer to Appendix H.2 to view the bending data over time. The fan position with regard to the power station is shown in Figure 4.1, but to clarify, the y -axis of the global coordinate system is directed in the direction of the power station boilers, and the x -axis is directed NNW. The z -axis is then positioned

according to right-hand-rule convention. Bending is calculated as described in Section 4.2.

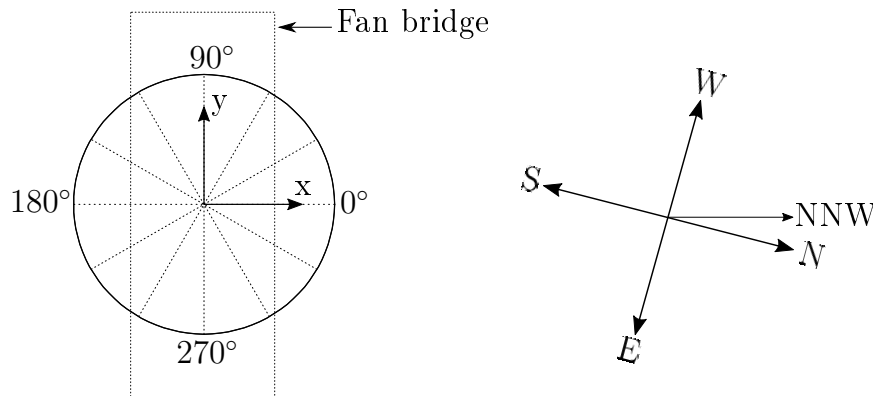


Figure 4.26: Orientation of polar plot with regard to the fan-bridge.

Figure 4.27 shows the shaft bending for 20 rotations, three different wind directions and constant wind speed. Table 4.2 shows the wind conditions for each of the polar plots shown in Figure 4.27(a-c). Bending on the output shaft is directed away from the oncoming wind i.e. the output shaft bends west for a wind blowing from the east. The bending moment reaches values in excess of $4000 \text{ N} \cdot \text{m}$ for the cases shown in Figure 4.27. It is also noted that the measured bending signal varies in magnitude and angle for each rotation of the shaft.

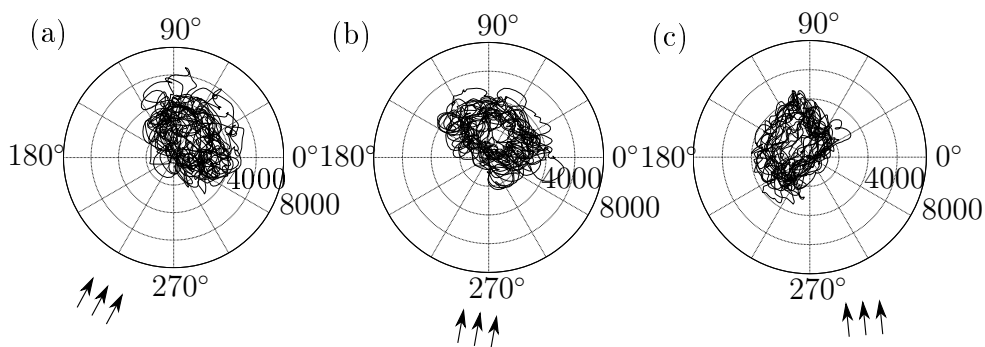


Figure 4.27: Bending experienced by the output shaft during three wind directions and constant wind speed.

Table 4.2: Wind speed and direction.

Figure 4.27	Speed [m/s]	Direction
(a)	25.4	116 °ESE
(b)	25.6	92 °E
(c)	24.6	66 °ENE

A FFT is used to isolate the dominant bending frequencies present in the bending signal. The signal length is 5 min, the frequency resolution is 0.0021 Hz and a Hamming window was used. Figure 4.28 shows the frequency spectrum plot of the bending measurements. The most dominant frequency is the rotational speed of the output shaft, $f_1 = 2.113$ Hz. Other notable frequency components at $f_2 = 4.23$ Hz and $f_3 = 6.354$ Hz, are the natural frequencies of the fan-bridge and the fan blades (Muiyser, 2012).

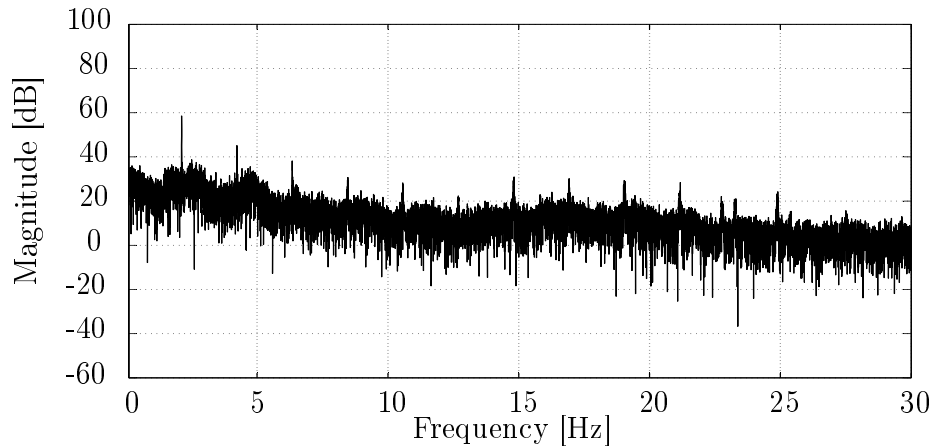


Figure 4.28: Frequency spectrum plot of output shaft bending.

The different frequency components in the measured bending signal can be isolated using digital filters in Matlab R2013b. Figure 4.30(i-iv) shows the bending component that occurs in the given frequency ranges for the wind condition shown in Figure 4.27(b). The bending components present in Figure 4.27(a) and Figure 4.27(c) are shown in Appendix H.3. It is assumed that wind speed and direction is a variable that changes its quantity at a frequency below 2 Hz. Applying a low pass filter to the measured bending data allows the bending moment caused by wind to be isolated. The bending moment induced by wind is shown in Figure 4.30(i), where it is notable that the signal is smoother and directed away from the oncoming wind.

A bending moment at the frequency of rotation, f_1 in Figure 4.28, makes a significant contribution to the moment. A bandpass filter is used to isolate

the moment that occurs in the frequency band of 2 Hz to 2.2 Hz. This moment is caused by a shifted center of mass of the fan blades and unbalanced blade loading. Two counteracting bending moments are caused by the shifted center of mass. The first bending moment (M_{gr}) is caused by the gravitational pull on the center of mass, while the second bending moment (M_{cen}) is caused by the centrifugal force on the center of mass. Distorted fan inlet air flow causes unbalanced blade lift, resulting in a third bending moment (M_{bl}). Figure 4.29 illustrates how the bending moments acted upon the output shaft.

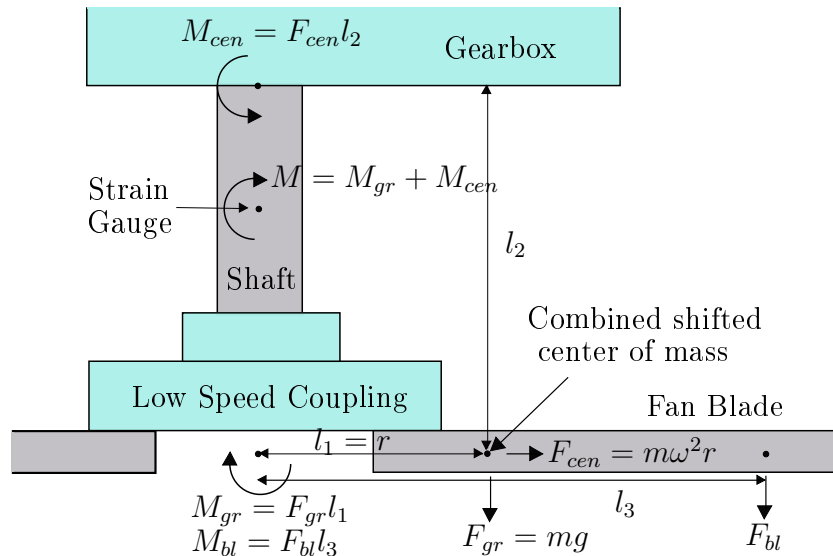


Figure 4.29: Bending forces present on the output shaft at rotational frequency.

Figure 4.30(ii) shows the bending component that is caused by the shifted center of mass of the fan. The shaft experiences a bending moment of $1500 \text{ N} \cdot \text{m}$ to $2500 \text{ N} \cdot \text{m}$ which rotates with the shaft. The elliptical shape of the bending moment (in the polar plot) is caused by the unbalanced blade lift. The bending moment caused by the shifted center of mass is constant and directly proportional to the radius of this center of mass, while the bending caused by unbalanced blade lift varies, depending on blade pitch angle and fan inlet air flow. The combined output shaft bending can be expressed as

$$M = mr \cdot (\omega^2 l_2 - g) - M_{bl}, \quad (4.13)$$

where,

M is the combined output shaft bending [$\text{N} \cdot \text{m}$],

M_{bl} is a moment induced by unbalanced blade lift [$\text{N} \cdot \text{m}$],

m is the mass of the entire fan [kg],

r is the radius of the shifted center of mass of the entire fan [m],

ω is the rotational speed of the fan [rad/s],

l_2 is the length of the moment arm [m],

g is gravitational acceleration [m/s²].

Muiyser (2012) found that blades on the side of the oncoming wind experience more bending in the downward direction than the blades on the opposite side. Meyer (2005) confirmed that flow separation occurs near the inlet of the fan's bell-mouth for the edge fan, while oblique flow into the fan causes inlet flow losses for the second row of fans. A combination of flow separation at the fan inlet and oblique flow into the fan, leads to a low pressure zone on the side of the oncoming wind, and forces the fan blades to experience unbalanced lifting.

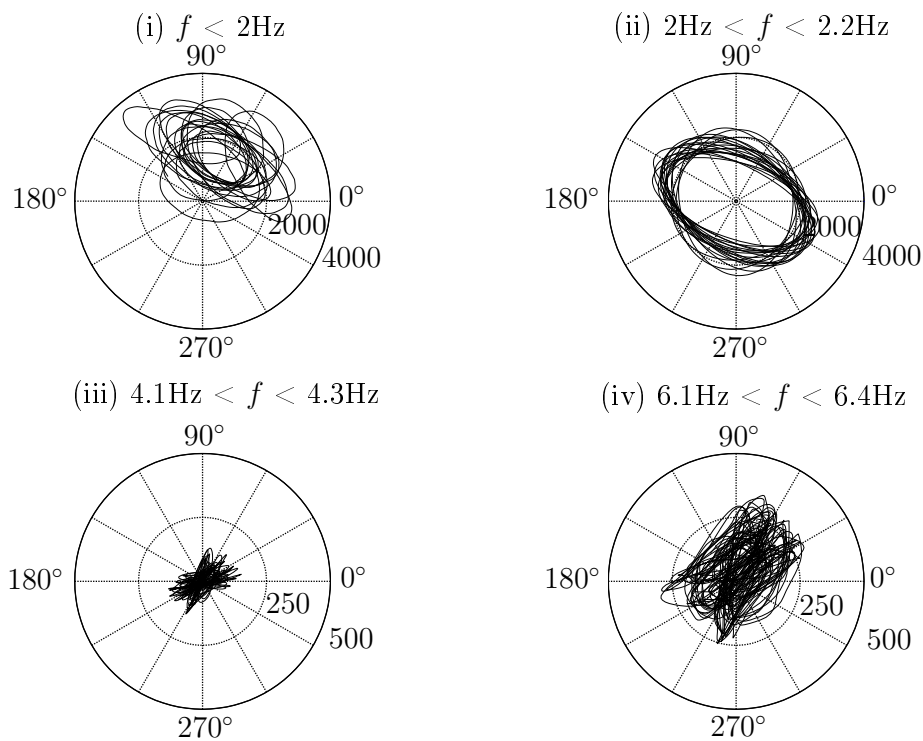


Figure 4.30: Polar plot of bending components present in the bending data for a wind speed and direction of 25.6 m/s and 92°E.

The components of bending that occur at f_2 and f_3 can be viewed in Figure 4.30(iii-iv). The bending induced at f_2 and f_3 is small compared to the frequencies below 2 Hz and at f_1 , and it does not justify individual analysis.

Figure 4.30 illustrated that filters can be used to isolate the bending components that cause bending at different frequencies. Varying wind conditions

are investigated in Figures 4.31 to 4.33 for 20 shaft rotations. It is clear that wind direction and speed play a combined role in the bending moment induced onto the output shaft of the gearbox. The wind direction has an effect when it becomes more easterly, i.e. flows directly into the tested fan.

In Figure 4.31 the wind speed is high but the wind direction is NNE, causing it to distort before reaching the test fan. The wind therefore does not cause off-centered bending. Figure 4.32 shows the bending associated with a low wind speed but a slightly more easterly direction. The low wind speed is however not enough to cause significant off-center bending of the shaft for all 20 rotations. Figure 4.33 shows that an easterly wind with a slightly higher wind speed of 11 m/s can cause the shaft to bend off-center.

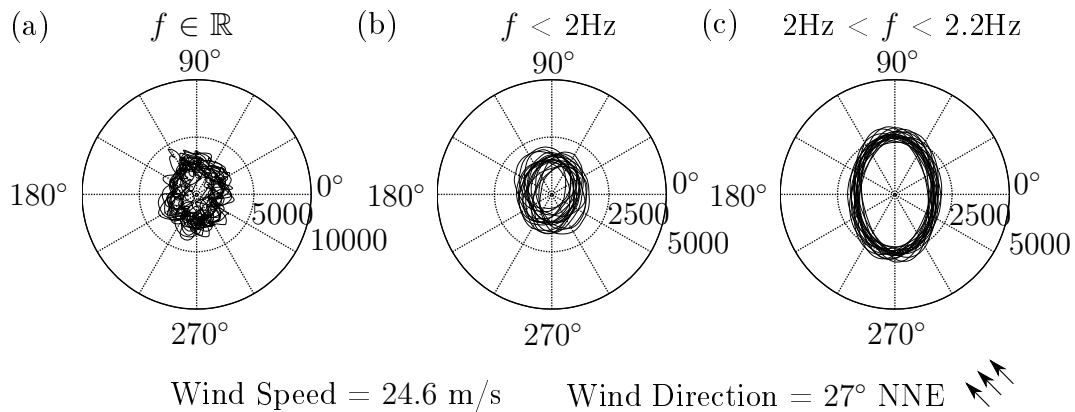


Figure 4.31: Polar plot of bending experienced by the shaft on 25 April 2016, at 13:00.

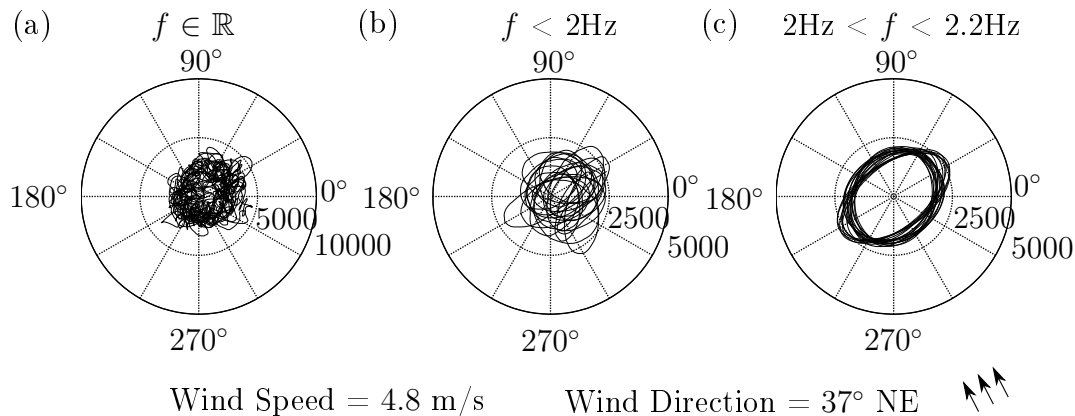


Figure 4.32: Polar plot of bending experienced by the shaft on 25 April 2016, at 11:00.

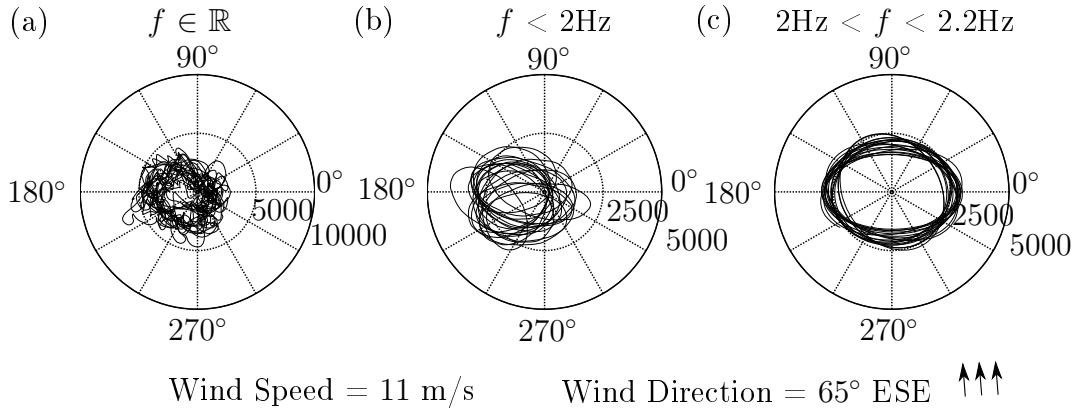


Figure 4.33: Polar plot of bending experienced by the shaft on 25 April 2016, at 16:00.

4.7 Results: Gearbox Vibration

The vibration of the gearbox is measured in the z and x directions of the global coordinate system depicted in Figure 4.26. The vibration is measured with two single-axis PCB-Accel-333B32. FFTs are performed on the vibration signals to identify the frequencies present in the motor-gearbox-fan system. The vibration signal length is 10 min, the FFT resolution is 0.0017 Hz and a Hamming window is used. Figure 4.34 and 4.35 show the frequency spectrum plots with a scale of 0 Hz to 200 Hz, with the shaded area representing the frequency range plotted in Figure 4.36 and 4.37. The frequency spectrum is plotted on these scales to capture all the fundamental frequencies of the gearbox, excluding the mesh frequency of the high speed gear pair.

Winterton (1991) gives the five fundamental frequencies associated with gear pairs as: (1) the pinion rotational frequency (f_{rp}); (2) the gear rotational frequency (f_{rg}); (3) the mesh frequency of the gear teeth (f_{gtm}); (4) the tooth repeat frequency (f_{tr}); and (5), the assembly phase passage frequency (f_{ap}). The fundamental frequencies are calculated as

$$f_{rp} = \frac{R_g}{60}, \quad (4.14)$$

$$f_{rg} = \frac{R_p}{60}, \quad (4.15)$$

$$f_{gtm} = f_{rp} \cdot N_{pt} = f_{rg} \cdot N_{gt}, \quad (4.16)$$

$$f_{tr} = \frac{f_{gtm} N_{ap}}{N_{gt} N_{pt}}, \text{ and} \quad (4.17)$$

$$f_{ap} = \frac{f_m}{N_{ap}}. \quad (4.18)$$

where,

$R_{rg/rp}$ is the rotational speed of the gear/pinion [rpm],

$N_{rg/rp}$ is the number of teeth on the gear/pinion,

N_{ap} is the number of assembly phases.

The mesh frequency of the low speed gear pair (f_{gm}) is visible in Figure 4.34 and 4.35 at 166.7 Hz. The peaks at 50 Hz and 100 Hz, in Figure 4.34 and 4.35, are associated with the first and second harmonic of the power supply (f_{1e} and f_{2e}). The peak at 80 Hz is located at five times the blade pass frequency ($5 \times f_{bp}$).

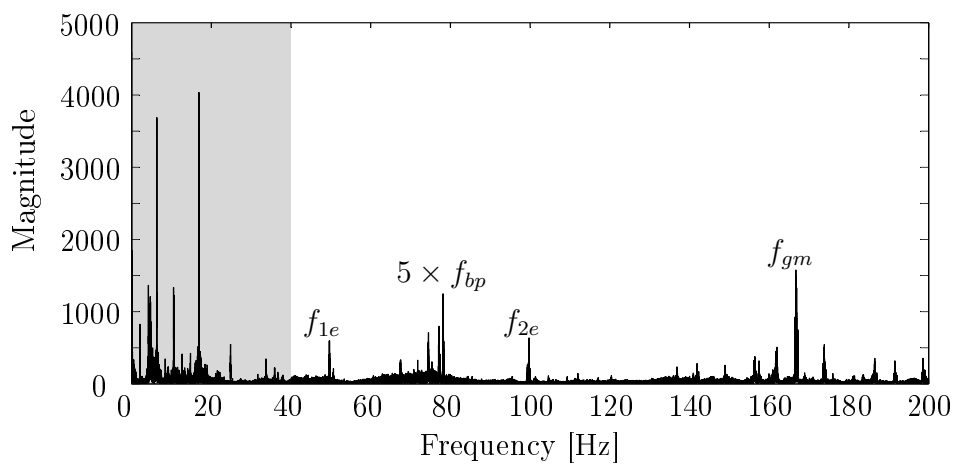


Figure 4.34: Frequency spectrum of gearbox vibration in the z -direction, from 0 Hz to 200 Hz.

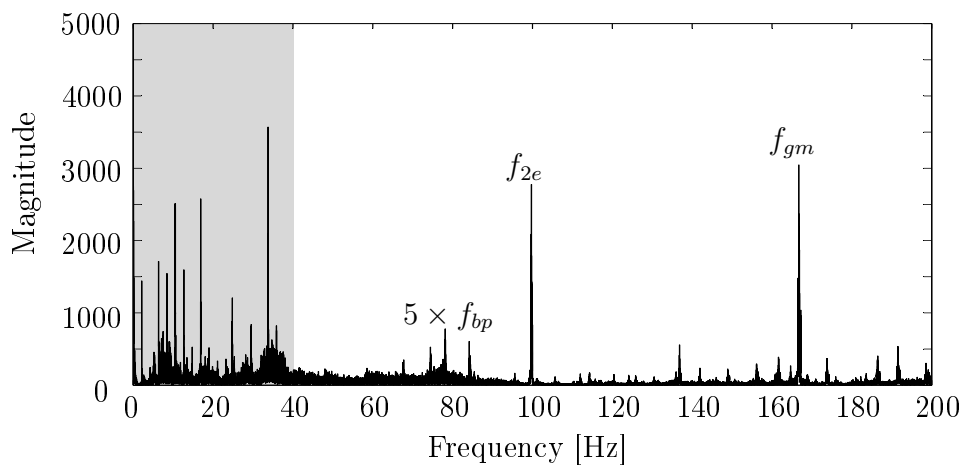


Figure 4.35: Frequency spectrum of gearbox vibration in the x -direction, from 0 Hz to 200 Hz.

In Figures 4.36 and 4.37 the focus is on the frequency components below 40 Hz. The frequency spectrum plot in the z -direction differs from the x -direction plot, but still share common frequency components. The shaft rotational frequencies (f_{Input} and f_{Output}) are visible in both the z -direction and the x -direction plots, at 2.109 Hz and 24.83 Hz. The natural frequency of the fan blades ($f_{\text{Blade}} = 6.332$ Hz), and the frequency at which the fan blades pass beneath the bridge ($f_{bp} = 16.89$ Hz), is also visible in both x and z directions. The rotational frequency of the intermediate gears (f_{img}) is visible at 10.54 Hz in both x and z directions, with visible side bands at 8.441 Hz and 12.66 Hz in Figure 4.37. The natural frequency of the fan bridge (f_{fb}) is seen in Figure 4.36 at 4.214 Hz. The natural frequency of the fan bridge is not visible in Figure 4.37, indicating vertical displacement of the fan bridge.

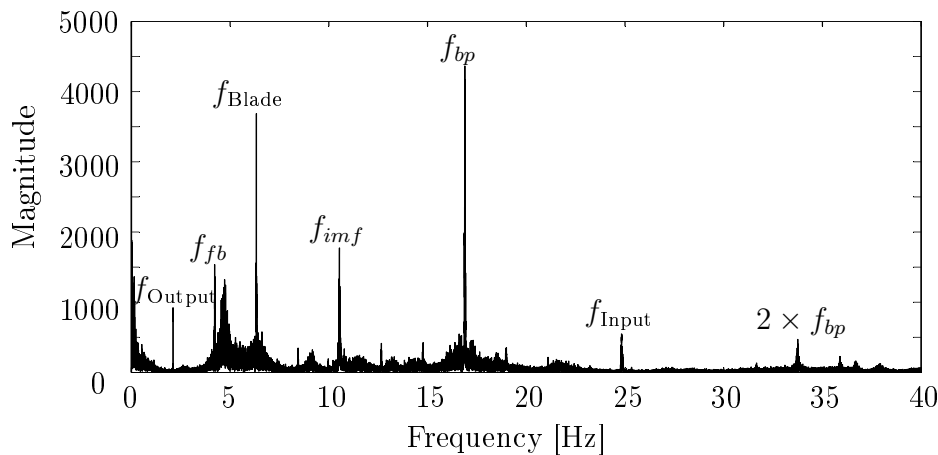


Figure 4.36: Frequency spectrum of gearbox vibration in the z -direction, from 0 Hz to 40 Hz.

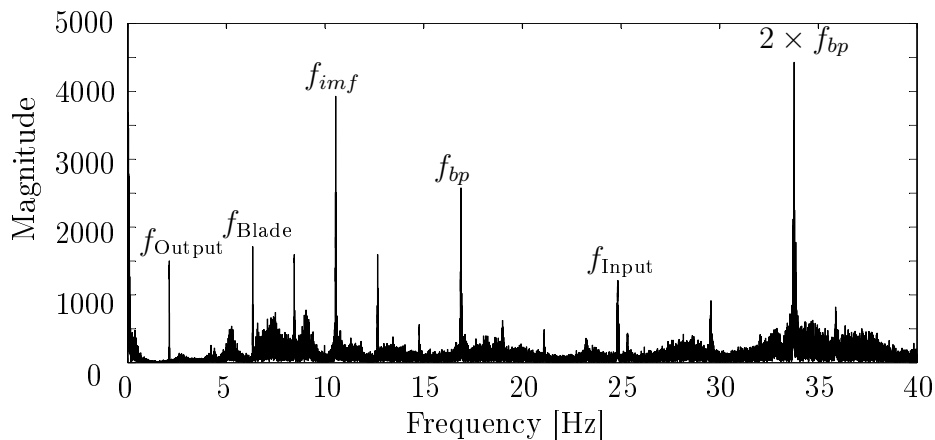


Figure 4.37: Frequency spectrum of gearbox vibration in the x -direction, from 0 Hz to 40 Hz.

Chapter 5

Conclusion

The loads that an operational ACC gearbox are subjected to, were successfully measured and analysed in this research paper. Tests were performed on a Hansen M4ACC gearbox at Eskom's Matimba power station. Measurements were taken during the start-up, run-down and normal operational periods of the gearbox, with the investigation aimed at shaft torsion, gearbox vibration and output shaft bending. Valuable insight was gained regarding gearbox behaviour during adverse weather conditions, as well as the interaction between input and output shaft torque. Previous research has failed to publish torque data obtained from the input shaft of an operational ACC gearbox, whereas this research succeeded at just that.

5.1 Areas of Investigation

Past research had succeeded in documenting on-site torsion and bending data from the output shaft of an ACC gearbox. However, the focus was primarily on the development of the measurement system and fan blade loading. This study aimed to include measurements from the input shaft of such a gearbox, and perform a more in-depth analysis of the measured torsional and bending data, with the focus on gearbox loading. Emphasis is also placed on the accuracy of the measured data and the analysis thereof.

This study showed that the challenges that are faced with when measuring torsion on the input shaft of an ACC gearbox during operation include: (1) limited space around the input shaft and the region where strain gauges could be positioned; (2) rotational speed of the shaft made it susceptible to imbalance from sensors, and complicated sensor installation on to the shaft; (3) data transmission from the rotating shaft, through the cast iron lantern housing, to the data acquisition apparatus; (4) accuracy of the measurements due to the shaft geometry, i.e. close proximity of the keyway and the strain gauges.

Gearbox load behaviour was investigated during the start-up, run-down, and normal operation period of the gearbox. Excessive torsional gearbox load-

ing during start-up was measured and analysed, while reverse loading of the gearbox was measured during the run-down period of the fan, as the fan momentum drove the motor for a short period of time. The electrical motor power was compared to the mechanical gearbox input power during the start-up and normal operational period of the gearbox. Measurements taken during the normal operational period allowed the analysis of gearbox torque transfer, gearbox vibration, torsional vibrations, output shaft bending, gearbox temperature, and the effect of varying wind conditions on output shaft loading.

5.2 Investigation Findings

A review of past literature showed that there is a lack of published measurements of full scale operational ACC behaviour. Previous work could be modified and used in this research project, i.e. the measurement system. Chapter 2 also investigated gearbox failures and identified the general causes thereof.

The accuracy of torsional strain measured on the input shaft is quantified in Chapter 3, where FEM is used to predict the stress distribution around the keyway and in the region of the strain gauges. The FE analysis is performed in Section 3.4. A statistical analysis is performed in Section 3.5 to create a calibration curve that relates measured strain to shaft torque with a given tolerance, whilst incorporating: (1) the combined effect of strain gauge positioning and non-homogeneous stress distribution on the shaft circumference; (2) the varying elastic modulus and Poisson's ratio of the input shaft material. Section 3.2 showed how an input shaft was tested in a laboratory environment. Digital image correlation was used in Section 3.3 to compare deformation of both sides of the keyway. A temperature correction factor was determined in Section 3.6 and can be used to adjust torque measurements on the input shaft. The laboratory torque measurements were found to be within the tolerance band of the calibration curve, as shown in Section 3.7.

The calibration curve from Section 3.7 is used to relate the measured input shaft strain to torque, while fundamental strength of material equations are used to determine the output shaft torque. The output shaft measurements correlate well with those performed by Muiyser (2012) on a similar gearbox. Results from Section 4.5.1 showed that start-up torque can be four times higher than the expected operational torque, but remained within the gearbox rated torque. Good correlation was found between the mechanically measured power on the input shaft and the electrical power being drawn by the motor. Speed and temperature measurements showed that it takes 3.163 s for the fan to start-up and roughly two hours for the gearbox to reach operational temperature.

Measurements taken during normal operation showed good correlation between motor output power and gearbox input power, as well as torsion measured on both gearbox shafts. In Section 4.5.2 the results show that shaft temperature influences the torque measurements as the elastic properties of the shaft

change when the shaft temperature increases, while the theory used to calculate torque assumes constant elastic properties. The frequency spectrum of input and output shaft torsion is also analysed, where it can be seen that torsional vibrations are transferred through the gearbox.

Firstly, during analysis of the gearbox run-down period in Section 4.5.3 it can be seen that the fan slows down exponentially rather than linearly as with the start-up speed. Secondly, a significant finding is the occurrence of reverse loading when the fan drives the motor. This refers to the non-loaded flanks of the gear teeth being loaded when the load (fan) becomes the driver. Lastly, A spectrogram is used to analyse the frequency spectrum of the output shaft torsion where it can be seen that the natural frequency of the fan blade decreases exponentially with shaft speed, rather than remaining constant.

Correlation between wind conditions and output shaft bending can be drawn based on the analysis performed on shaft bending in Section 4.6. Digital filters were utilized to isolate specific bending components in the measured signal. Analysis showed that wind direction and speed may cause the output shaft to bend away from the oncoming wind as the fan reacts to the distorted inlet air flow, while fan hub and blade angle misalignment also had a significant influence on output shaft bending. Gearbox vibration results are shown in Section 4.7, where gearbox-fan system vibrations were identified.

5.3 Recommendations for Future Measurements

Effects of material properties and stress concentrations near surface abnormalities should not be based on assumptions when absolute measurements are to be recorded. In order to measure strain and accurately relate it to either torsion or bending, it is required to know the material properties of the parts that are tested. A reliable statistical analysis of the material properties with a given distribution of the properties would suffice. If the geometry of the surface that was tested is of any concern, a calibration should be performed between the measured quantity and the strain gauges. In the case that a calibration is not possible, a numerical analysis should be performed to predict what the strain gauges would be measuring. It is highly recommended to measure the temperature of the component that is tested, to have a better idea of the change in material properties. Future research should attempt long term measurements, to capture more adverse weather conditions, i.e. thunderstorms, low temperatures and high wind speeds.

Appendices

Appendix A

Gear Design

This section focusses on the general design of a multi-stage, parallel-axis-helical-gear gearbox that resembles the gearboxes used in ACC's at South African power stations. Notably the design techniques used in this section are referenced from Shigley's Mechanical Engineering Design (Budynas and Nisbet, 2015) who obtained this information from ANSI/AGMA 2001-D04.

The following four equations are used in ANSI/AGMA 2001-D04 for gear design. The equations are in SI units and were converted to SI units by Budynas and Nisbet (2015). The gear bending stress is expressed as

$$\sigma = W^t K_o K_v K_s \cdot \frac{1}{b m_t} \cdot \frac{K_H K_B}{Y_J} \quad (\text{A.1})$$

Where

W_t is tangential transmitted load [N],

K_o is the overload factor,

K_v is the dynamic factor,

K_s is the size factor,

P_d is the transverse diametral pitch,

b is the face width of the narrower member [mm],

K_H is the load-distribution factor,

K_B is the rim thickness factor,

Y_J is the geometry factor for bending strength,

m_t is the transverse metric module.

The gear contact stress is shown as

$$\sigma_c = Z_E \cdot \sqrt{W^t K_o K_v K_s \cdot \frac{K_H}{d_{w1} b} \cdot \frac{Z_R}{Z_I}}, \quad (\text{A.2})$$

with W^t , K_o , K_v , K_s , K_H and b defined the same as for Equation A.1. Where as

Z_E is the elastic coefficient [$\sqrt{\text{Pa}}$],

Z_R is the surface condition factor,

d_{w1} is the pitch diameter of the pinion, [mm],

Z_I is the geometry factor for pitting resistance.

The above mentioned terms can be viewed as advice concerning items that should be considered by the designer if he/she follows the voluntary standard or not. The advice concerning items include issues such as transmitted load magnitude, overload, dynamic augmentation of transmitted load, size, pitch and face width, distribution of load across the teeth, rim support of tooth and the lewis form factor. The equation for allowable bending stress is given as

$$\sigma_{\text{all}} = \frac{S_t}{S_F} \cdot \frac{Y_N}{Y_\theta Y_Z} \quad (\text{A.3})$$

where

S_t is allowable bending stress [Pa]

Y_θ is the temperature factor,

Y_Z is the reliability factor,

S_F is the AGMA factor for safety.

The equation for allowable contact stress is expressed as

$$\sigma_{c,\text{all}} = \frac{S_c}{S_H} \cdot \frac{Z_N Z_W}{Y_\theta Y_Z} \quad (\text{A.4})$$

where

S_c is allowable contact stress [Pa],

Z_N is the stress cycle factor,

Z_W is the hardness ration factor for contact resistance,

Y_θ is the temperature factor,

Y_Z is the reliability factor,

S_H is the AGMA factor for safety.

The allowable AGMA safety factors are for unidirectional loading, 10 million stress cycles and 99% reliability. All terms mentioned in Equations A.1 to A.4 can be calculated with the use of Budynas and Nisbet (2015).

Designing or choosing a gear is based on the specification of the given application. When designing a helical gear there is a set of decisions (or design steps) that need to be made. Steps 1 to 5 can be classified as a priori steps and can be done before any design iteration is necessary. A summary of the steps would be as follows;

Step 1: Function (load, speed, reliability, overload factor or lifespan) - The function is based on the application of the gearbox.

Step 2: Unquantifiable risk (design factor) - Unquantifiable risk could be dependent on external factors i.e. environmental, socio-economic etc.

Step 3: Tooth system (pressure angle, helix angle, addendum, dedendum and root fillet radius) - Tooth system is chosen according to ANSI/AGMA 2001-D04.

Step 4: Gear ratio (bigger than 1, number of teeth on pinion and number of teeth on gear) - Gear ratio is based on the relationship between the rotating speed of the input and output shafts.

Step 5: Quality number - This is also dependent on the application of the gearbox i.e. commercial quality gears have quality number between 3 and 7 whilst high precision gears range between 8 and 12.

Steps 6 to 10 form part of the iterative design process of the gear. The iterative process should be performed as follows;

Step 6: Diametral pitch - A trial value for the diametral pitch is chosen initially.

Step 7: Pinion bending stress - First consider the pinion and Equation A.1 and find a face width that satisfies the geometry factor for bending strength, also choose the pinion material and core hardness accordingly. Then check the factor of safety in bending with Equation A.3.

Step 8: Gear bending stress - Again make use of Equation A.1 and find a companion core hardness for the gear, also check the factor of safety in bending for the gear with Equation A.3.

Step 9: Pinion contact stress - Find the necessary surface contact strength S_c from ANSI/AGMA 2001-D04 tables. Then choose a case hardness level and check the factor of safety in contact stress using Equations A.2 and A.4.

Step 10: Gear contact stress - Find the companion gears case hardness from ANSI/AGMA 2001-D04 tables. Check that the factor of safety is satisfactory by again using Equations A.2 and A.4.

A satisfactory gear design will be achieved by following the above mentioned design steps. Choosing different diametral pitches will yield parallel designs from which the designer may choose. Unfortunately, in the academic environment it is tedious to find a figure of merit when it comes to gear design, as material and processing costs vary. The wide range of factors should be considered, where some may justifiably be set equal to 1 for design simplicity.

Appendix B

Relation Between Strain and Electric Resistance

The relationship between electric resistance and strain of a metal wire can be expressed mathematically, and the derivation of the relationship equation is shown in this section.

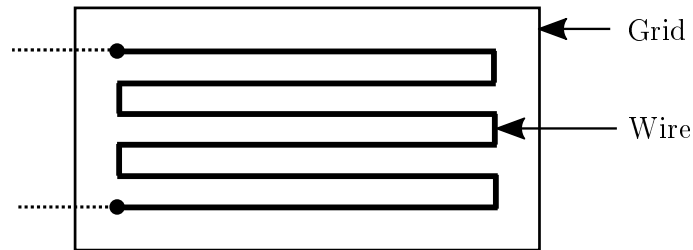


Figure B.1: Resistive wire placed on a plastic grid.

Consider the wire strain gauge shown in Figure B.1. The wire has a length l , cross section A and an electric resistivity ρ . The resistance R of the wire can then be calculated as

$$R = \frac{\rho \cdot l}{A}. \quad (\text{B.1})$$

The change in wire resistance is as a function of the wire geometry and resistivity and can be expressed as

$$dR = \frac{\rho}{A} \cdot dl - \frac{\rho \cdot l}{A^2} \cdot dA + \frac{l}{A} \cdot d\rho, \quad (\text{B.2})$$

meaning that,

$$\frac{dR}{R} = \frac{dl}{l} - \frac{dA}{A} + \frac{d\rho}{\rho}. \quad (\text{B.3})$$

When the strain gauge is bonded to a surface it is assumed that the strain gauge and the surface deform the same. This means that the strain experienced by the wire in the longitudinal direction is the same as the strain on the surface for the same direction, thus

$$\epsilon_l = \frac{dl}{l}. \quad (\text{B.4})$$

The cross sectional area of the wire also changes because of Poisson's ratio. Assuming a cylindrical wire with a radius r , it is possible to express the normal strain in the radial direction of the wire as

$$\epsilon_r = \frac{dr}{r} = -\nu \cdot \epsilon_l = -\nu \frac{dl}{l}. \quad (\text{B.5})$$

Assuming small strain, it is possible to express the change rate of the cross sectional area as

$$\frac{dA}{A} = (1 + \epsilon_r)^2 - 1 = 2\epsilon_r + \epsilon_r^2 \approx 2\epsilon_r = -2\nu \frac{dl}{l}. \quad (\text{B.6})$$

Substituting Equation B.4 to B.6 into Equation B.3, it is possible to express the change in resistance as

$$\frac{dR}{R} = (1 + 2\nu) \frac{dl}{l} + \frac{d\rho}{\rho} = (1 + 2\nu)\epsilon_l + \frac{d\rho}{\rho} \quad (\text{B.7})$$

Now the sensitivity (k) of resistance versus strain, also known as the gauge factor, is calibrated as

$$k = \frac{dR/R}{\epsilon_l} = 1 + 2\nu + \frac{d\rho/\rho}{\epsilon_l}. \quad (\text{B.8})$$

Strain can then be expressed as a function of change in resistance ($\Delta R/R$) and the gauge factor,

$$\epsilon = \frac{\Delta R}{k \cdot R}. \quad (\text{B.9})$$

Appendix C

Instrument Calibration

The calibration of the PCB-Accel-333B32 and RSCC-Load-Cell is discussed and shown in this section.

C.1 Accelerometer

The accelerometers used in this investigation are calibrated beforehand using a SV111 Vibration Calibrator and a HEAD acoustics SQuadriga II, shown in Figure C.1 and C.2.



Figure C.1: SV111 Vibration Calibrator.



Figure C.2: HEAD acoustics SQuadriga II.

An accelerometer is placed on the vibration plate, while the plate acceleration and frequency of oscillation is specified in the settings panel. The SQuadriga II is used to measure the output voltage of the accelerometer as the vibration plate oscillates. The sensitivity of the accelerometer is established by relating the output voltage of the accelerometer to the motion of the vibration plate. Figure C.3 shows the vibration plate, and Figure C.4 shows the settings panel. Calibration is performed in a quiet environment where no external factors could influence the motion measured by the accelerometers.

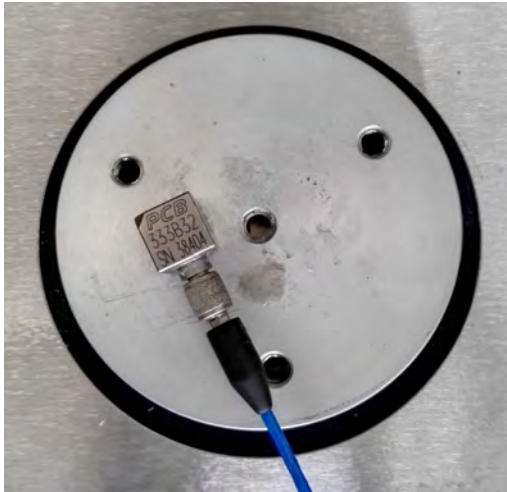


Figure C.3: PCB-Accel-333B32 positioned on the vibration plate.



Figure C.4: Settings panel of the SV111 Vibration Calibrator.

C.2 Load Cell

The load cell is used to determine the load applied to the moment arm by means of turn buckle in Section 3.2. Calibration is performed on the load cell beforehand to relate the output voltage of the load cell to some mass. Calibration is performed by placing weights on top of the load cell while measuring the output voltage of the cell. A computer and a HBM Spider8 are used to communicate with the load cell and record its output. Figure C.5 shows the RSCC-Load-Cell, while Figure C.6 illustrates the calibration setup.



Figure C.5: HBM RSCC-Load-Cell.

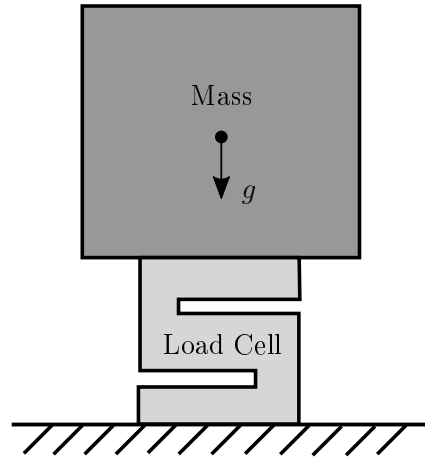


Figure C.6: Calibration setup.

The result of the calibration is shown in Figure C.7, where a linear relationship between mass and load cell output voltage is defined. This curve is used to determine the load that is applied to the moment arm in Section 3.2.

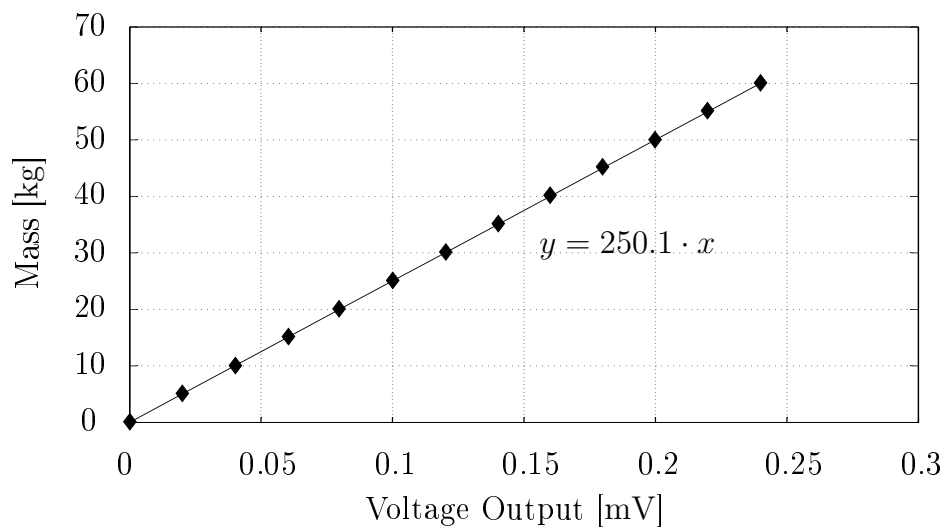


Figure C.7: Load cell calibration curve.

Appendix D

Finite Element Analysis

Finite element analysis is performed in Section 3.4, and this appendix aims to elaborate on the relationship between shaft torque and stress, as well as the effect that material properties have on shaft stress.

D.1 Stress and Varying Material Properties

Load control is used to model the input shaft in Section 3.4, meaning that the stress throughout the shaft is calculated without considering the elastic properties of the shaft. When using displacement control, the shaft is displaced a certain amount before shaft stresses are calculated as a function of the elastic properties. This statement is proved for load control by varying the material properties of the shaft while monitoring the shear stress at a specific node. The results are shown in Figures D.1 and D.2. Elastic modulus and Poisson's ratio of the shaft material is varied.

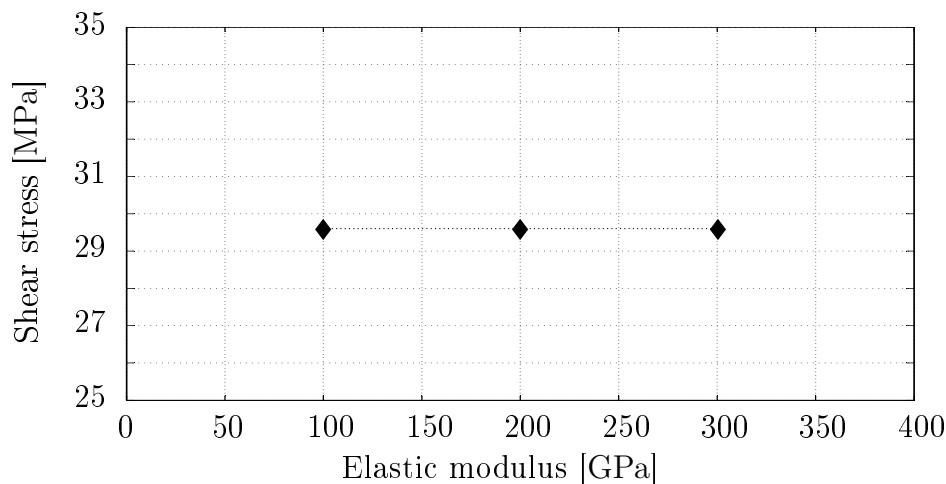


Figure D.1: Load control with varying elastic modulus.

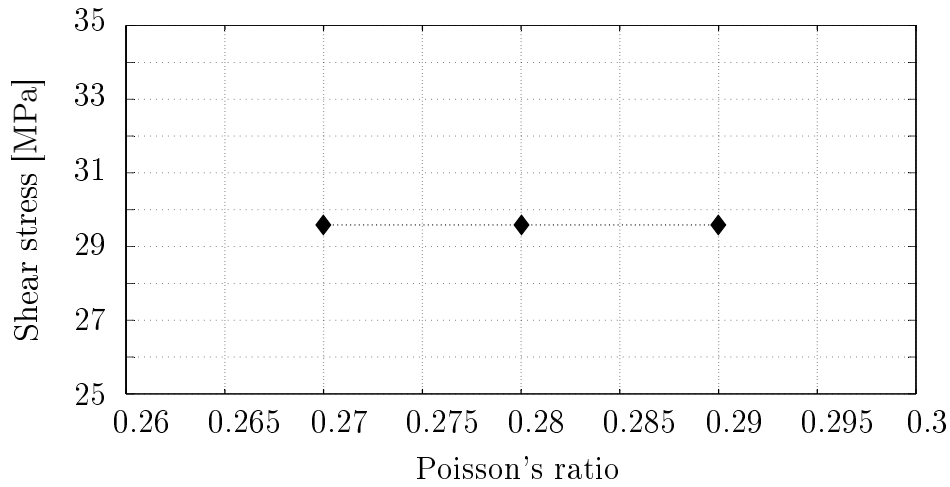


Figure D.2: Load control with varying Poisson's ratio.

D.2 Linearity of Stress and Torque

The assumption that a linear relationship exists between torsion applied to the input shaft, and shear stress on the surface of the shaft is proven in this section. The applied shaft torque is varied in increments of $500 \text{ N} \cdot \text{m}$ while the shear stress is probed at a single node. Figure D.3 shows the result proving that shear strain on the surface of the shaft increases linearly with shaft torque.

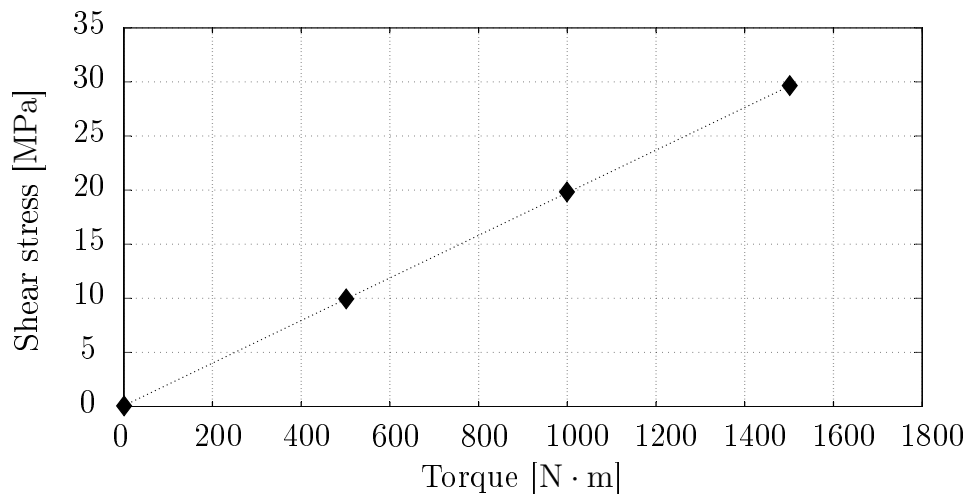


Figure D.3: Relationship between shaft torque and shear stress.

Appendix E

Oscilloscope Measurements

According to Hiscocks (2013), power factor can be calculated from AC voltage and current measurements. Power factor is calculated as the cosine of the phase angle between voltage and current. Figure E.1 shows the normal fan operation AC measurements obtained from the switchboard at the ACC of Matimba power station. Peak line to neutral voltage (V_{LN}) and current (I_{LN}) is measured.

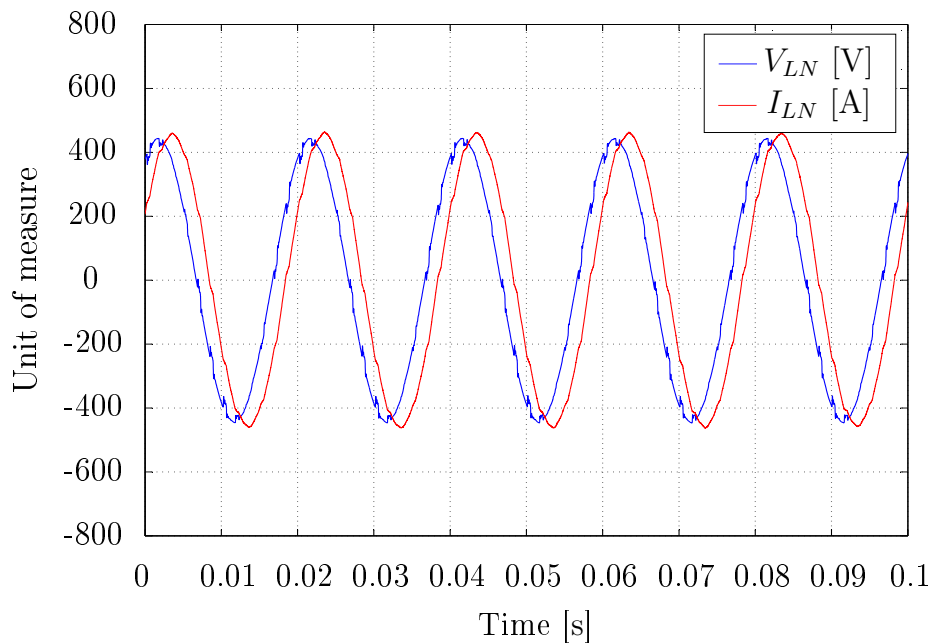


Figure E.1: Line to neutral voltage and current.

The time shift (Δt) between the voltage and current signal can be measured from the data and is found to be 0.001 99 s. Figure E.2 illustrates how the time shift is measured.

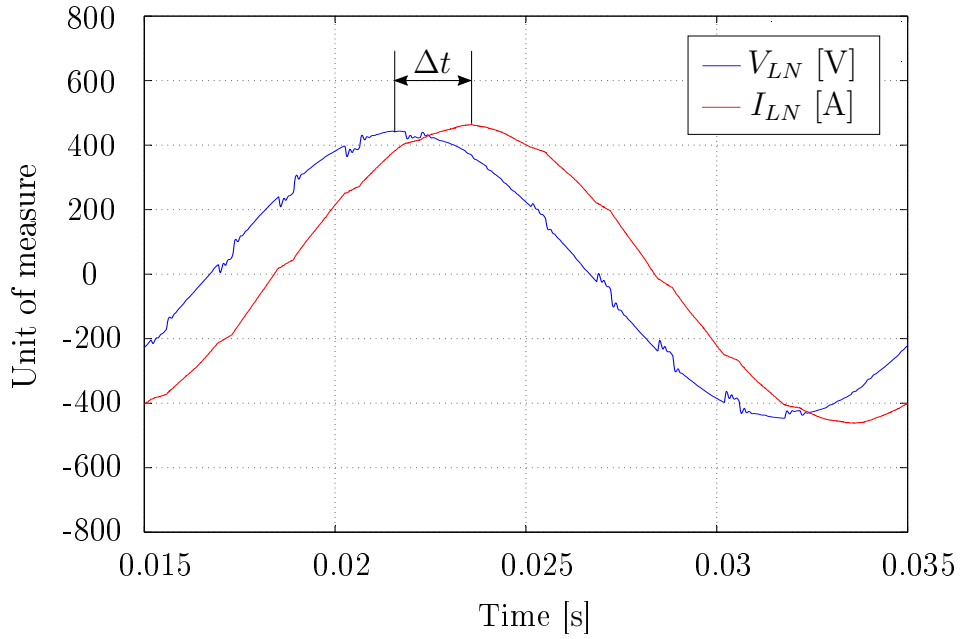


Figure E.2: Time lag between line voltage and current.

The signal frequency is 50 Hz, relating to a wave period T_w of 0.02 s. The phase shift can then be derived as,

$$\phi = \frac{\Delta t}{T_w} \cdot 360^\circ. \quad (\text{E.1})$$

The power factor is then calculated as,

$$PF = \cos(\phi). \quad (\text{E.2})$$

Using Equation E.2, the PF for the induction motor used in the ACC of Matimba power station is calculated as 0.811.

Appendix F

Weather Station Data

This section gives the temperature and wind data obtained from a weather station near Matimba power station. The measurements are taken 40 m above the ground.

Date [DD/MM]	Time [HH:MM]	Temperature [°C]	Wind Speed [m/s]	Wind Direction
18/04	08:00	21.14	36.26	10.88
	09:00	22.70	34.90	10.70
	10:00	24.61	40.25	8.37
	11:00	25.96	36.36	8.68
	12:00	27.84	33.42	10.00
	13:00	29.60	27.27	11.21
	14:00	31.17	29.39	11.78
	15:00	32.03	32.31	27.99
	16:00	32.41	24.81	25.50
	17:00	32.55	21.72	22.57
19/04	08:00	20.44	31.08	8.26
	09:00	21.47	44.93	7.07
	10:00	23.02	41.94	8.84
	11:00	24.96	43.17	6.42
	12:00	26.47	38.13	7.28
	13:00	27.85	36.72	9.72
	14:00	29.26	32.49	7.70
	15:00	30.13	31.09	15.10
	16:00	30.66	37.87	14.31
	17:00	30.65	35.95	10.52
20/04	08:00	20.71	34.21	11.53
	09:00	22.74	29.56	9.53
	10:00	24.92	27.44	7.78
	11:00	26.79	21.28	10.81

APPENDIX F. WEATHER STATION DATA

97

	12:00	28.54	23.93	10.82
	13:00	29.97	29.78	11.86
	14:00	30.39	29.94	11.53
	15:00	31.62	30.14	11.23
	16:00	31.46	17.76	9.65
	17:00	31.73	28.39	26.86
<hr/>				
21/04	08:00	21.81	20.13	13.22
	09:00	23.67	19.25	11.48
	10:00	25.91	16.03	24.57
	11:00	28.05	30.01	30.47
	12:00	28.12	53.47	27.79
	13:00	27.41	84.35	25.85
	14:00	26.34	117.56	26.08
	15:00	24.96	116.32	25.43
	16:00	24.00	92.10	25.60
	17:00	23.91	66.30	24.55
<hr/>				
22/04	08:00	18.35	7.63	18.70
	09:00	20.74	18.12	12.83
	10:00	23.08	25.67	7.64
	11:00	25.11	23.72	11.73
	12:00	27.01	26.21	9.69
	13:00	28.82	23.04	12.44
	14:00	30.03	23.19	26.50
	15:00	31.18	28.53	27.39
	16:00	31.58	20.33	30.68
	17:00	31.53	18.26	31.00
<hr/>				
23/04	08:00	20.73	26.83	13.70
	09:00	23.08	25.19	12.65
	10:00	25.95	22.57	9.79
	11:00	28.23	29.16	8.46
	12:00	30.62	34.42	14.50
	13:00	31.96	30.79	31.97
	14:00	32.77	25.49	29.68
	15:00	32.86	25.81	31.49
	16:00	33.10	25.36	33.60
	17:00	32.91	15.90	31.79
<hr/>				
24/04	08:00	20.87	48.90	11.87
	09:00	21.11	63.45	10.65
	10:00	22.20	64.45	10.97
	11:00	23.79	65.76	9.29
	12:00	24.74	63.72	8.41
	13:00	25.75	64.81	6.49
	14:00	27.28	63.67	4.94

	15:00	27.51	64.41	4.27
	16:00	27.95	65.80	3.95
	17:00	27.57	69.20	2.98
25/04	08:00	18.17	21.08	13.69
	09:00	19.76	33.36	8.44
	10:00	20.82	44.17	5.64
	11:00	22.30	37.54	4.83
	12:00	24.25	30.55	7.51
	13:00	26.25	24.64	26.95
	14:00	28.14	17.95	18.59
	15:00	29.42	15.67	26.27
	16:00	30.28	17.38	26.22
	17:00	30.61	14.90	10.50
26/04	08:00	20.42	17.85	13.79
	09:00	22.47	24.51	10.10
	10:00	24.82	18.66	9.66
	11:00	27.18	13.40	13.60
	12:00	28.28	20.43	16.91
	13:00	30.12	29.11	17.97
	14:00	31.52	31.29	19.87
	15:00	30.52	65.15	11.01

Table F.1: Weather station measurements.

Appendix G

Project Photographs

Photographs of the investigation are shown in this section to give insight on some practical aspect involved with this project.

G.1 Gearbox Input Shaft

Figures G.1 and G.2 illustrate the input shaft of the M4ACC gearbox with the problematic keyway.

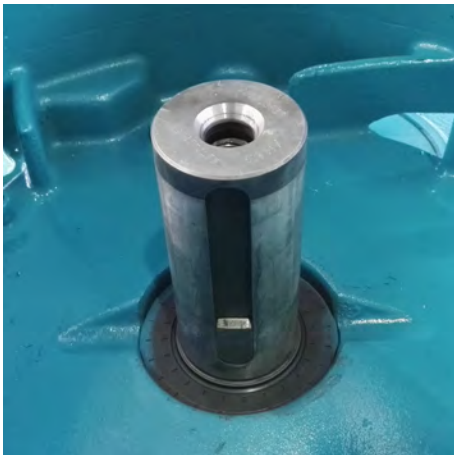


Figure G.1: Input shaft.



Figure G.2: Input shaft front view.

Figures G.3 and G.4 show the sleeve that covers the area available for strain gauge application, and how the problem was overcome by machining a hole on both sides of the sleeve.



Figure G.3: Sleeve with machined opening.

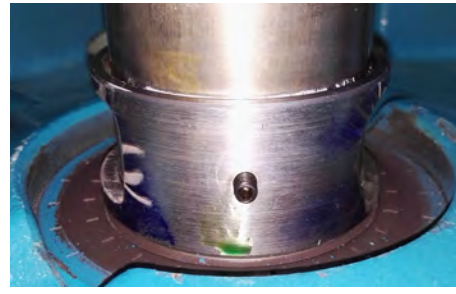


Figure G.4: Sleeve with grub screw to keep sleeve in place.

G.2 Strain Gauge Rosettes

The positioning of strain gauge rosettes onto both gearbox shafts are shown in Figures G.5 to G.7.

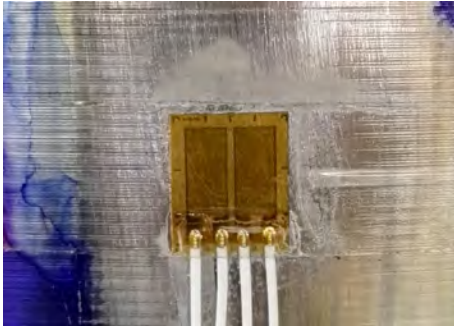


Figure G.5: Bending strain gauge rosette on the output shaft.

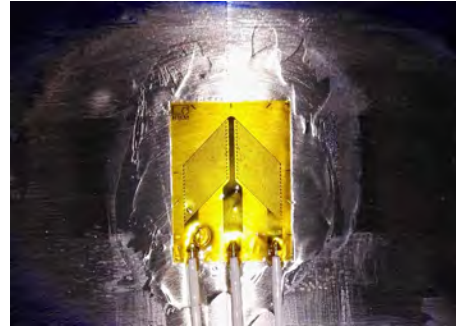


Figure G.6: Torsional strain gauge rosette on the output shaft.

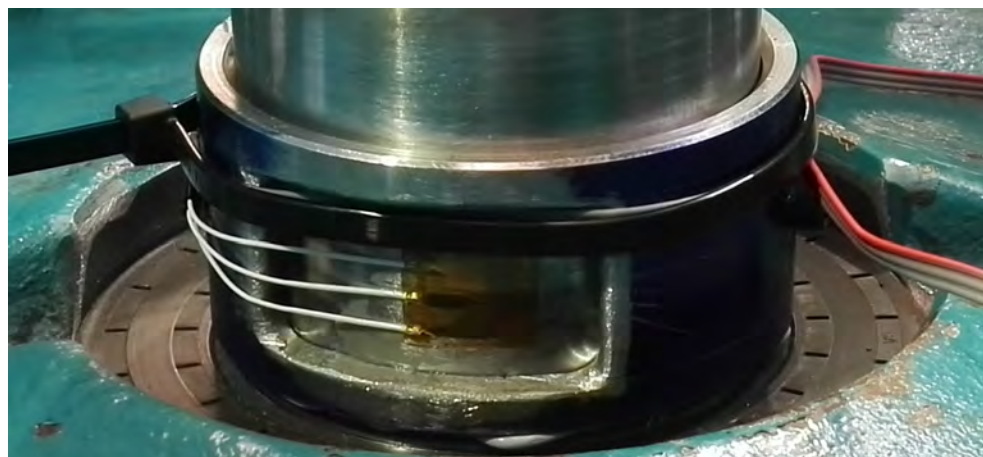


Figure G.7: Torsional strain gauge rosette on the input shaft.

G.3 Proximity Sensor Connection

Proximity sensors are used to measure the speeds of both gearbox shafts during the various operational states. Figures G.8 and G.9 show how the proximity sensor and the magnet are mounted on the input shaft.



Figure G.8: Proximity sensor rod for input shaft speed measurement.



Figure G.9: Magnet and proximity sensor used for input shaft.

Figures G.10 and G.11 show how the proximity sensor and the magnet are positioned for speed measurements on the output shaft.



Figure G.10: Proximity sensor positioned for output shaft speed measurement.



Figure G.11: Proximity sensor and magnet used to measure the output shaft speed.

G.4 Shaft Protection

The safety of the strain gauges and the Link's during transit, installation and operation were a concern for the project. This section shows which safety precautions were applied to both gearbox shafts. Figures G.12 and G.13 show how the SG-Link-LXRS and the connecting wires were fastened to withstand transit and operation.



Figure G.12: SG-Link-LXRS installed onto high speed coupling with free hanging connecting wires.

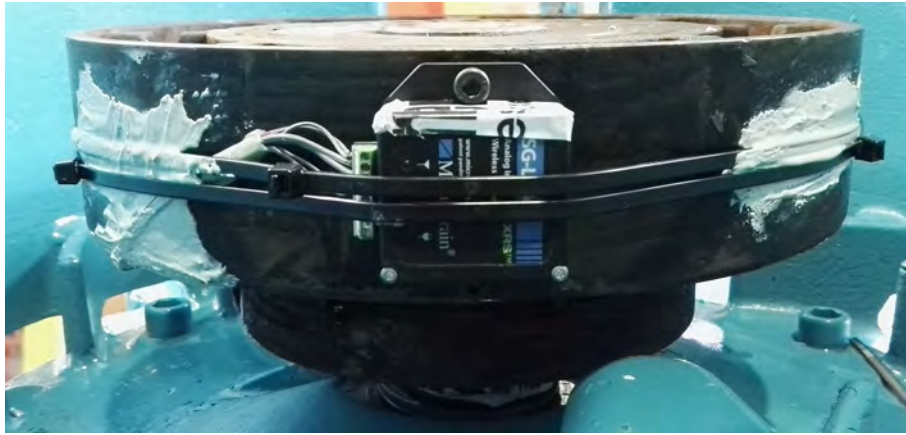


Figure G.13: SG-Link-LXRS installed onto high speed coupling with connecting wires fixed to the coupling with quick set cement.

Figures G.14 and G.15 show how the output shaft is prepared for transit and installation. Operation is not of concern for the output shaft as the rotational speed is low.

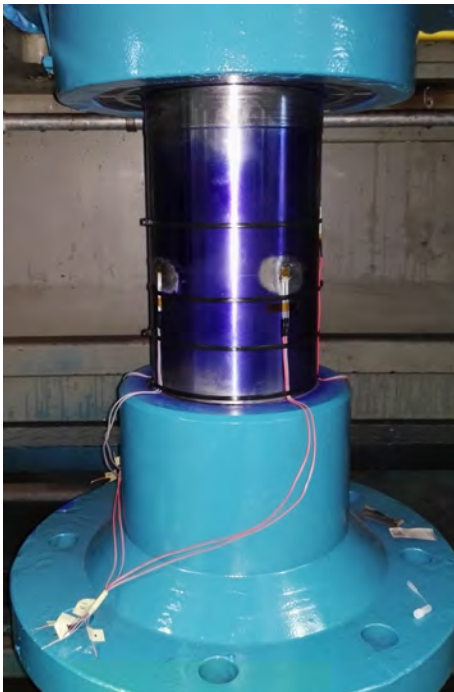


Figure G.14: Strain gauges positioned on the output shaft. Figure G.15: Output shaft protection before transport.

G.5 Gearbox Installation

The installation of the gearbox requires that the gearbox be lifted by crane from the ground to the ACC platform, shown in Figure G.16.



Figure G.16: Connecting the lift to the gearbox on the ground.



Figure G.17: Gearbox being lowered into position in the ACC.

Thereafter the gearbox is positioned onto the fan bridge, and the fan hub is connected, as shown in Figures G.17 and G.18. Figure G.19 shows the complete ACC unit after installation.



Figure G.18: Connecting the gearbox output shaft to the fan hub.



Figure G.19: Installation complete.

Appendix H

Measurement Data

H.1 Start-up Power Transfer

Section 4.5.1 shows the start-up torque transfer for the days from the 19th to the 21st of April. This section gives the power transfer for the same days. Figures H.1 to H.3 show the power transfer from the input to the output shaft during the fan start-up period.

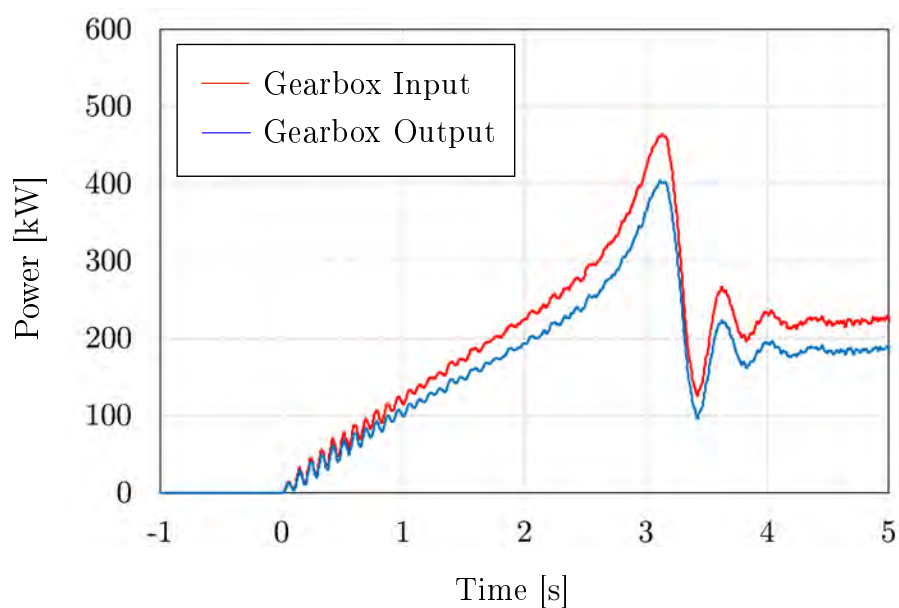


Figure H.1: Start-up power transmission of the gearbox on 19 April 2016.

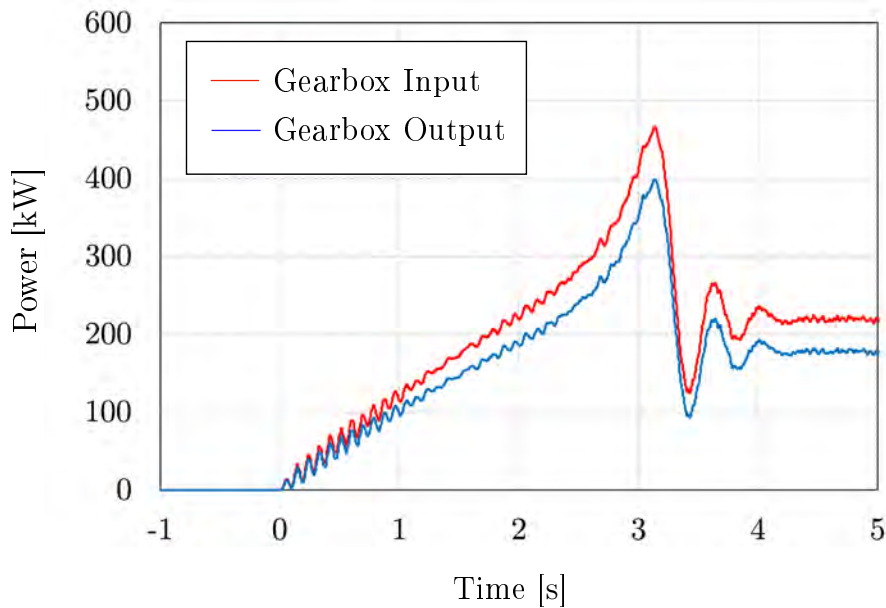


Figure H.2: Start-up power transmission of the gearbox on 20 April 2016.

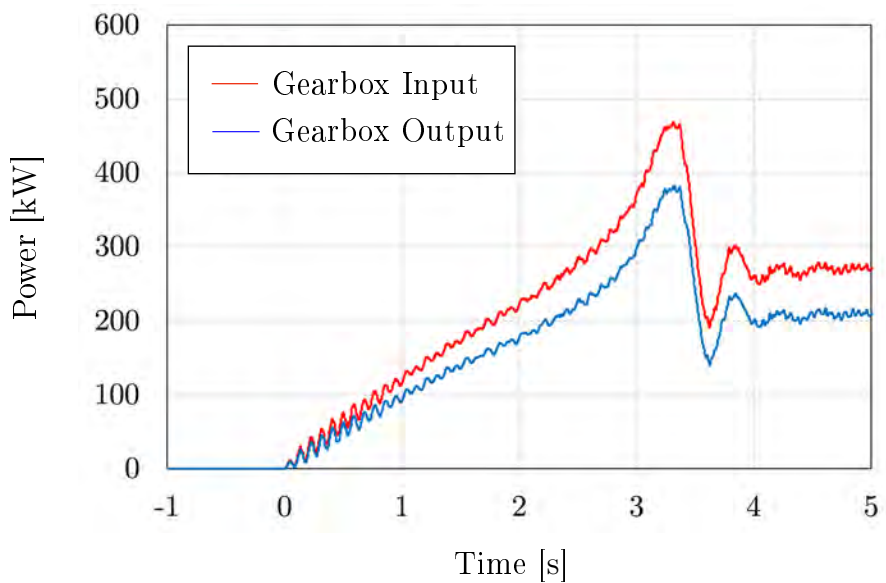


Figure H.3: Start-up power transmission of the gearbox on 21 April 2016.

H.2 Raw Output Shaft Bending

This section shows the raw bending measurements before they are plotted on to polar plots. Figure H.4 shows the bending measured by each bending full bridge configuration for a duration of two minutes. The absolute bending moment on the output shaft is calculated by the vector sum of the individual

bending moments, and is shown in Figure H.5, along with the direction of the thereof in Figure H.6. Figures H.7 and H.8 show the absolute bending moment of the output shaft and the angle thereof for a two second period, where it is more visible that the magnitude and angle of the bending moment varies over time. The polar plots used in this study better illustrate the magnitude and direction of the output shaft bending.

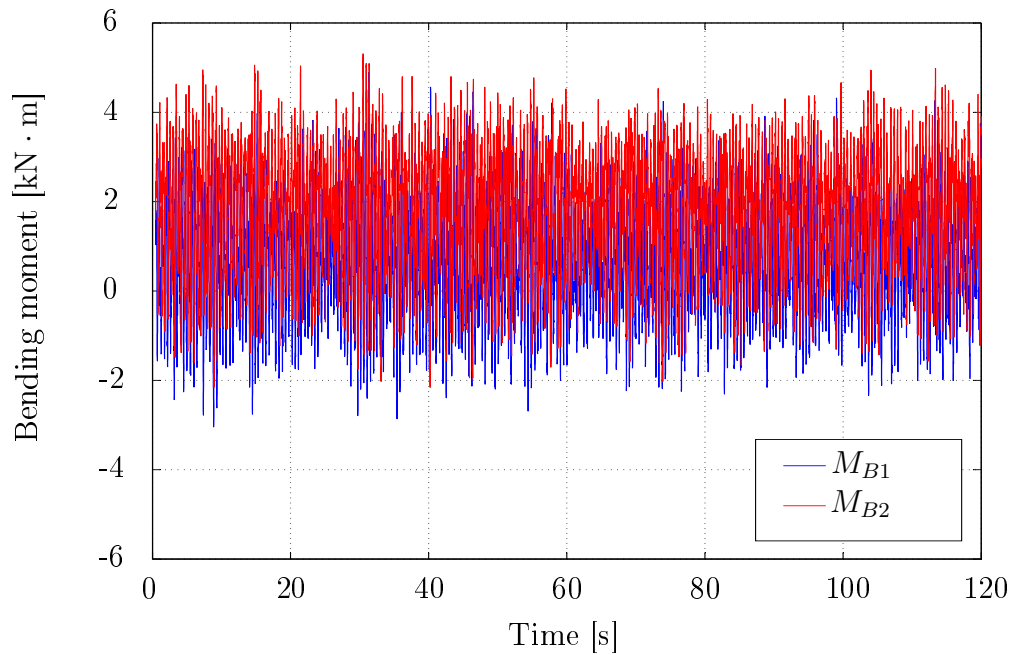


Figure H.4: Bending moment measured on the output shaft by both bending full bridge configurations.

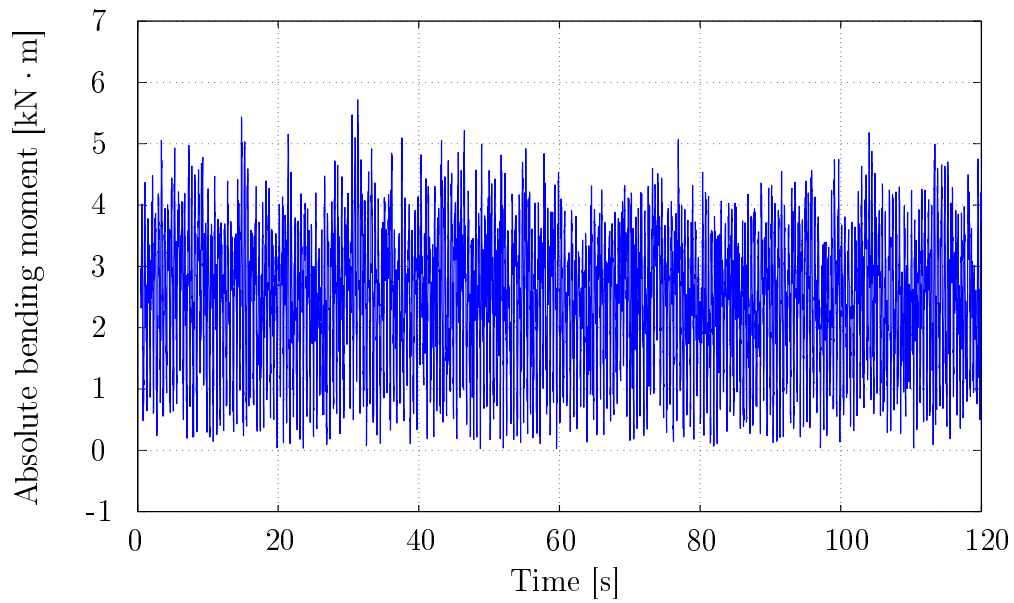


Figure H.5: Absolute bending moment experienced by the output shaft.

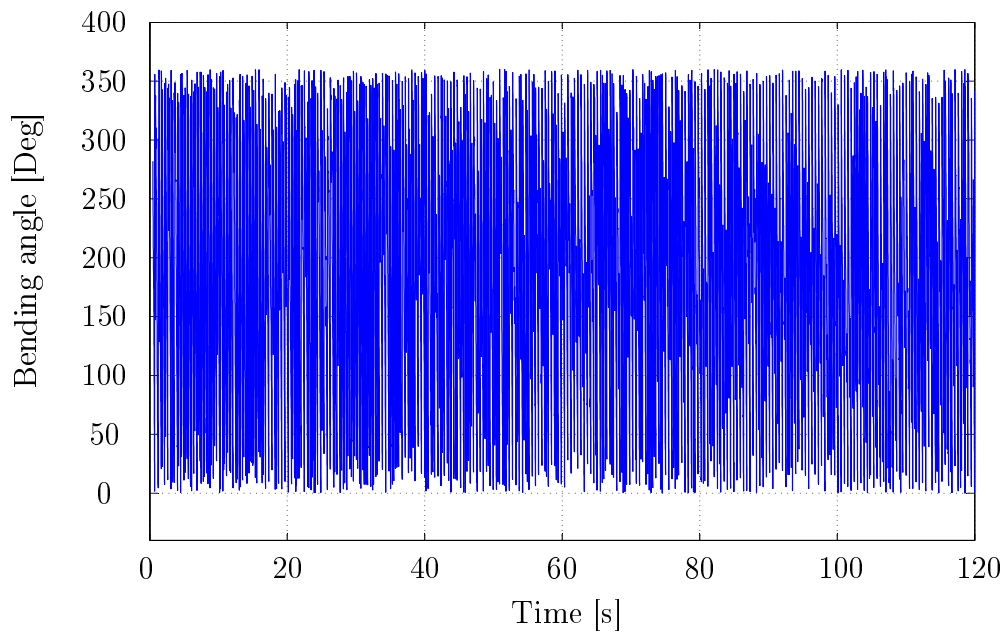


Figure H.6: Angle of absolute bending moment, with regard to the global coordinate system.

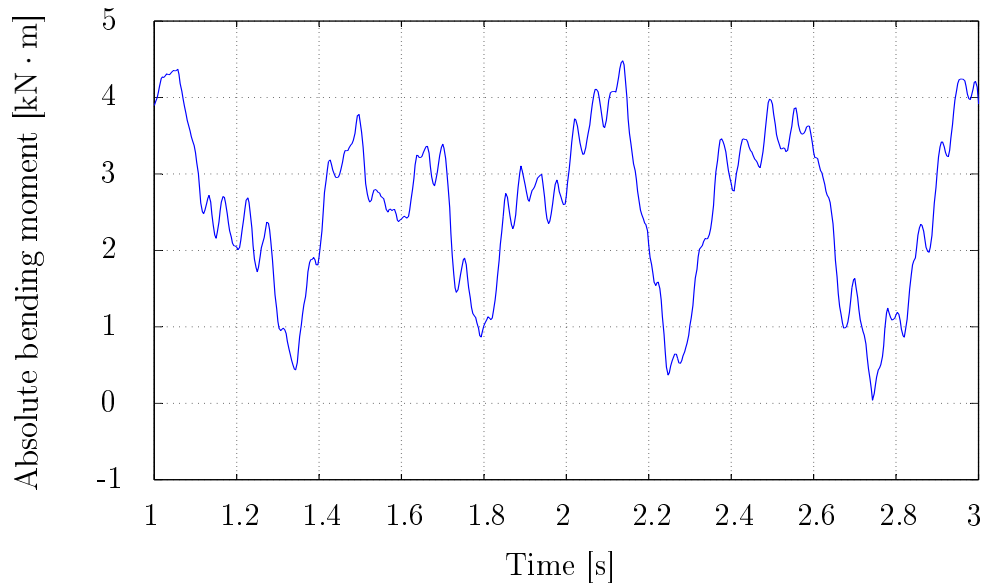


Figure H.7: Absolute bending moment experienced by the output shaft shown for a two second period.

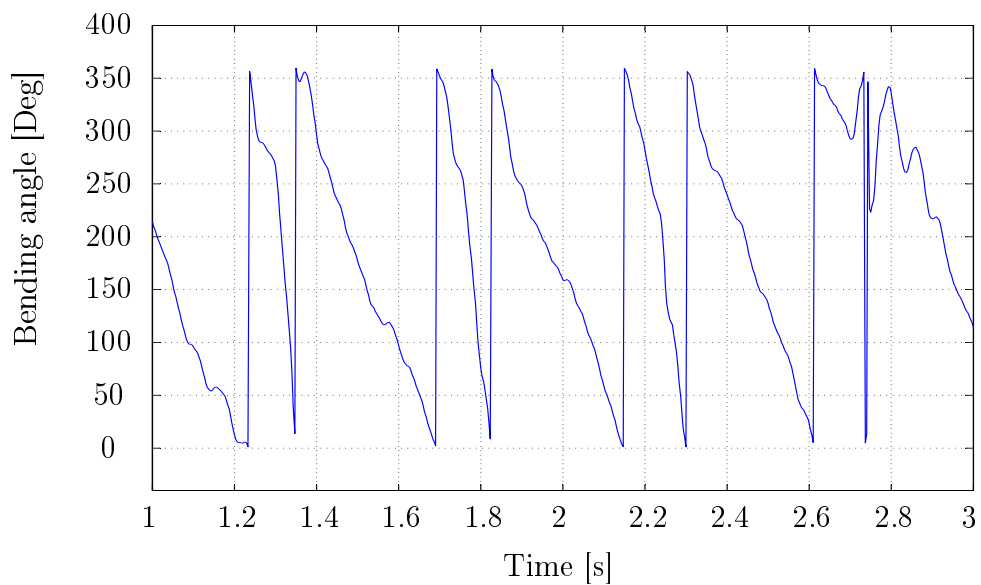


Figure H.8: Angle of absolute bending moment, with regard to the global coordinate system, shown for a two second period.

H.3 Filtered Output Shaft Bending

This section presents the bending components present in the bending data measured on the output shaft for a constant wind speed, but a varying wind direction. The analysis of the bending data is performed in Section 4.6.

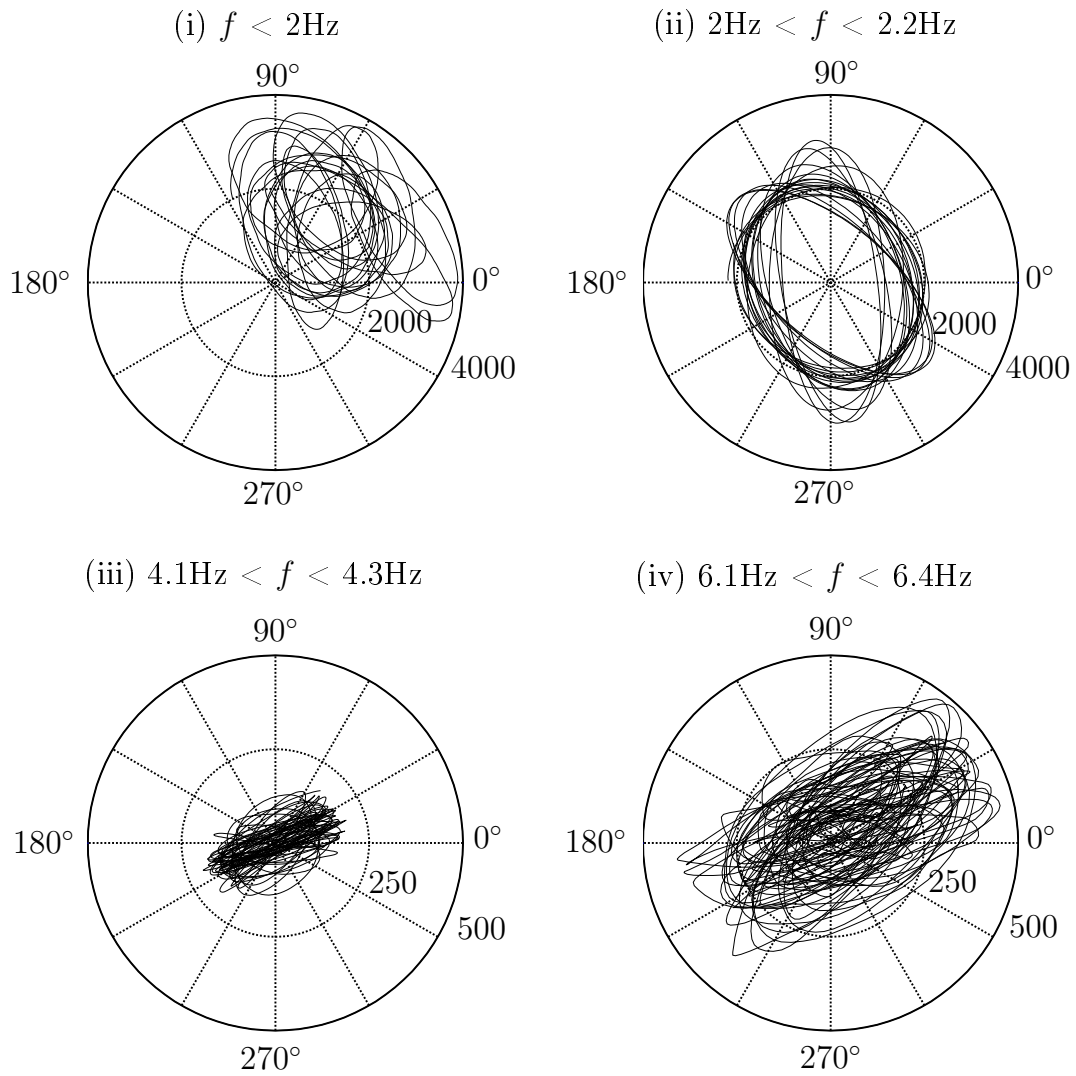


Figure H.9: Polar plot of bending components present in the bending data for a wind speed and direction of 25.4 m/s and 116°ESE.

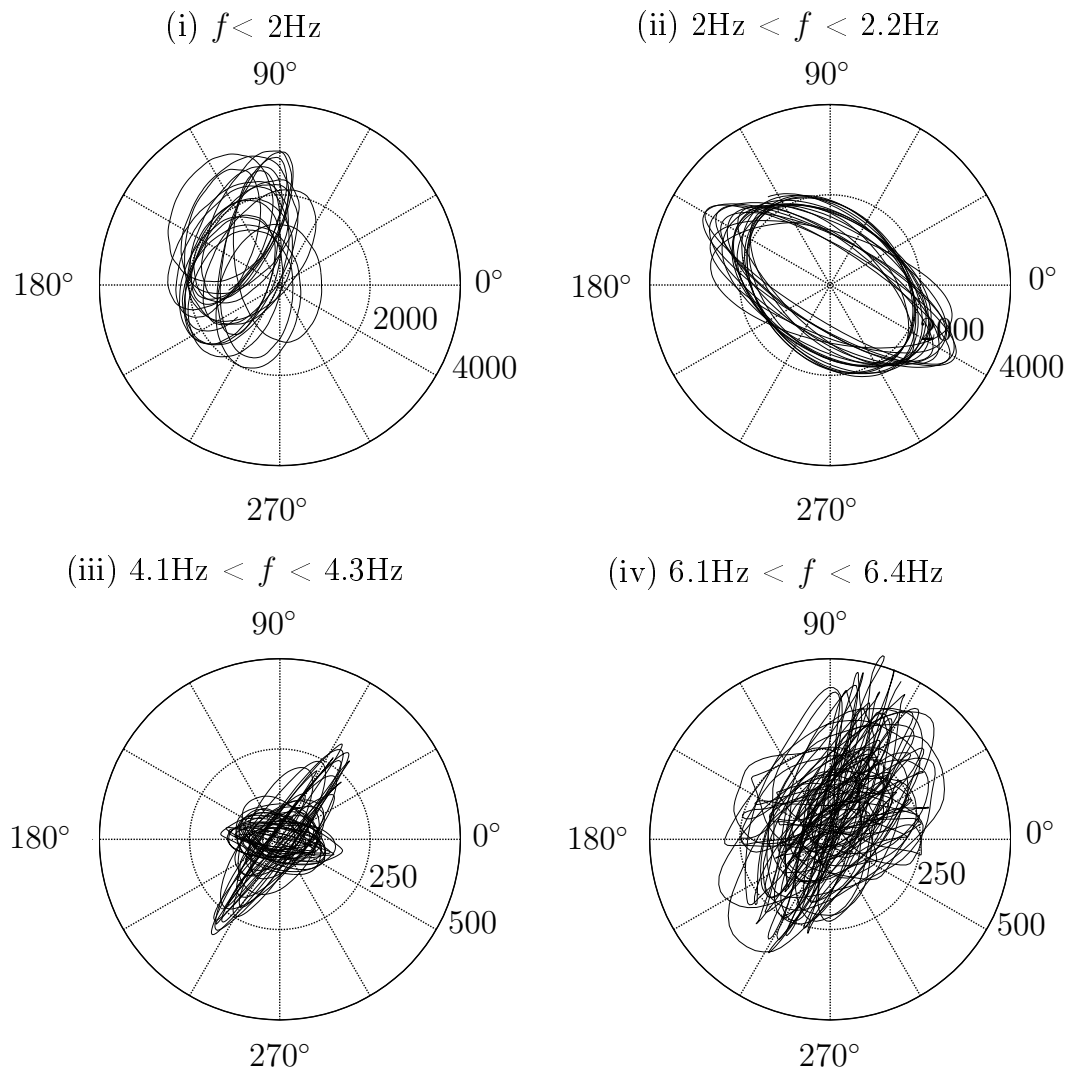


Figure H.10: Polar plot of bending components present in the bending data for a wind speed and direction of 24.6 m/s and 66°ENE.

Bibliography

- Ai, X. (2001). Effect of Debris Contamination on the Fatigue Life of Roller Bearings. *Journal of Engineering Tribology*.
- Andersson, M. (2014). *Churning Losses and Efficiency in Gearboxes*. Ph.D. thesis, KTH Royal Institute of Technology.
- ANSI/AGMA 2001-D04 (2004). Fundamental Rating Factors and Calculation Methods for Involute Spur and Helical Gear Teeth. Tech. Rep., AGMA.
- Application Note 290-1 (1981). Practical Strain Gage Measurements. Tech. Rep., Hewlett Packard.
- Artemis SUITE (2015). Artemis suite basic analysis module (code 5001). Data sheet, HEAD-acoustics, Herzogenrath, Germany.
- ASTM E1876-01 (2005). Standard test method for dynamic young's modulus, shear modulus, and poisson's ration by impuls excitation of vibration. Tech. Rep., ASTM International, West Conshohocken, PA.
- Ayyub, B.M. (1998). *Uncertainty Modeling and Analysis in Civil Engineering*. CRC Press LLC.
- Bartelmus, W. and Zimroz, R. (2008). Vibration condition monitoring of planetary gearbox under varying external load. *Mechanical Systems and Signal Processing 2009*.
- Benham, P.P., Crawford, R.J. and Armstrong, C.G. (1996). *Mechanics of Engineering Materials*. Pearson.
- Bentler, P.M. (2006). EQS 6 Structural Equations Program Manual. Manual, University of California.
- Beèr, J.M. (2007). High Efficiency Electric Power Generation: The Environmental Role. *Progress in Energy and Combustion Science*.
- Boglietti, A., Cavagnino, A., Pastorelli, M. and Vagati, A. (2005). Experimental Comparison of Induction and Synchronous Reluctance Motors Performance. *IEEE Industry Application Society*.
- Brandlein, J., Eschmann, P., Hasbargen, L. and Weigand, K. (1995). *Ball and Roller Bearings*. Wiley.

- Bredell, J.R., Kroger, D.G. and Thiart, G.D. (2006). Numerical investigation of fan performance in a forced draft air-cooled steam condenser. *Applied Thermal Engineering*.
- BS EN 10084:2008 (2008). Case hardening steels - technical delivery conditions. Standard, European Committee for Standardization, rue de Stassart, Brussels.
- Budynas, R.G. and Nisbet, J.K. (2015). *Shigley's Mechanical Engineering Design*. McGraw Hill.
- Catman Professional 5.0 (). Catman Professional 5.0. Tech. Rep., Hottinger Baldwin Messtechnik GmbH Software, Darmstadt, Germany.
- Cengel, Y.A. and Ghajar, A.J. (2015). *Heat and Mass Transfer*. McGraw Hill.
- Chen, J., Young, B. and Uy, B. (2006). Behaviour of high strength structural steel at elevated temperatures. *Journal of Structural Engineering*.
- Cimbala, J.M. (2013). Stress, Strain, and Strain Gages. Tech. Rep., Penn State University.
- CMG Performance Report (2006). Performance report. Data sheet, CMG Technology.
- Cook, R., Malkus, D.S., Plesha, M.E. and Witt, R.J. (2002). *Concepts and Applications of Finite Element Analysis*. John Wiley & Sons, Inc.
- de Groot, P.J., Wijnen, A.M. and Janssen, B.F. (1995). Real-time frequency determination of acoustic emission for different fracture mechanisms in carbon/epoxy composites. *Composites Science and Technology*.
- eFunda (2016). Strain Gage: Theoretical Background.
Available at: http://www.efunda.com/designstandards/sensors/strain_gages/strain_gage_theory.cfm
- El-Hawary, M.E. (2002). *Principles of Electric Machines with Power Electronic Applications*. Wiley-Interscience.
- Fay, H.P.R. (1997). Air Cooled Condenser.
- FLIR E8 (2013). Flir Ex series. User manual, FLIR, Wilsonville, OR.
- Folta, Z. and Hrudickova, M. (2013). EExperience with Torque Measurement on Rotating Shaft. *Transactions on Electrical Engineering*.
- Garg, A. and Tomar, A.S. (2015). Starting time calculation for induction motor. *Int. Journal of Engineering research and Applications, Vol. 5, Issue 5, pp. 56-60*.
- Göksenli, A. and Eryürek, I.B. (2009). Failure Analysis of an Elevator Drive Shaft. *Engineering Failure Analysis*.
- Goldschagg, H. (2013). ACC Fan Gearbox. In: *ACCUG Nevada Conference*.

- Haldar, A. and Mahadevan, S. (2000). *Probability, Reliability and Statistical Method in Engineering Design*. John Wiley & Sons, Inc.
- Hameed, Z., Hong, Y.S., Cho, Y.M., Ahn, S.H. and Song, C.K. (2009). Condition monitoring and fault detection of wind turbines and related algorithms: A review. *Renewable And Sustainable Energy Reviews*.
- Hansen Industrial Transmissions(2004) (2004). Power Solutions for Cooling Towers and Air Cooled Condensers. Data sheet, Hansen Industrial Transmissions.
- Harcarik, T., Bocko, J. and Maslakova, K. (2012). Frequency Analysis of Acoustic Signal Using the Fast Fourier Transformation in MATLAB. *Procedia Engineering* 48.
- Harris, T.A. and Kotzalas, M.N. (2007). *Essential Concepts of Bearing Technology*. Taylor & Francis.
- HBM Spider8 (2003). Spider8. Operating Manual, Hottinger Baldwin Messtechnik GmbH.
- HEAD Recorder (2016). Head recorder. Data sheet, HEAD-acoustics, Herzogenrath, Germany.
- Hibbeler, R.C. (2013). *Mechanics of Materials*. Pearson.
- Hiscocks, P.D. (2013). Measuring AC Current and Power Factor.
- Hoffmann, K. (1986). Applying The Wheatstone Bridge Circuit. Application Guide, Hottinger Baldwin Messtechnik GmbH, Darmstadt.
- Hoffmann, K. (1989). *An Introduction to Measurements using Strain Gages*. Hottinger Baldwin Messtechnik GmbH, Darmstadt.
- Hoffmann, K. (1996). Practical Hints for the Installation of Strain Gages. Installation Guide, Hottinger Baldwin Messtechnik GmbH.
- Kim, H.-Y. (2013). Statistical notes for clinical researchers: assessing normal distribution (2) using skewness and kurtosis.
Available at: <http://synapse.koreamed.org/DOIx.php?id=10.5395/rde.2013.38.1.52>
- Kröger, D.G. (2004). *Air-Cooled Heat Exchangers and Cooling Towers*. PennWell.
- Ledbetter, H.M. and Austin, M.W. (1984). Elastic constant versus temperature behaviour of three hardened maraging steels. *Materials Science and Engineering*.
- Lin, P.I.-H. (2014). Three-Phase Induction Motors.
Available at: http://www.etc.s.ipfw.edu/~lin/ECET211/spring2014/1-Lectures/ECET211_Lect_3pIM.htm
- Liu, P., Duan, H. and Zhao, W. (2009). Numerical investigation of hot air recirculation of air-cooled condensers at a large power plant. *Applied Thermal Engineering*.

- Lord, J.D. and Morrell, R. (2007 February). Elastic Modulus Measurement. National Physical Laboratory, Measurement Good Practice Guide No. 98.
- Luchetta, S. (2014). Preventive Maintenance: An Examination of the Root Causes of Gearbox Failure.
Available at: http://www.philagear.com/news_press_prmay04.shtm
- Mahadevan, S. (1997). *Reliability-Based Mechanical Design*. Marcel Dekker, Inc.
- Manojlovic, J. and Jankovic, P. (2013). Bridge measuring circuits in the strain gauge sensor configuration. *Mechanical Engineering, Vol. 11, pp. 75-84*.
- Matlab R2013b (2016). MATLAB Primer. Primer, MathWorks.
- McCormick, N. and Lord, J. (2010). Digital image correlation. *Materials Today*.
- McFadden, P.D. and Smith, J.D. (1984). Model for the Vibration Produced by a Single Point Defect in a Rolling Element Bearing. *Journal of Sound and Vibration*.
- McGinty, B. (2012). Continuum Mechanics Website - Strain Gauges.
Available at: <http://www.continuummechanics.org/index.html>
- Meirovitch, L. (2001). *Fundamentals of Vibration*. McGraw Hill.
- Meyer, C.J. (2005). Numerical investigation of the effect of inlet flow distortions on forced draught air-cooled heat exchanger performance.
- MSC.Software (2016). Interference Fits.
Available at: <http://www.mssoftware.com/exercise-modules/interference-fits>
- Muiyser, J. (2012). *Simultaneous measurement of air flow conditions and the resultant blade and gearbox loading at large-scale cooling system fans*. Master's thesis, Stellenbosch University.
- Muiyser, J., Els, D.N.J., Van Der Spuy, S.J. and Zapke, A. (2014). Measurement of air flow and blade loading at a large-scale cooling system fan. *R & D Journal of the South African Institute of Mechanical Engineering*.
- Nguyen, V.M., Doherty, P.S. and Riffat, S.B. (2001). Development of a Prototype Low-Temperature Rankine Cycle Electricity generation System. *Applied Thermal Engineering*.
- NIST/SEMATECH (2013). Engineering Statistics Handbook.
Available at: <http://www.itl.nist.gov/div898/handbook/index.htm>
- Node Commander 2.10.0 (2014). Node Commander Wireless Sensor Software Suite. User manual, LORD MicroStrain SENSING SYSTEMS, Williston, VT.
- PCB-Accel-333B32 (2002). Model 333B32. User Manual, PCB Piezotronics, 3425 Walden Avenue, Depew, NY.

- PCB-Microphone-378B02 (2014). Model 378B02. User Manual, PCB Piezotronics, 3425 Walden Avenue, Depew, NY.
- Phala, S., Aspen, D., Du Preez, F., Goldschagg, H. and Northcott, K. (2007). Corrosion in Air Cooled Condensers - Understanding and Mitigating the Mechanisms.
- Pillay, K., Nour, P., Yang, K.H., Harun, D. and Haw, L.K. (2009). Assessment and Comparison of Conventional Motor Starters and Modern Power Electronic Drives for Induction Motor Starting Characteristics. In: *IEEE Symposium on Industrial Electronics and Applications*.
- Polak, S. (1999). Gearbox & Gear System Problems. In: *IMEchE*. Available at: <http://www.tribology.co.uk/articles-papers/gearbox-gear-problems/>
- Pretorius, J. (2012). Eskom Perspective on Specifications for Large ACC's. In: *ACC User Group Meeting*.
- QuantumX MX1601B (). QuantumX i3031-11.0. User manual, Hottinger Baldwin Messtechnik GmbH, Darmstadt, Germany.
- Ramsden, E. (2006). *Hall-Effect SSensor, Theory and Application*. Elsevier.
- Redwood, M. (1961). Transient Performance of a Piezoelectric Transducer. *The Journal of the Acoustic Society of America*.
- Roelands, C.J.A. (1966). *Correlation Aspects of the Viscosity-Temperature-Pressure Relation of Lubricating Oils*. Ph.D. thesis, Delft University of Technology.
- RSCC-Load-Cell (2014). RSCC Load Cell. Data Sheet, Hottinger Baldwin Messtechnik GmbH, Im Tiefen See 45, 64293 Darmstadt, Germany.
- Serridge, M. and Licht, T.R. (1987). *Piezoelectric Accelerometers and Vibration Preamplifiers*. Brüel & Kjaer.
- SG-Link-LXRS (2015). SG-link-LXRS. User manual, LORD MicroStrain, Williston, VT.
- Smith, J.D. (1999). *Gear Noise and Vibration*. Marcel Dekker.
- SQuadriga II (2016). SQuadriga II (code 3320). Data sheet, HEAD-acoustics, Herzogenrath, Germany.
- StrainMaster (2016). StrainMaster. Brochure, LaVision, Goettingen, Germany. Available at: <http://www.lavision.de/en/download.php?id=323pdf>
- Surgeon, M. and Wevers, M. (1999). Modal analysis of acoustic emission signals from cfrp laminates. *NDT&E International* 32.
- Sutton, M.A., Cheng, M., Peters, W.H., Chao, Y.J. and McNeill, Y.J. (1986). Application of an optimized digital correlation method to planar deformation analysis. *Image and vision computing, Vol. 4, No. 3*.

- Sutton, M.A., Wolter, W.J., Peters, W.H., Ranson, W.F. and McNeill, S.R. (1983). Determination of displacement using an improved digital correlation method. *Image and vision computing, Vol. 1, No. 3*.
- Sutton, M.A., Yan, J.H., Tinwari, V., Schreider, H.W. and Orteu, J.J. (2008). The effect of out-of-plane motion on 2d and 3d digital image correlation measurement. *Optics and Lasers in Engineering, Vol. 46, pp. 746-757*.
- SV111 Vibration Calibrator (2011). SV 111 Vibration Calibrator. Instruction Manual, Svantek, Warszawa, Poland.
- TN-514 (2013). Shunt Calibration of Strain Gage Instrumentation. Technical Note, Vishay Precision Group, Micro-Measurements.
- V-Link-LXRS (2015). V-link-LXRS. User manual, LORD MicroStrain, Williston, VT.
- Verbeek, D. (2016). Material Properties of Input/Output Shafts at Hansen Belgium. [Email Correspondence].
- Wang, W.J. and McFadden, P.D. (1993). Early Detection of Gear Failure by Vibration Analysis: Calculation of the Time-Frequency Domain. *Mechanical Systems and Signal Processing*.
- WEG W22 Three-Phase Electric Motor (2015). W22 three-phase electric motors. Technical catalogue european market, WEG, Duluth, GA.
- Winterton, J.G. (1991). Component identification of gear-generated spectra. *Orbit*.
- WSDA-Base-104 (2015). WSDA-base-104. User manual, LORD MicroStrain, Williston, VT.
- Xiao, S., Jiang, X. and Li, X. (2015). Contact Stress Analysis of Tapered Interference Fit for the Cantilevered Axle. In: *Material, Mechanical and Manufacturing Engineering*.
- Yntema, R.T. (1955). National Advisory Committee for Aeronautics - TN 3459. Technical Note, Langley Aeronautical Laboratory.
- Zenginobuz, G. (2001). Soft starting of large induction motors at constant current with minimized starting torque pulsations. *IEEE Transactions on Industry Applications*.